

NATIONAL TECHNICAL UNIVERSITY OF ATHENS SCHOOL OF ELECTRICAL AND COMPUTER ENGINEERING SCHOOL OF MECHANICAL ENGINEERING

INTERDISCIPLINARY POSTGRADUATE PROGRAMME "Translational Engineering in Health and Medicine"

Multi-Scale Simulation and Printability Assessment of Implantable Titanium Voronoi Scaffolds for Femur Bone Defect Management

Postgraduate Diploma Thesis

Georgios Emmanouil Poulakis

Supervisor: Vasilios Spitas (Professor School of Mechanical Engineering NTUA)

Approved by the examination committee on: 4 /July 2025



NATIONAL TECHNICAL UNIVERSITY OF ATHENS SCHOOL OF ELECTRICAL AND COMPUTER ENGINEERING SCHOOL OF MECHANICAL ENGINEERING

INTERDISCIPLINARY POSTGRADUATE PROGRAMME "Translational Engineering in Health and Medicine"

Multi-Scale Simulation and Printability Assessment of Implantable Titanium Voronoi Scaffolds for Femur Bone Defect Management

Postgraduate Diploma Thesis

Georgios Emmanouil Poulakis

Supervisor: Vasilios Spitas (Professor School of Mechanical Engineering NTUA)

The postgraduate diploma thesis has been approved by the examination committee on: 4 / July 2025

1st member

Spitas Vasilios, Professor, School of Mechanical Engineering/NTUA 2nd member

Manopoulos Christos,
Associate Professor, School
of Mechanical
Engineering/NTUA

3rd member

Markopoulos Aggelos, Professor, School of Mechanical Engineering/NTUA

Athens, July 2025

Georgios Emmanouil Poulakis
Graduate of the Interdisciplinary Postgraduate Programme,
"Translational Engineering in Health and Medicine",
Master of Science,
School of Electrical and Computer Engineering,
National Technical University of Athens

Copyright © - Georgios Poulakis 2025 All rights reserved.

You may not copy, reproduce, distribute, publish, display, modify, create derivative works, transmit, or in any way exploit this thesis or part of it for commercial purposes. You may reproduce, store or distribute this thesis for non-profit educational or research purposes, provided that the source is cited, and the present copyright notice is retained. Inquiries for commercial use should be addressed to the original author.

The ideas and conclusions presented in this paper are the author's and do not necessarily reflect the official views of the National Technical University of Athens.

Abstract

This diploma thesis investigates the treatment of critical femoral bone defects using patient-specific, 3D-printed implantable lattice scaffolds, focusing on both mechanical performance and manufacturability. A highly accurate femur model was extracted from medical CT scan data to achieve anatomical precision at the problem location. A porous Voronoi lattice scaffold was created as it better balanced mechanical stability with biological integration. The geometry was carefully designed to correspond with the defect's morphology and to coincide with physiological load-bearing routes, assuring mechanical compatibility and the potential for osteointegration.

For the creation of the implant lattice, we utilized the nTopology software platform, which enabled the parametric design and optimization of a Voronoi lattice structure, chosen for its ability to mimic the natural porous structure of bone, promoting osseointegration and graded mechanical response. The final lattice geometry was incorporated into the overall femur model for the purposes of the simulations.

To assess the viability of manufacturing the scaffold using Selective Laser Melting (SLM), a series of simulations were executed using ANSYS Additive, a specialized process simulation tool. These simulations included a full-scale model of the entire scaffold, a refined 10 mm sliced section to capture higher resolution thermal effects during the printing process and several simulations of a cubed shaped lattice. For the cube shaped lattice, key outcome variables, displacement, von Mises stress, high strain severity, and recoater blade interference, were analyzed under a range of printing parameters, including laser power, beam width, scan speed, and layer thickness.

Results showed that layer height and laser power significantly influenced print quality and mechanical reliability, with 50 μ m layer height and laser power of 195 W or more yielding optimal results without increasing print time. In contrast, variations in laser width and scan speed ranging from 80–120 μ m and 600–1400 mm/s respectively, had minimal effect, offering flexibility in speed optimization. These trends suggest that precise control of printing settings is essential to achieving both geometric accuracy and mechanical robustness. The results highlight how simulation may help direct the design and manufacturing of intricate biomedical implants and provide a useful methodology for creating load-bearing scaffolds that are anatomically appropriate for orthopedic restoration.

Περίληψη

Η παρούσα διπλωματική εργασία ασχολείται με τη μελέτη και προσομοίωση εξατομικευμένων εμφυτεύσιμων πλεγμάτων για την αποκατάσταση εκτεταμένων οστικών ελλειμμάτων του μηριαίου οστού, μέσω της χρήσης τεχνολογιών 3D εκτύπωσης μετάλλων. Αρχικά, πραγματοποιήθηκε ανακατασκευή του μηριαίου οστού από δεδομένα αξονικής τομογραφίας (CT scan), προκειμένου να δημιουργηθεί ένα ακριβές τρισδιάστατο μοντέλο του κοκκάλου και εν συνεχεία του εμφυτεύσιμου ικριώματος.

Για τη δημιουργία του πλέγματος του εμφυτεύματος χρησιμοποιήθηκε η λογισμική πλατφόρμα nTopology, η οποία επέτρεψε τον παραμετρικό σχεδιασμό και τη βελτιστοποίηση μιας δομής τύπου Voronoi lattice, επιλεγμένης λόγω της ικανότητάς της να μιμείται τη φυσική πορώδη δομή του οστού, ευνοώντας την οστεοενσωμάτωση και τη διαβαθμισμένη μηχανική απόκριση. Η τελική γεωμετρία του πλέγματος ενσωματώθηκε στο συνολικό μοντέλο του μηρού για τις ανάγκες των προσομοιώσεων.

Οι προσομοιώσεις πραγματοποιήθηκαν μέσω του λογισμικού ANSYS Additive, το οποίο εξειδικεύεται στην προσομοίωση της διαδικασίας Selective Laser Melting (SLM). Αρχικά, πραγματοποιήθηκε προσομοίωση του πλήρους πλέγματος, ακολουθούμενη από ανάλυση ενός τεμαχίου ύψους 10 mm για καλύτερη ακρίβεια, λόγω των υπολογιστικών περιορισμών. Εξετάστηκαν βασικές μεταβλητές κατασκευής όπως η ισχύς του λέιζερ, το πλάτος της ακτίνας, το ύψος στρώσης και η ταχύτητα σάρωσης, μέσω της προσομοίωσης ενός μικρού, κυβικού σχήματος πλέγματος.

Τα αποτελέσματα αξιολογήθηκαν βάσει τεσσάρων κρίσιμων δεικτών: μετατόπιση, μέγιστες τάσεις von Mises κατά την διάρκεια της εκτύπωσης, περιοχές υψηλής παραμόρφωσης (strain severity) και πιθανά σημεία σύγκρουσης με τη λεπίδα εξομάλυνσης (blade crash). Οι προσομοιώσεις έδειξαν ότι το ύψος στρώσης και η ισχύς του λέιζερ επηρέασαν σημαντικά την ποιότητα εκτύπωσης και τη μηχανική αξιοπιστία. Ύψος στρώσης 50 μm και ισχύς λέιζερ 195 W ή υψηλότερη απέδωσαν τα βέλτιστα αποτελέσματα χωρίς αύξηση του χρόνου εκτύπωσης. Αντίθετα, οι μεταβολές στο πλάτος της δέσμης λέιζερ και στην ταχύτητα σάρωσης (80–120 μm, 600–1400 mm/s) είχαν ελάχιστη επίδραση, προσφέροντας ευελιξία στη βελτιστοποίηση της ταχύτητας εκτύπωσης.

Συνολικά, η εργασία παρουσιάζει μια ολοκληρωμένη προσέγγιση σχεδιασμού και προσομοίωσης προσαρμοσμένων οστικών εμφυτευμάτων lattice, η οποία ενσωματώνει βιομιμητικό σχεδιασμό και βελτιστοποίηση παραμέτρων εκτύπωσης. Η μεθοδολογία αυτή μπορεί να αποτελέσει χρήσιμο εργαλείο για την περαιτέρω ανάπτυξη προηγμένων, προσωποποιημένων λύσεων στην επανορθωτική ορθοπαιδική.

Acknowledgements:

I would like to sincerely thank my professor and supervisor Vasilios Spitas. His mentorship and assistance during this effort have been indispensable. He afforded me the opportunity to engage in a thesis topic that integrates mechanical design and biomechanics, and his guidance at each phase of the project has been vital to its success.

I would also like to express my gratitude to my coordinator Panos Ntakos for his involvement and support were essential to the project's accomplishment. His assistance and cooperation rendered this endeavor feasible and transformed it into a pleasurable educational experience.

Table of Contents

Abstract	5
Περίληψη	7
Acknowledgements:	9
List of Figures	13
1. Introduction	15
2. Femur Bone Defect Literature Review	15
2.1 Femur Bone Anatomy	15
2.2 Bone Healing Process - Association with Strain	17
2.3 Conventional Treatment Methods of Distal Femur Fractures	18
2.4 3D Printed Bone Implants - Materials and Design	20
3. 3D Printing Overview	22
3.1 Additive manufacturing Process	22
3.2 Non-Metallic Materials 3D Printing	22
3.3 Metal 3D printing	22
3.4 3D Printing Microstructure Lattices in Bone Imitating Implants	23
3.5 Selective Laser Melting (SLM) for Implantable Bone Scaffolds	23
4. Structured Scaffold CAD Design	25
4.1 From CT scan to CAD Model	25
4.1.1 Processing and Refinement	25
4.1.2 Rationale for Excluding Spongy Bone	32
4.2 Unit Cell to Porous Scaffold	33
4.3 Voronoi Lattice – nTopology	35
4.3.1 Why We Chose the Voronoi Lattice	35
4.3.2 From CAD Model to Voronoi Lattice Mesh using Ntop	35
5. Printing Process Simulation	41
5.1 Ansys Additive	41
5.1.1 Introduction to Ansys Additive	41
5.1.2 Theoretical Overview and Strain Simulation Types	41
5.2 Printing Process Simulation and Result Options	42
5.2.1 Simulation Geometry and Voxelization	42
5.2.2 Material Selection and Stress mode	43
5.2.3 Machine Parameters	44
5.2.4 Simulation Outputs Selection	45
5.3 Simulation and Results	47

	5.3.1 Full Scaffold Lattice Simulation	47
	5.3.2 High-Resolution Simulation of a 10mm Slice	57
	Observations on the 10 mm High-Resolution Slice Simulation	61
	5.3.3 Cube Lattice Simulation	62
į	5.4 Final Comments on Printing Parameters and Scaffold Design Modifications for Better Manufacturability	85
6. I	-uture Work	86
7. (Conclusion	87
Ref	ferences	88

List of Figures

- Figure 2.1 Femur Bone Regions
- Figure 2.2 Femur Proximal End
- Figure 2.3 Femur Distal End
- Figure 2.4 Bone Healing Process
- Figure 2.5 Femur Bone Retrograde Nailing Technique
- Figure 2.6 Femur Bone Antegrade Nailing Technique
- Figure 3.1 SLM 3D Printing Schematic
- Figure 4.1 3D Slicer Working Environment
- Figure 4.2 3D Slicer Femur Bone Before and After Trimming
- Figure 4.3 Corrected Mesh in Blender
- Figure 4.4 Bone Marrow and Spongy Bone Cavity Mesh in Blender
- Figure 4.5 Final Bone Mesh Model in Blender with Section View
- Figure 4.6 Mesh to CAD Model Conversion in NTop
- Figure 4.7 Importing Femur Bone CAD Model in Solidworks
- Figure 4.8 Final Implant Geometry Derived from CAD Model
- Figure 4.9 Femur Bone Proximal End Microstructure
- Figure 4.10 Deterministic Unit Cell Types Commonly Used in Bone Implants: (a) Cubic, (b) Diamond, (c) Gyroid, (d) Schwartz
- Figure 4.11 Cubic Voronoi Stochastic Lattice example
- Figure 4.12 CAD Model to Implicit Body
- Figure 4.13 Scaffold Volume Mesh for Voronoi Lattice Creation
- Figure 4.14 Voronoi Volume Lattice Scaffold
- Figure 4.15 Trimmed Voronoi Scaffold
- Figure 4.16 Final Mesh for Simulation
- Figure 5.1 Geometry and Voxel Size Selection Window in Ansys Additive
- Figure 5.2 Voxel Sample Rate Illustration
- Figure 5.3 Material Selection Tab in Ansys Additive with Ti6Al4V material properties
- Figure 5.4 Machine Parameters for a Typical Rotating Stripe Scan Pattern at an SLM Printer
- Figure 5.5 Blade Crash Risk Accession by Ansys Additive
- Figure 5.6 Input Variables for High Strain Areas Calculation
- Figure 5.7 Full Scaffold Lattice Displacement (mm) View 1
- Figure 5.8 Full Scaffold Lattice Displacement (mm) View 2
- Figure 5.9 Full Scaffold Lattice Displacement (mm) View 3
- Figure 5.10 Full Scaffold Lattice End-state von Mises Stress (MPa)
- Figure 5.11 Full Scaffold Lattice End-state von Mises Stress (MPa) Zoomed in View
- Figure 5.12 Full Scaffold Lattice End-state von Mises Stress (MPa) Histogram
- Figure 5.13 Full Scaffold Lattice Potential Blade Crash Locations
- Figure 5.14 Full Scaffold Lattice Potential Blade Crash Locations Zoomed in view
- Figure 5.15 Full Scaffold Lattice High Strain Severity Locations
- Figure 5.16 Sliced Scaffold Lattice Displacement (mm) View 1
- Figure 5.17 Sliced Scaffold Lattice Displacement (mm) View 2
- Figure 5.18 Sliced Scaffold Lattice End-state von Mises Stress (MPa) View 1

- Figure 5.19 Sliced Scaffold Lattice End-state von Mises Stress (MPa) View 2
- Figure 5.20 Sliced Scaffold Lattice End-state von Mises Stress (MPa) Histogram
- Figure 5.21 Sliced Scaffold Lattice Potential Blade Crash Locations
- Figure 5.22 Sliced Scaffold Lattice High Strain Severity Locations
- Figure 5.23 Cube Shaped Lattice Mesh
- Figure 5.24 Cube Lattice Displacement (mm) Comparison for Variable Laser Power View 1
- Figure 5.25 Cube Lattice Displacement (mm) Comparison for Variable Laser Power View 2
- Figure 5.26 Cube Lattice Max von Mises Stress (MPa) Comparison for Variable Laser Power
- Figure 5.27 Cube Lattice Potential Blade Crash Locations Comparison for Variable Laser Power
- Figure 5.28 Cube Lattice High Strain Severity Locations Comparison for Variable Laser Power
- Figure 5.29 Cube Lattice Displacement (mm) Comparison for Variable Laser Width
- Figure 5.30 Cube Lattice Max von Mises Stress (MPa) Comparison for Variable Laser Width
- Figure 5.31 Cube Lattice Potential Blade Crash Locations Comparison for Variable Laser Width
- Figure 5.32 Cube Lattice High Strain Severity Locations Comparison for Variable Laser Width
- Figure 5.33 Cube Lattice Displacement (mm) Comparison for Variable Layer Height View 1
- Figure 5.34 Cube Lattice Displacement (mm) Comparison for Variable Layer Height View 2
- Figure 5.35 Cube Lattice Max von Mises Stress (MPa) Comparison for Variable Layer Height
- Figure 5.36 Cube Lattice Potential Blade Crash Locations Comparison for Variable Layer Height
- Figure 5.37 Cube Lattice High Strain Severity Locations Comparison for Variable Layer Height
- Figure 5.38 Cube Lattice Displacement (mm) Comparison for Variable Scan Speed View 1
- Figure 5.39 Cube Lattice Displacement (mm) Comparison for Variable Scan Speed View 2
- Figure 5.40 Cube Lattice Max von Mises Stress (MPa) Comparison for Variable Scan Speed
- Figure 5.41 Cube Lattice Potential Blade Crash Locations Comparison for Variable Scan Speed
- Figure 5.42 Cube Lattice High Strain Severity Locations Comparison for Variable Scan Speed

1. Introduction

Any kind of damage or break in a bone's regular structure is called a bone defect. Several conditions, including trauma, infection, tumor growth, and some disorders like osteoporosis that induce bone loss, can result in this. The size, location, and impact of bone defects can vary significantly, and they can have a major effect on the bone's structural integrity and functionality. Affected individuals may experience pain and a decline in quality of life if the defect affects their ability of motion, depending on the extent and location.

The human body's natural ability to repair and cure bone may not always be sufficient especially in larger defects, patients with compromised immune systems and older individuals. In such cases, medical intervention is required to restore function and maintain the patient's quality of life.

2. Femur Bone Defect Literature Review

2.1 Femur Bone Anatomy

The femur is the only bone located in the thigh and it is the longest, heaviest, and strongest bone in the body.

It consists of three parts: proximal, shaft, and distal. It serves as the origin and attachment point for many muscles and ligaments.



Figure 2.1 Femur Bone Regions

The proximal end is the uppermost part of the femur that articulates with the acetabulum of the pelvis to form the hip joint. It consists of a head and neck, and two bony processes called the greater and lesser trochanters. The two trochanters are connected posteriorly by two bony ridges, the intertrochanteric line anteriorly and the trochanteric crest posteriorly. Several muscles attach to these bony protrusions to enable hip joint mobility.

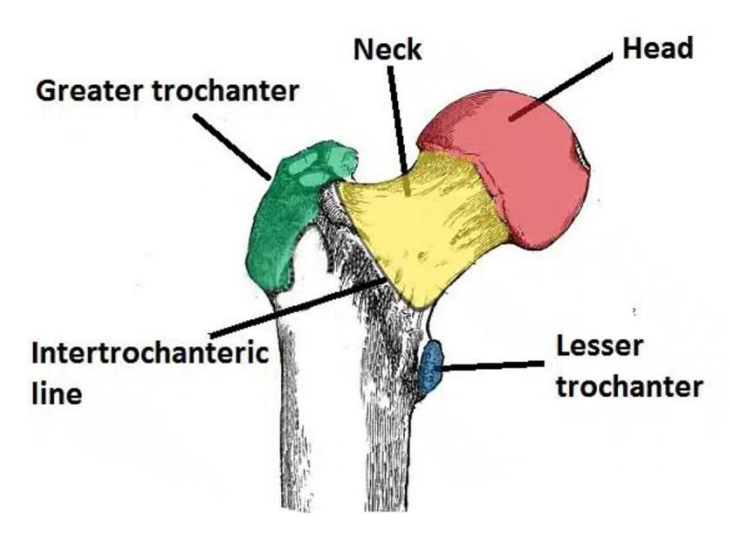


Figure 2.2 Femur Proximal End

Femur Neck fractures are most commonly observed in the elderly population especially in women, as a result of low energy falls along with preexisting osteoporosis. In younger patients they tend to occur as a result of high energy accidents.

The femoral shaft is the long mostly straight part of the femur bone. It descends in a slight medial direction in order to bring the knees closer to the body's center of gravity, increasing stability. The midsection of the shaft has a circular cross section, but the proximal and distal ends are posteriorly flattened.

Femoral shaft fractures are usually high energy injuries, however they can also occur in the elderly as a result of a low energy fall. They can result in the loss of leg length due to the bony fragments overriding, pulled compressively by their attached muscles. Since femoral shaft fractures are high energy, the surrounding tissues can also be damaged with considerable hemorrhaging often occurring.

The Distal end is the lower part of the femur bone. It features the medial and lateral condyles, which connect with the tibia and patella to create the knee joint. The medial and lateral condyles are rounded structures located at the end of the femur. Their posterior and inferior surfaces connect with the tibia and menisci of the knee, while the anterior surface interacts with the patella. The larger lateral condyle plays a key role in preventing the natural lateral movement of the patella, as a flatter condyle increases the risk of patellar dislocation. There are also two bony elevations on the non-articular areas of the condyles, the medial and lateral epicondyles from where the medial and lateral collateral ligaments of the knee originate. Lastly the deep notch between the two condyles is named Intercondylar fossa is the anchoring point of the anterior cruciate ligament (ACL) and the posterior cruciate ligament (PCL), the most commonly injured ligaments among athletes.

Fractures of the distal femur are severe and medical management and treatment are difficult. The participation of the distal end in the formation of the knee joint, the most complicated joint found in the human body, makes a non-surgical approach in the treatment of such fractures a rare option [1].

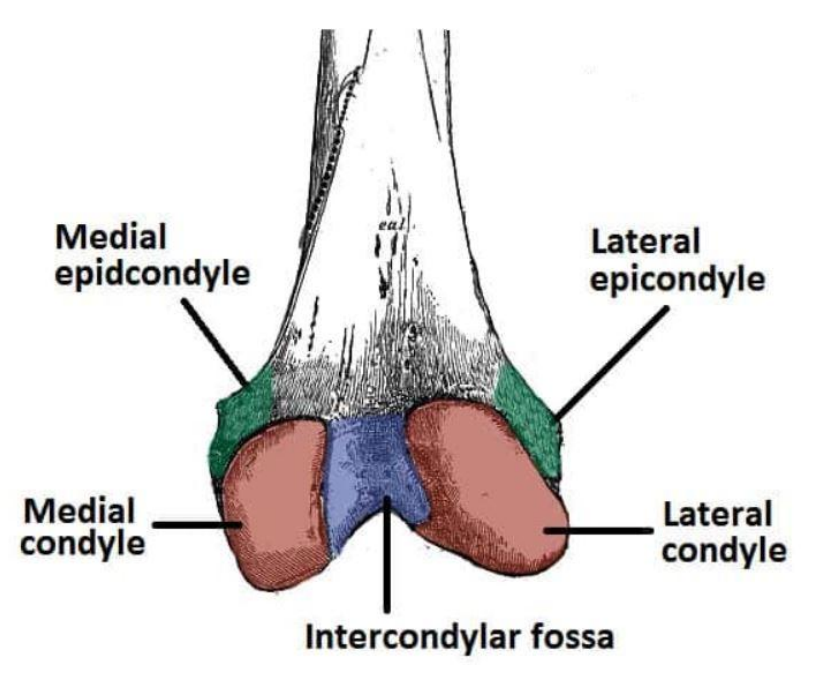


Figure 2.3 Femur Distal End [6]

2.2 Bone Healing Process - Association with Strain

The process of bone fracture healing is complex and involves a seamless regenerative process to restore the damaged bone to its original state and cellular makeup. When a fracture occurs, it results in a break in the structural integrity of the bone cortex and causes varying levels of damage to the surrounding soft tissues. After the fracture, the secondary healing process commences, involving four distinct stages.

Hematoma Formation: (Immediately after the fracture)

This is a crucial stage in the healing process of a fracture. The fracture disrupts the blood supply to the bone and periosteum, leading to the formation of a hematoma at the site of the fracture, which contains a large number of hematopoietic cells. The hematoma coagulates and serves as the temporary framework for the healing process that follows.

Granulation Tissue Formation: (Within two weeks)

In this step an inflammatory response is initiated by the platelets flooding the injury site. Following that, other mesenchymal cells and inflammatory cells, like fibroblasts and endothelial cells, are called to the fracture area, leading to the formation of granulation tissue rich in fibrin and angiogenesis. The granulation tissue withstands the greatest strain prior to failure during the healing process.

Bony Callus Formation (If bone ends are not in contact, then a soft bridging callus forms):

The granulation tissue is gradually substituted by a callus, which acts as a connection of new bone linking the fractured ends of the bone. The initially soft callus made of cartilage starts to undergo endochondral ossification, and a medullary callus provides further support to the soft callus that bridges the gap. Consequently, the cartilaginous callus is absorbed and begins to calcify. Woven bone continues to be deposited subperiosteally. The newly formed blood vessels continue to grow, facilitating the further migration of mesenchymal stem cells. Ultimately, at the conclusion of this phase, an immature bone callus composed of rigid, calcified tissue develops. The development of bone callus depends on the suitable relative movement between fracture segments.

Bone Remodeling: (Continues for months to years after clinical union)

This is the final process of bone healing and involves a complex interaction of signaling pathways, resulting in the middle of the callus is eventually substituted with compact bone, with the callus borders being replaced by lamellar bone. Significant changes occur in the vasculature during this process. The bone remodeling process continues for several months, leading to the restoration of the typical bone structure [2].

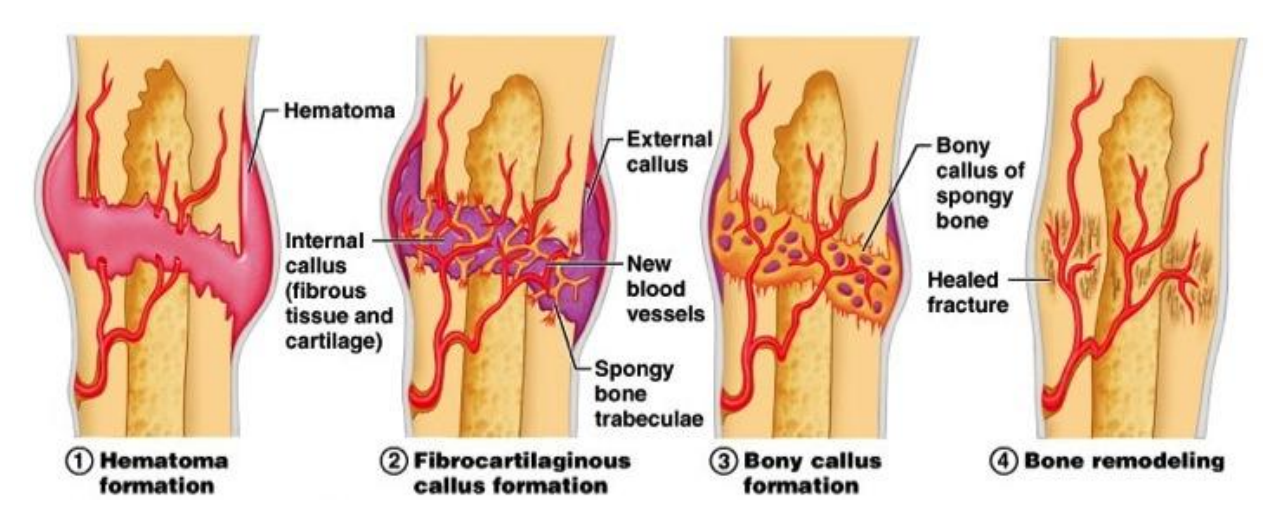


Figure 2.4 Bone Healing Process [3]

As we already mentioned the process of bone fracture healing is complex and thus affected by some external factors one of which are mechanical loads. Bones are dynamic tissues that constantly remodel in response to mechanical loads, especially during the healing period. These loads are the cause of mechanical strain a fundamental concept in biomechanics that refers to the degree of deformation experienced by a material or tissue in response to an applied force. Strain is typically expressed as a ratio of the change in length (deformation) to the original length of the material. It is a dimensionless quantity because it represents a percentage change relative to the original size.

The achievement of the ideal strain amount is critical for an efficient and strong fracture heal. Low amounts of strain (<2%) leads to a lack of mechanical stimulation, which can result in poor bone formation and delayed healing. This is especially a concern with overly rigid fixation devices or immobility during healing. Only in the primary stages of bone healing such low amounts of strain can be beneficial, to let the body form the hematoma and start the inflammatory response. Moderate strain (2-10%) promotes the formation of the callus and aids in the differentiation of stem cells into osteoblasts. This range is associated with the most effective healing process in the secondary bone healing phase. High Strain (>10%) can lead to delayed healing or non-union (when the bone fails to heal properly). High strain levels can cause the newly formed bone tissue or callus to break down, leading to complications or instability at the fracture site [4].

In the management of distal femur fractures doctors control the strain through several techniques in order to avoid complications like non-union or implant failure. Doctors achieve this primarily by selecting the right fixation device, adjusting the bone gap during surgery, and setting weight-bearing limitations for the patient. Partial or non-weight-bearing protocols are enforced during the early stages of recovery, as the fracture begins to heal and gradually increased weight-bearing is allowed, which incrementally increases the strain on the bone and encourages bone remodeling [5].

2.3 Conventional Treatment Methods of Distal Femur Fractures

The treatment of distal femur fractures typically depends on the severity of the fracture, the patient's overall health, and the type of fracture (simple or complex). When there is significant bone loss, the primary conventional methods are non-surgical treatment, surgical fixation techniques, and bone grafting. When treating distal femur fractures, non-surgical techniques are uncommon and are usually reserved for stable fractures—those in which the bone fragments are still in

alignment—or for patients for whom surgery may be extremely risky, such as the elderly or those with specific medical conditions. Non-displaced or minimally displaced fractures may be treated with casting or functional bracing. Immobilizing the fracture and letting the bone heal on its own are the objectives. In order to stabilize the joint and limit movement, casts are usually placed from the upper thigh to the ankle. Though less common these days, traction can still be used in certain situations, such as when surgery is not immediately feasible. To realign the bone fragments, a constant pulling force is applied. Traction an also be used temporarily prior to surgery.

Surgery is the most common approach for treating distal femur fractures, particularly for displaced, open, or complex fractures. The regions complex anatomy and muscle activity more often than not, lead to bone fragments misalignment and instability requiring surgical intervention. The two main fixation techniques implemented are **Locking plates with screws** and **intramedullary nailing**.

Locking plates are frequently employed in surgical interventions for distal femur fractures, especially in instances of complex or comminuted fractures characterized by many bone pieces, as well as in patients exhibiting compromised bone quality, such as individuals with osteoporosis. These plates feature screw holes that enable locking screws to firmly attach into both the plate and the bone, establishing a strong, fixed-angle construct that ensures stability even in compromised bones. Locking plates are particularly advantageous for fractures next to joints, such as the knee, where conventional plating may lack sufficient support. Locking plates facilitate appropriate alignment and enhance bone healing by minimizing the displacement of bone fragments and maintaining blood supply, hence decreasing the likelihood of non-union or malunion.

Intramedullary nails are inserted into the marrow canal of the femur. They provide strong internal support, particularly for fractures in the shaft or more proximal areas of the distal femur. Two primary methods of intramedullary nailing are commonly employed: Antegrade and Retrograde nailing. Retrograde nailing includes the insertion of the nail via the distal segment of the bone, usually via the knee joint for femoral fractures, and extending it superiorly into the medullary canal. This technique is frequently employed for fractures located toward the distal end and is beneficial when the patient has simultaneous hip or pelvic injuries, as it prevents additional disturbance to the hip region. It offers robust stability for distal femur fractures.



Figure 2.5 Femur Bone Retrograde Nailing Technique [7]

Antegrade nailing, on the other hand, involves inserting the nail from the superior aspect of the femur into the medullary canal, initially traversing the hip region. This procedure is typically employed for fractures in the mid-shaft or

upper region of the femur. While both methods assist in aligning and stabilizing the bone, the fracture location and any concurrent injuries will dictate the choice between retrograde and antegrade nailing techniques [5].



Figure 2.6 Femur Bone Antegrade Nailing Technique [8]

2.4 3D Printed Bone Implants - Materials and Design

Bone typically exhibits a strong innate ability to regenerate. However, in cases presenting with large defects with great amounts of bone loss, the treatment is still a considerable clinical challenge. In these cases, Scaffold-based biomimetic bone substitutes are designed to replicate the structural, mechanical, and biological characteristics of bone, providing a replacement for missing tissue [9].

The scaffold material should form a mechanically stable contact with the bone and also have the ability to aid bone tissue growth on its surface and through its pores. To fulfill these requirements, various scaffold properties, such as material composition and spatial organization, need to be considered and carefully balanced. Also, the materials that are used in such scaffolds need to be sufficiently biocompatible. Biocompatibility refers to the capacity of a biomaterial to perform its intended function in a medical therapy without causing adverse local or systemic reactions in the patient while simultaneously achieving the highest possible level of clinical effectiveness [10].

Because of the aforementioned parameters the material choice for bone replacing scaffolds is a challenging task. As a result, the bone matrix remains the most effective material for regenerative approaches in bone repair. Unfortunately, the use of autologous bone grafts in the treatment of femur defects is impossible as the injuries of the femur demanding the implantable scaffold approach, present great amounts of bone loss. The use of allogenic bone grafts is more suitable for larger defects but it comes with some drawbacks allografts have. To mitigate the risk of disease transmission, allografts must undergo sterilization to eliminate pathogens or deproteinization to reduce immunogenic reactions and the chances of the implanted scaffold getting rejected. However, these processes can compromise their structural integrity and also reduce the osteogenic properties of the implant [11].

Due to the limitations associated with bone grafts, the attention is shifting to natural or synthetic materials utilized as bone substitutes. The manufacturing of custom porous scaffolds that both provide the appropriate mechanical support and also allow for cell in-growth is being studied extensively and one of the most promising manufacturing methods is

3D-Printing. Subsequently we are going to briefly present the most commonly used materials in the manufacturing of such bone mimicking porous scaffold, used in different methods of 3D-Printing [12].

1. Metals and Alloys

Metals are chosen for the manufacturing of bone scaffolds because of their superior mechanical strength. The most common metals used are:

- **Titanium** it's Alloys (such as Ti6Al4V) is a non-biodegradable metal that exhibits excellent mechanical strength and biocompatibility.
- Magnesium (Mg) and it's Alloys are biodegradable and promote cell growth, but attention is needed in the control of their degradation process.
- **Cobalt-Chromium** Alloys are non-biodegradable and less osteoconductive than titanium but present good mechanical properties.
- **Stainless steel** (alloy of iron, chromium, and nickel) is a cheaper option, it's not biodegradable and its main use is for temporary scaffolds or implants.

2. Bioceramics

Bioceramics are inorganic materials composed of calcium and phosphorus salts, along with chemically and heattreated metals such as titanium and tantalum, which possess a degree of osteoinductive capability. The most common are:

- **Hydroxyapatite (HA)** is a bioceramic that closely resembles the mineral component of bone, providing excellent biocompatibility and osteoconductivity, although it is non-biodegradable.
- **Tricalcium phosphate (TCP)** is another calcium phosphate ceramic that is biodegradable and supports bone regeneration by gradually resorbing in the body.
- **Bioactive glass** is a silicate-based material known for its ability to bond with bone and stimulate hydroxyapatite formation on its surface, enhancing bioactivity.
- **Calcium silicates** are synthetic materials that release bioactive ions, promoting bone formation and offering partial biodegradability.

3. Synthetic Polymer Materials

Synthetic Polymer Materials are engineered polymers that offer tunable properties and mechanical strength. The most common synthetic polymers used for the manufacturing of bone scaffolds are:

- **Polycaprolactone (PCL)** which is a biodegradable polyester with excellent mechanical strength and slow degradation, making it suitable for long-term scaffolds.
- **Polylactic acid (PLA)** is a biodegradable polymer derived from renewable resources, known for its rigidity and ease of fabrication, although it is more brittle compared to other options.
- **Poly-lactic-co-glycolic acid (PLGA)** is a copolymer of lactic acid and glycolic acid, offering tunable degradation rates and wide application in bone regeneration.
- **Polyethylene glycol (PEG)** is a synthetic polymer used to create hydrogels, offering biodegradability and flexibility for softer scaffold designs.

4. Natural Materials

These materials are derived from biological sources thus being inherently biocompatible and some examples of them are:

• **Collagen** is the primary structural protein in the extracellular matrix of bone, offering excellent biocompatibility and promoting cell adhesion, differentiation, and osteogenesis, making it a fundamental choice for bone scaffold construction.

- **Chitosan**, derived from chitin in shellfish exoskeletons, is biodegradable, antimicrobial, and often used as a composite with ceramics to improve mechanical properties and bioactivity.
- **Alginate**, extracted from seaweed, provides a gel-like consistency that supports cell encapsulation, but it requires crosslinking to achieve adequate mechanical stability for bone applications.
- **Gelatin** is a hydrolyzed form of collagen and it is widely used for bioinks in 3D printing due to its biocompatibility and ability to mimic the bone microenvironment.
- **Silk fibroin**, obtained from silkworm cocoons, is notable for its combination of strength, flexibility, and slow biodegradability, making it an excellent choice for scaffolds requiring structural integrity and controlled degradation.

These materials are often combined with synthetic polymers or ceramics to create hybrid scaffolds that balance mechanical strength, biodegradability, and bioactivity, enabling more effective bone regeneration.

3. 3D Printing Overview

3.1 Additive manufacturing Process

3D printing is an additive manufacturing technology that in most cases creates three-dimensional objects layer by layer from digital designs. It enables the production of complex geometries that would otherwise be challenging or impossible to manufacture with traditional manufacturing techniques. This technology finds numerous applications across diverse fields, including healthcare, with specific relevance in medical sectors like tissue engineering and prosthetics.

3.2 Non-Metallic Materials 3D Printing

The most common methods of 3D printing Non-metallic materials are the following [13]:

- 1. **Fused Deposition Modeling (FDM):** This method uses thermoplastic filaments like PLA, ABS, and PCL, which are melted and extruded layer by layer. FDM is widely used for prototyping and low-cost manufacturing.
- 2. **Stereolithography (SLA)**: SLA uses liquid photopolymer resins cured with a UV laser to produce highly detailed and smooth objects. It is suitable for biocompatible and dental materials.
- 3. **Digital Light Processing (DLP)**: Similar to SLA, DLP uses a digital light projector to cure resin, often producing faster and more precise results.
- 4. **Selective Laser Sintering (SLS)**: SLS uses a laser to sinter powdered materials such as nylon, polyamide, or glass-filled composites. It is valued for its strength and ability to handle complex geometries.
- 5. **Material Jetting (MJ)**: In this method, liquid photopolymers are deposited and cured layer by layer, allowing for multi-material printing with exceptional surface finishes.

3.3 Metal 3D printing

Metal 3D printing involves using a heat source, such as a laser or an electron beam, to fuse or melt the material together. For metal 3D printing, the following methods are commonly used:

- 1. **Selective Laser Sintering (SLS)**: Employs a laser to sinter metal powders into solid structures, suitable for rapid prototyping and lightweight designs.
- 2. **Selective Laser Melting (SLM)**: Uses a high-power laser to fully melt metal powders, producing dense and strong parts.
- 3. **Electron Beam Melting (EBM)**: Utilizes an electron beam instead of a laser to melt metal powders, typically in a vacuum, and is commonly used for titanium alloys and aerospace applications.
- 4. **Direct Metal Laser Sintering (DMLS)**: DMLS is similar to SLS, SLM but operates at slightly lower energy levels, utilizing one or more fiber lasers to sinter metal powders together.

3.4 3D Printing Microstructure Lattices in Bone Imitating Implants

When focusing on metal 3D printing methods for producing bone-imitating microstructure implants, it is essential to evaluate the ability of the technology to replicate intricate microarchitectures, biocompatibility, mechanical strength, and cost-effectiveness. The femur bone experiences significant mechanical loads, making metal scaffolds particularly well-suited for addressing defects in this bone. Consequently, metal 3D printing is an optimal technique for producing implantable scaffolds that mimic bone structure. Below is a comparison between the most common metal 3D printing methods:

SLS uses a laser beam to sinter metal powders together, not melt them, thus the resulting prints present limited strength compared to other methods. The compromised mechanical strength is undesirable to our specific application as the femur bone experiences substantial mechanical loads. DMLS is also a sintering process but work closer to the melting point of metal powders, producing better results as far as mechanical strength is considered. On the downside, DMLS machines are more expensive to acquire, require more energy to run, and typically have less build volumes then SLS machines.

When comparing EBM with SLM printing processes, some important differences are observed. EBM printing utilizes an electron beam to melt the metal powder together while an SLM printing machine does the same by using one or more high power laser beams. This means that EBM printing is conducted in vacuum while SLM printing only needs an inert gas layer above the metal powder to prevent it from oxidizing when melted by the laser beam. The electron beam of an EBM printer is thicker than a laser beam, leading to EBM being less accurate than SLM printing. Typically, the layer height of EBM is around 70 microns when in SLM it can be as small as 20 microns and the minimum recommended feature size for EBM is more than 100 microns when in SLM printers it can be as small as 50 microns. Despite the above, an EBM 3D printer is more affordable than the equivalent SLM, and also faster at printing [14], [15].

In conclusion, for bone-imitating microstructure implants, **SLM** and **DMLS** are preferred for their precision and strength, while EBM is advantageous for its speed, and less expensive machine. In the next paragraph we are going to explain in more detail how **SLM** metal 3D printing works, as in the following chapters we are going to simulate the manufacturing process of such a scaffold, using the **Additive** application from the **Ansys 2024 Suite**.

3.5 Selective Laser Melting (SLM) for Implantable Bone Scaffolds

As we explained, SLM printing is one of the most precise additive manufacturing techniques resulting in it being the preferred manufacturing method for creating highly detailed and complex structures such as micro structured implantable bone scaffolds. The process begins with the deposition of a thin layer of metal powder (typically 20–60 microns thick—across the build platform using a recoater blade. A high-energy laser scans specific areas of the powder bed based on a digital CAD model, melting and fusing the powder into a solid structure. The build platform subsequently descends by the layer thickness, and a fresh layer of powder is distributed, repeating the procedure until the item is completely constructed. SLM operates within a regulated inert gas atmosphere, such as argon or nitrogen, to avert oxidation. A primary issue in SLM is achieving consistent melting and solidification of powders, necessitating careful control of laser parameters, including power, scan speed, and focus. Residual stresses resulting from quick thermal cycles can cause warping or cracking in intricate geometries, rendering post-processing procedures such as stress-relief annealing essential for preserving mechanical integrity.

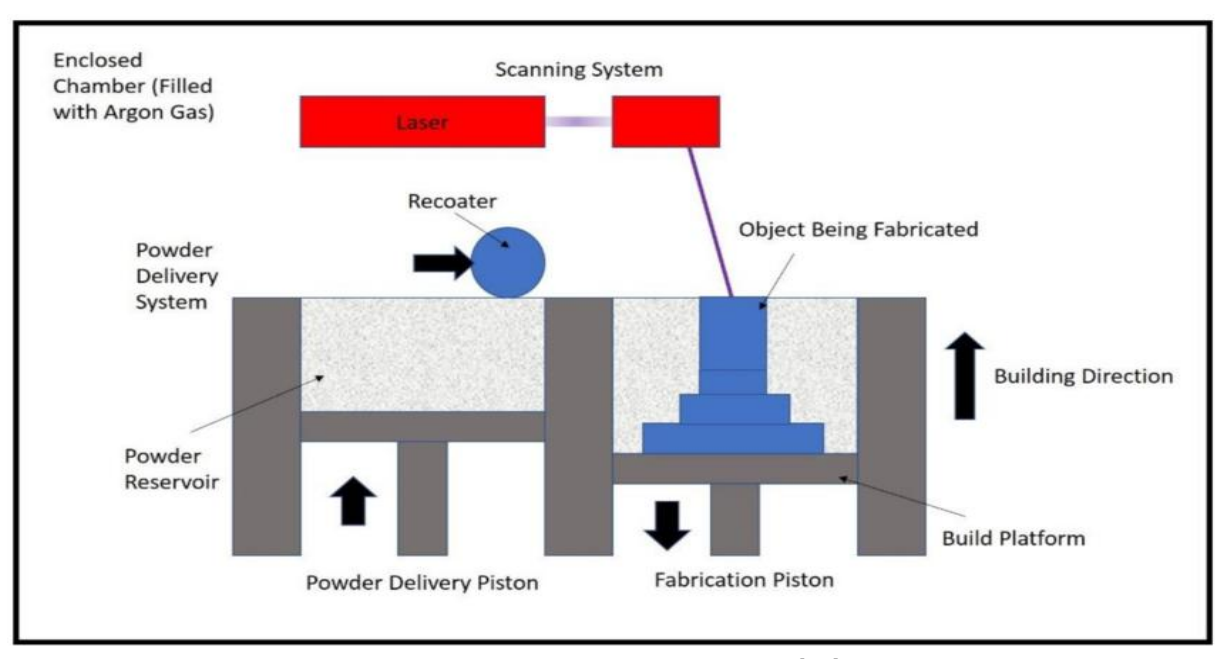


Figure 3.1 SLM 3D Printing Schematic [16]

SLM is particularly suited for biomedical applications due to its ability to fabricate complex, porous, and patient-specific structures while presenting a good variety of materials to be used. Cobalt-chromium, stainless steel, aluminum alloys, titanium and its alloys (such as Ti-6Al-4V), and other materials are frequently utilized. Particularly preferred for bone-imitating scaffolds are titanium alloys due to their superior biocompatibility, resistance to corrosion, and mechanical characteristics that closely resemble those of natural bone. These scaffolds often feature intricate lattice structures designed to replicate trabecular bone, enabling cell adhesion, vascularization, and overall promoting osteogenesis. All of the above makes SLM a great technology for producing advanced orthopedic implants, meeting the demands for both functionality and biological compatibility.

4. Structured Scaffold CAD Design

4.1 From CT scan to CAD Model

4.1.1 Processing and Refinement

To determine the appropriate implant design, a patient specific analysis is required, starting from the CT scan of the affected bone area and ending with the basic CAD model of the implant. To achieve that we followed the steps below:

1. Initial Processing in 3D Slicer:

The first step in converting the CT scan into a bone implant CAD model was to process the raw medical imaging data using 3D Slicer. This open-source software allowed us to extract a 3D surface mesh from the grayscale CT scan. Since CT scans capture a vast amount of anatomical detail, including surrounding tissues, it was necessary to isolate the bone structure using threshold segmentation. To refine our selection, we utilized the "Island" and "Cut" command tools, in order to remove any unnecessary parts and artifacts of the scan that did not belong to the femur. The "Island" command works by separating individual connected regions, allowing us to discard unwanted structures, while the "Cut" tool is used to trim excess areas, further helping us to refine the geometry. This process resulted in a rough STL mesh file, which represented the outer surface of the bone with reasonable accuracy but still contained imperfections that required further processing in the following steps.

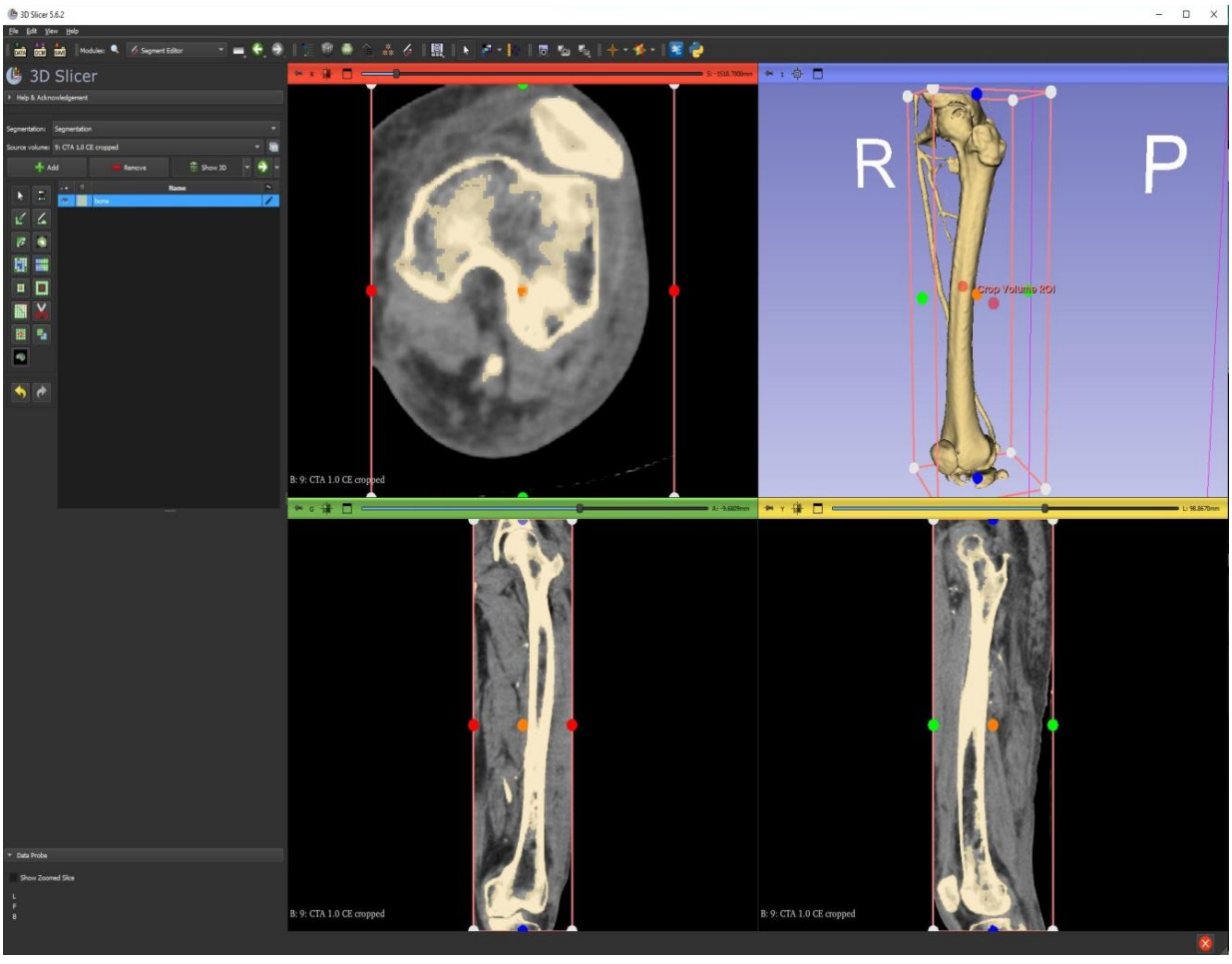


Figure 4.1 3D Slicer Working Environment

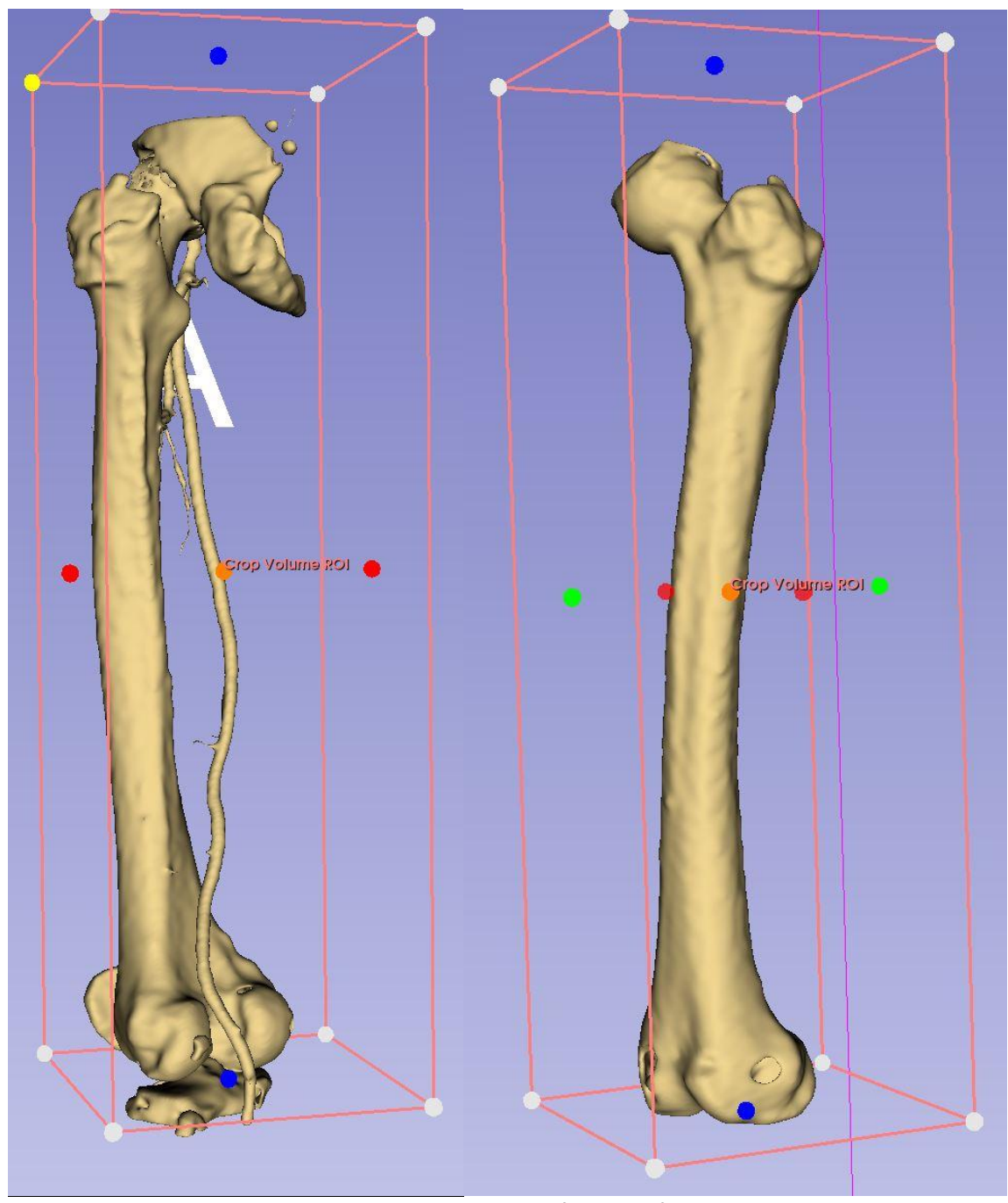


Figure 4.2 3D Slicer Femur Bone Before and After Trimming

2. Mesh Refinement in Blender:

For the next step, we imported the rough STL mesh from Slicer into Blender for refinement and improvement. Prior to further processing, the original mesh had to be fixed because it had holes, jagged surfaces, and other irregularities.

Firstly, we applied the Remesh modifier, which helped redefine the topology and create a more uniform structure by replacing the irregular triangles with an even quadrilateral mesh. This step ensured that the mesh was easier to work with, smaller in size, better suited for modifications and improved on its structural integrity. Next, using Blender's sculpting tools, we manually filled gaps and smoothed rough surfaces to eliminate noise and inconsistencies introduced during the segmentation process.

To create the bone marrow cavity, we utilized the Displace modifier, which simulates organic deformations by pushing or pulling mesh surfaces along a specified axis. By carefully adjusting displacement values, we sculpted a

realistic internal cavity, accurate enough for our simulation purposes. Finally, in order to ensure a structurally complete and watertight mesh that could be converted into a solid CAD model, the last step in Blender was to join the outer bone surface with the newly created marrow cavity.

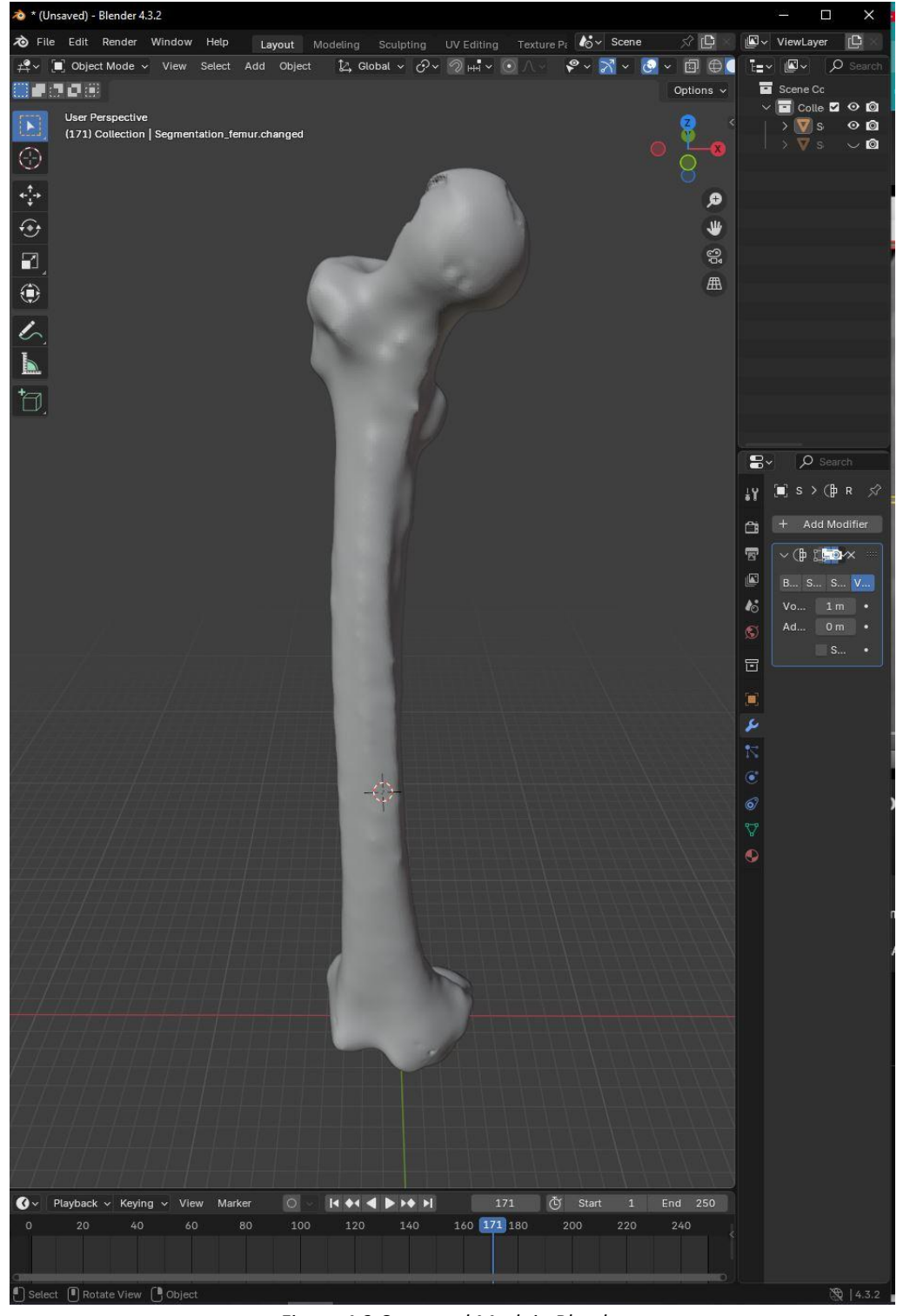


Figure 4.3 Corrected Mesh in Blender

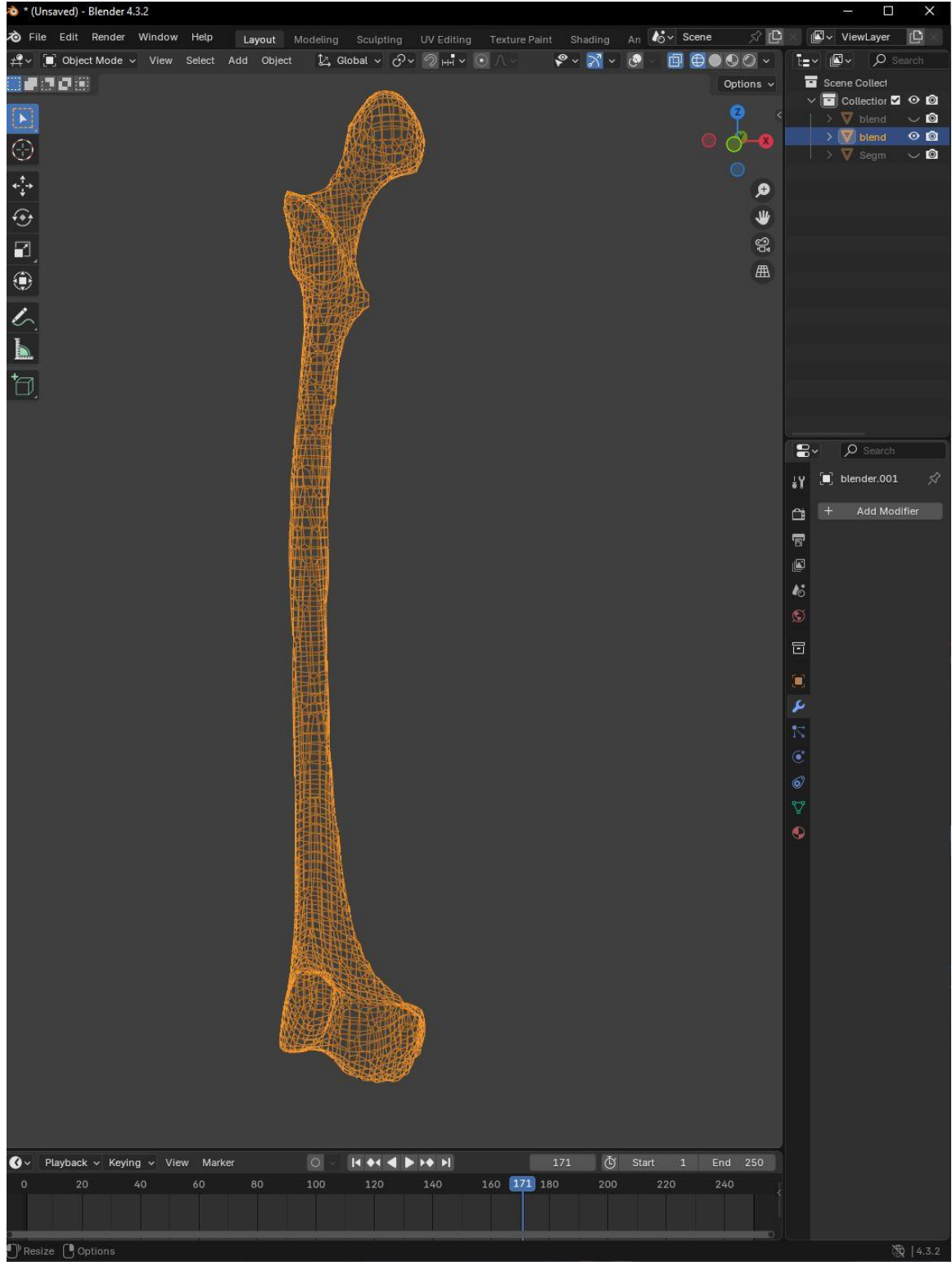


Figure 4.4 Bone Marrow and Spongy Bone Cavity Mesh in Blender

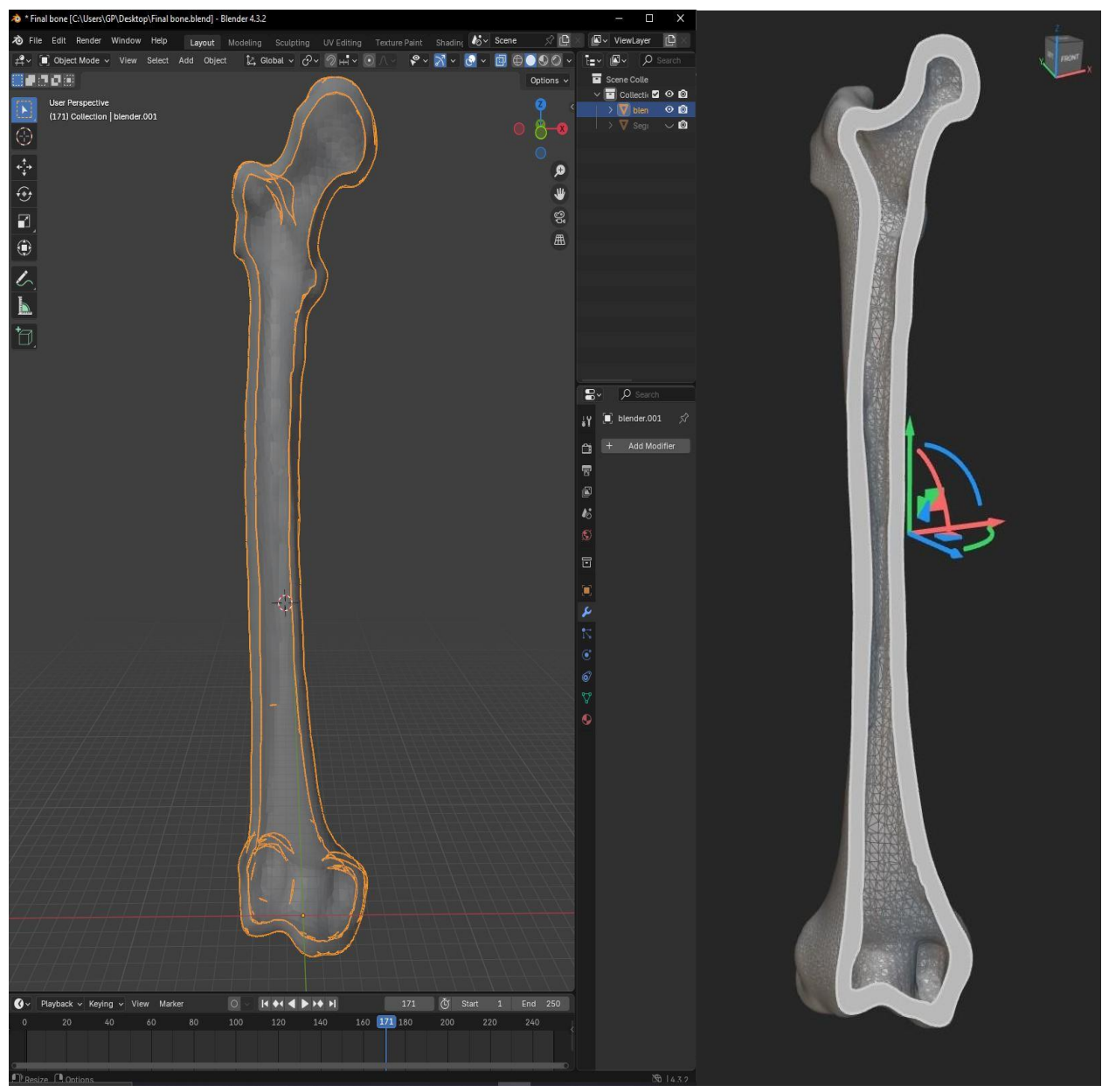


Figure 4.5 Final Bone Mesh Model in Blender with Section View

3. Converting the Mesh to a Solid CAD Model in NTop:

With the cleaned and enhanced STL mesh from Blender, we moved to NTop (nTopology) to transform the mesh into a solid CAD model. With a series of conversions shown in the picture below we managed to convert the mesh we got from Blender to a CAD file that we can then use in Solidworks to execute more accurate parametric operations.

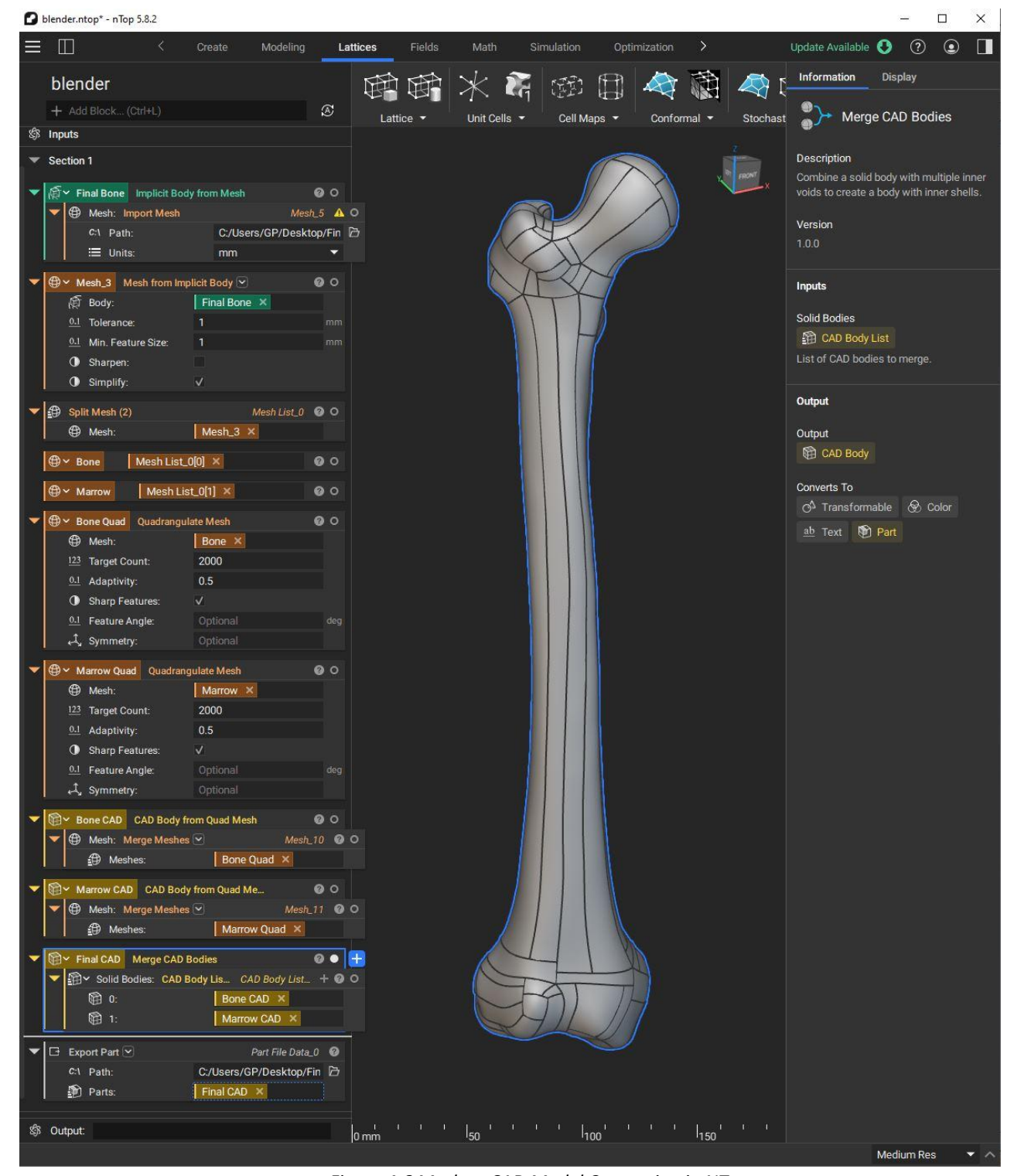


Figure 4.6 Mesh to CAD Model Conversion in NTop

4. Cutting the final implant in SolidWorks:

Once the solid CAD model was generated in NTop, we imported it into SolidWorks to finalize the bone implant design. In this phase, we determined the optimal cut locations to shape the implant into its final form.

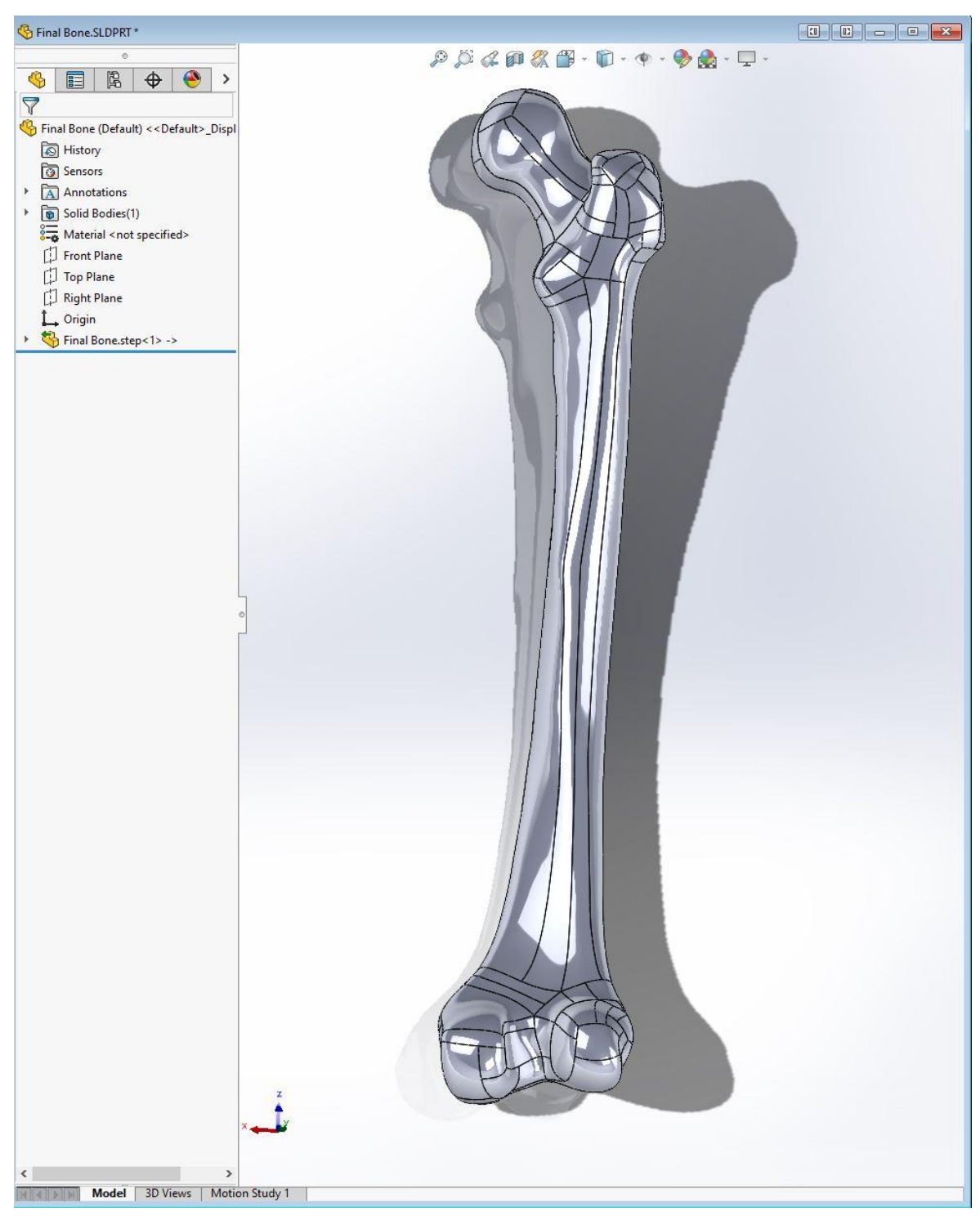


Figure 4.7 Importing Femur Bone CAD Model in Solidworks

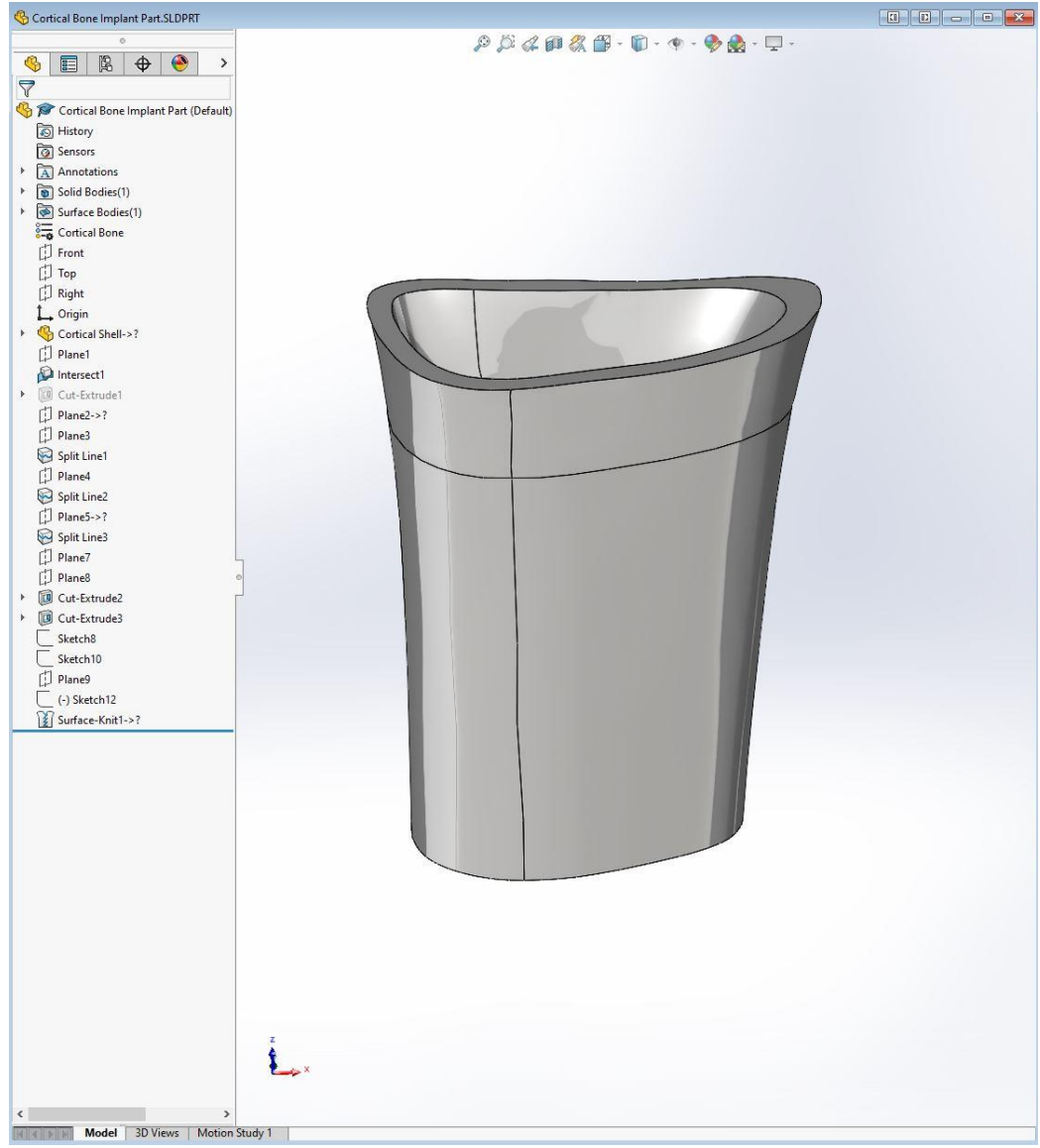


Figure 4.8 Final Implant Geometry Derived from CAD Model

To summarize, we were able to successfully transform a CT scan into a highly accurate, CAD model for a bone implant that could be manufactured thanks to this multi-step process. We produced an exact design that was prepared to serve as the foundation for our SLM printing simulations by utilizing 3D Slicer for the initial segmentation, Blender for mesh repair and cavity creation, NTop for CAD conversion, and SolidWorks for the final implant geometry.

4.1.2 Rationale for Excluding Spongy Bone

We have to note that in our 3D model of the bone scaffold, we chose not to include cancellous or spongy bone for several important reasons, based in both practical considerations and biological principles. Cancellous bone, has a highly porous and intricate architecture that is challenging to accurately model and simulate in 3D printing, demanding even longer computational time and resources. Our scaffold design's main objective is to create the conditions necessary for effective bone regeneration while offering structural support that replicates the mechanical characteristics of solid, cortical bone. However, spongy bone contributes less to overall mechanical stability and acts as a shock absorber and bone marrow reservoir. From a biological standpoint, the scaffold design's exclusion of spongy bone is consistent with the body's inherent regeneration and healing mechanisms. Because of its vascularized structure, spongy bone has a high capacity for self-healing. Using a scaffold to try to replicate spongy bone could impede this natural regeneration thus ending up doing more harm than good. Research supports the idea that allowing the immune system and osteogenic

cells to regenerate spongy bone leads to better integration and functionality of the implant [25]. In a nutshell a combination of clinical, biological, and practical factors led us to decide against modeling or simulating cancellous bone. This method guarantees that our scaffold design maintains computational efficiency, promotes natural healing processes, and prioritizes structural integrity, all of which improve patient outcomes.

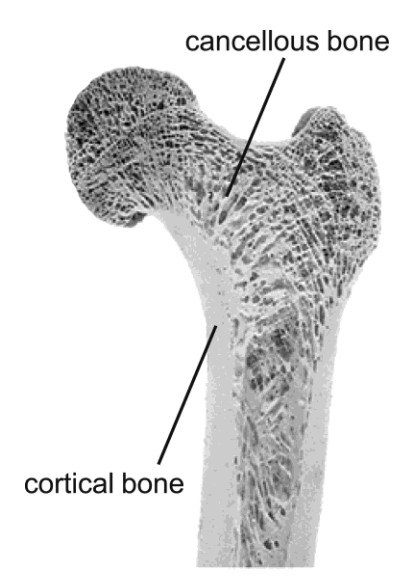


Figure 4.9 Femur Bone Proximal End Microstructure [17]

4.2 Unit Cell to Porous Scaffold

In this chapter, we address bone defect management by introducing porosity into these implantable scaffolds. To discover the best solutions for efficient bone treatment, a thorough investigation of scaffold design is presented considering unit cell geometry, size, thickness, and porosity to determine the most optimal microstructure for effective bone treatment.

Unit cells can be generally categorized into stochastic and deterministic designs, each with distinct characteristics and applications.

1. Deterministic Unit Cells:

These unit cells have regular and repeatable geometries, such as cubic, gyroid, diamond, or Schwartz primitives. These designs are ideal for load-bearing uses, these designs provide consistent stiffness and uniform stress distribution, so providing predictable mechanical characteristics. Deterministic structures also allow for precise control over porosity and mechanical strength, enabling tailored scaffold properties for specific clinical needs.

2. Stochastic Unit Cells:

These are irregular and random in geometry, closely mimicking the natural trabecular structure of bone. Stochastic lattices, such as Voronoi structures, are generated based on random point distributions, resulting in heterogeneous pore sizes and arrangements. This irregularity provides enhanced biological mimicry, promoting bone ingrowth and vascularization. However, their mechanical behavior is less predictable and often requires extensive simulations to optimize them for load-bearing applications.

The most common unit cell types used for porous bone scaffolds are cubic cells, gyroid cells, diamond lattices, Voronoi structures, and Schwartz primitives. Each unit cell has its distinct mechanical behavior owing to their geometry, influencing their application in scaffolds for bone tissue engineering. The mechanical properties such as stiffness,

strength, and deformation behavior are largely affected by the unit cell's shape, porosity, and ability to distribute stress uniformly.

Cubic unit cells are among the simplest geometries, characterized by their square or rectangular arrangement. They provide a straightforward design for supporting loads but have limitations in mimicking the trabecular structure of natural bone. From a mechanical standpoint, these structures tend to be directionally dependent, showing varied stiffness and strength based on the axis of applied force. This directional weakness can lead to stress build-up in multi-directional loading environments. Still, their uncomplicated layout makes them easy to produce and useful in basic scaffold applications where design complexity is less critical.

Gyroid unit cells, with their smooth, continuous surfaces and no sharp edges, are highly effective in distributing mechanical loads. his continuous geometry helps distribute mechanical forces evenly, reducing the likelihood of weak spots forming under pressure. Because gyroids react similarly when loaded from different directions, they offer a nearly uniform mechanical response, which is ideal in applications that demand both strength and a porous structure. This balance is especially important for implants designed to encourage bone in-growth. The geometry also allows for interconnected internal spaces, which support the movement of fluids and nutrients—an important feature for promoting healing and integration with surrounding tissue.

Diamond lattice cells have the advantage of producing strong yet lightweight designs. These structures are particularly effective in scenarios where implants need to withstand considerable mechanical stress—such as in load-bearing sections of the femur. Their design offers consistent stiffness and compressive strength while preserving the open structure needed for biological compatibility In places under repeated mechanical loads, where maintaining structural integrity over time is essential, this feature is especially helpful. [18].

Schwartz primitives structures incorporate mathematically derived surfaces known for their minimal area properties. Their geometry offers a favorable blend of mechanical symmetry and high permeability, enabling both structural support and internal fluid transport. These features make them particularly appropriate in scaffold designs for bone areas rich in blood vessels. The smooth transitions in their geometry also reduce stress concentrations, contributing to enhanced fatigue resistance under cyclic loading [19].

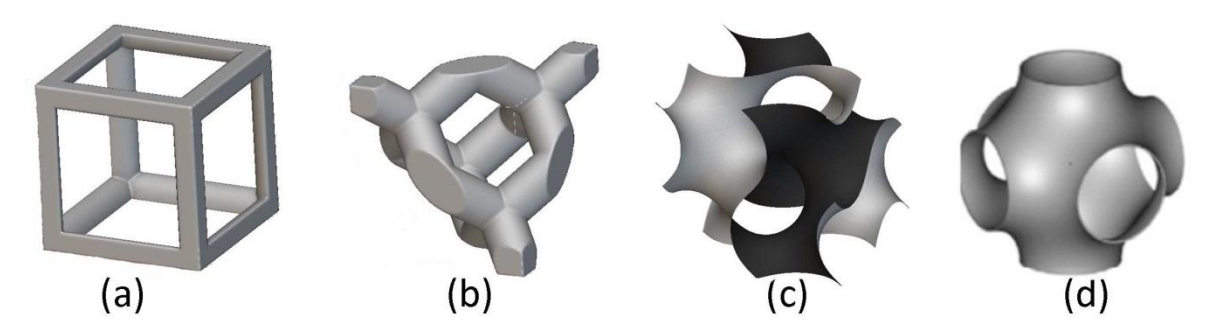


Figure 4.10 Deterministic Unit Cell Types Commonly Used in Bone Implants: (a) Cubic, (b) Diamond, (c) Gyroid, (d) Schwartz

Voronoi structures stand out for their biologically inspired, irregular geometries that closely mimic the natural trabecular structure of bone. This randomness not only enhances their ability to imitate natural bone morphology but also contributes to their mechanical performance. Voronoi scaffolds distribute stress irregularly across their structure, which can be beneficial in replicating the mechanical heterogeneity of real bone. However, this same irregularity can result in localized stress concentrations under specific loading conditions, requiring careful optimization of the structure for the intended application.

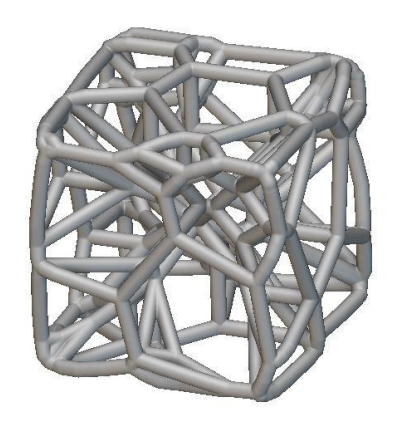


Figure 4.11 Cubic Voronoi Stochastic Lattice example

Each of these unit cell types brings unique mechanical advantages and challenges. The selection of the unit cell depends on the specific mechanical and biological requirements of the application.

4.3 Voronoi Lattice – nTopology

4.3.1 Why We Chose the Voronoi Lattice

Voronoi lattices are created using a computational process called Voronoi tessellation. This process divides a three-dimensional space into regions derived from a set of seed points. These seed points are randomly distributed within the design space, and each point generates a polyhedral cell representing all points closer to it than to any other seed. This results in a stochastic, irregular structure that closely mimics the trabecular architecture of natural bone. After tessellation, the lattice geometry is optimized to meet specific mechanical and biological requirements, such as achieving a target porosity or stiffness. The irregularity and interconnectivity of Voronoi structures make them particularly effective for bone scaffolds, as they allow for high permeability, facilitating cell infiltration and nutrient flow. Advanced computational tools, such as nTop Platform or custom algorithms, are often employed to create and refine such lattices ensuring conformation to geometric constraints and suitability for additive manufacturing processes. As these stochastic lattices can mimic the heterogeneity and anisotropy of natural bone, they are being utilized more and more in bioimplant designs. This makes them perfect for orthopedic implants and tissue engineering applications [20].

4.3.2 From CAD Model to Voronoi Lattice Mesh using Ntop

The creation of these scaffolds required advanced computational tools due to the limitations of traditional CAD software. Instead, nTop Platform was utilized for its capability to design complex geometries, including porous lattices, with high precision. This software allows engineers to control critical design parameters, such as pore size, shape, and arrangement, which directly influence the scaffold's mechanical properties and biological interactions. NTop Platform's computational efficiency and ability to handle intricate lattice structures make it an ideal tool for scaffold design and optimization. To get from the CAD Model to the Simulation ready STL file we followed the steps below:

1. <u>Importing the CAD Model and Converting to an Implicit Body:</u>

The process of creating the Voronoi lattice scaffold in NTop began with importing the 3D CAD model of the bone scaffold we created earlier. Since CAD models are typically defined by boundary representations or solid bodies, they need to be converted into implicit bodies within NTop. NTop operates primarily with implicit modeling, which differs from traditional CAD modeling. Instead of defining geometry through explicit surfaces and edges, implicit bodies use mathematical field equations to define shapes. This method offers several advantages such

as greater computational efficiency and stability, especially when conducting complex transformations like latticing. Once converted, the implicit representation of the scaffold became the foundation for creating a volume lattice that would be used in the next steps.



Figure 4.12 CAD Model to Implicit Body

2. <u>Creating the Triangle Volume Mesh for Voronoi Lattice Generation:</u>

To define the internal lattice structure, a triangle volume mesh was generated from the implicit body. This step was necessary because the Voronoi Volume Lattice command requires a 3D mesh input to distribute Voronoi seed points inside the defined volume.

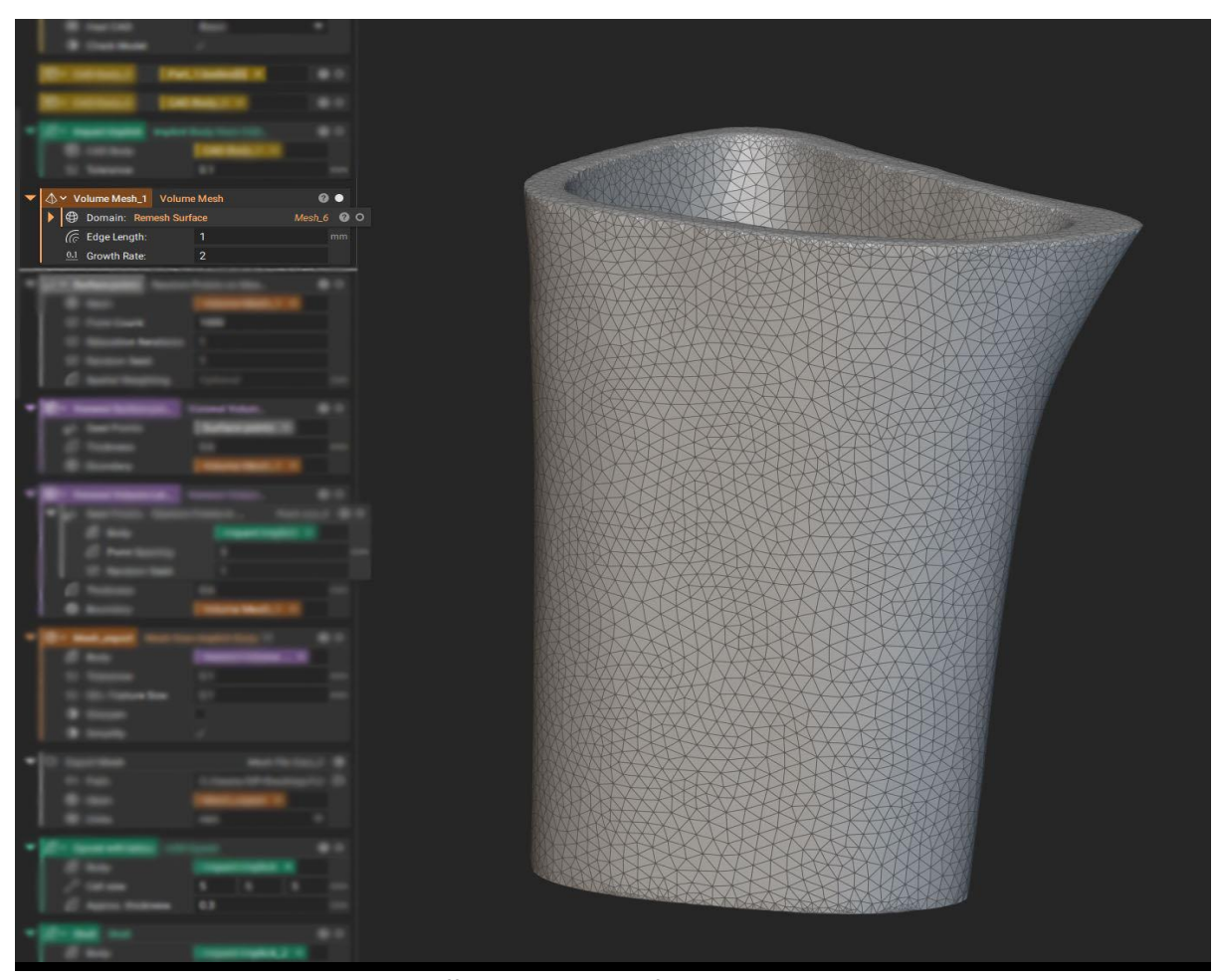


Figure 4.13 Scaffold Volume Mesh for Voronoi Lattice Creation

3. Generating the Voronoi Volume Lattice:

Using the Voronoi Volume Lattice command, we generated the internal lattice structure. The Voronoi algorithm works by placing seed points within the volume and constructing a cell-based network where each cell's edges form the lattice struts. For the parameter values we selected **3mm point spacing and 0.6mm thickness** for the Voronoi struts. In our design of the Voronoi porous scaffold, we chose a point spacing of 3 mm and a strut width of 0.6 mm—not because the printer couldn't handle finer features, but because of the computational limitations of our simulation tools. Modern SLM machines can easily print much smaller details, even below 100µm. However, simulating such fine structures would have required an extremely dense mesh and far more computing power than we had available. A more detailed mesh means significantly longer processing times and a much higher risk of crashes or incomplete results. By choosing these dimensions, we struck a balance: the geometry is still representative of real-world scaffold designs, but the simulations remain manageable and accurate. This approach allowed us to explore mechanical behavior and printability without compromising simulation performance or realism.

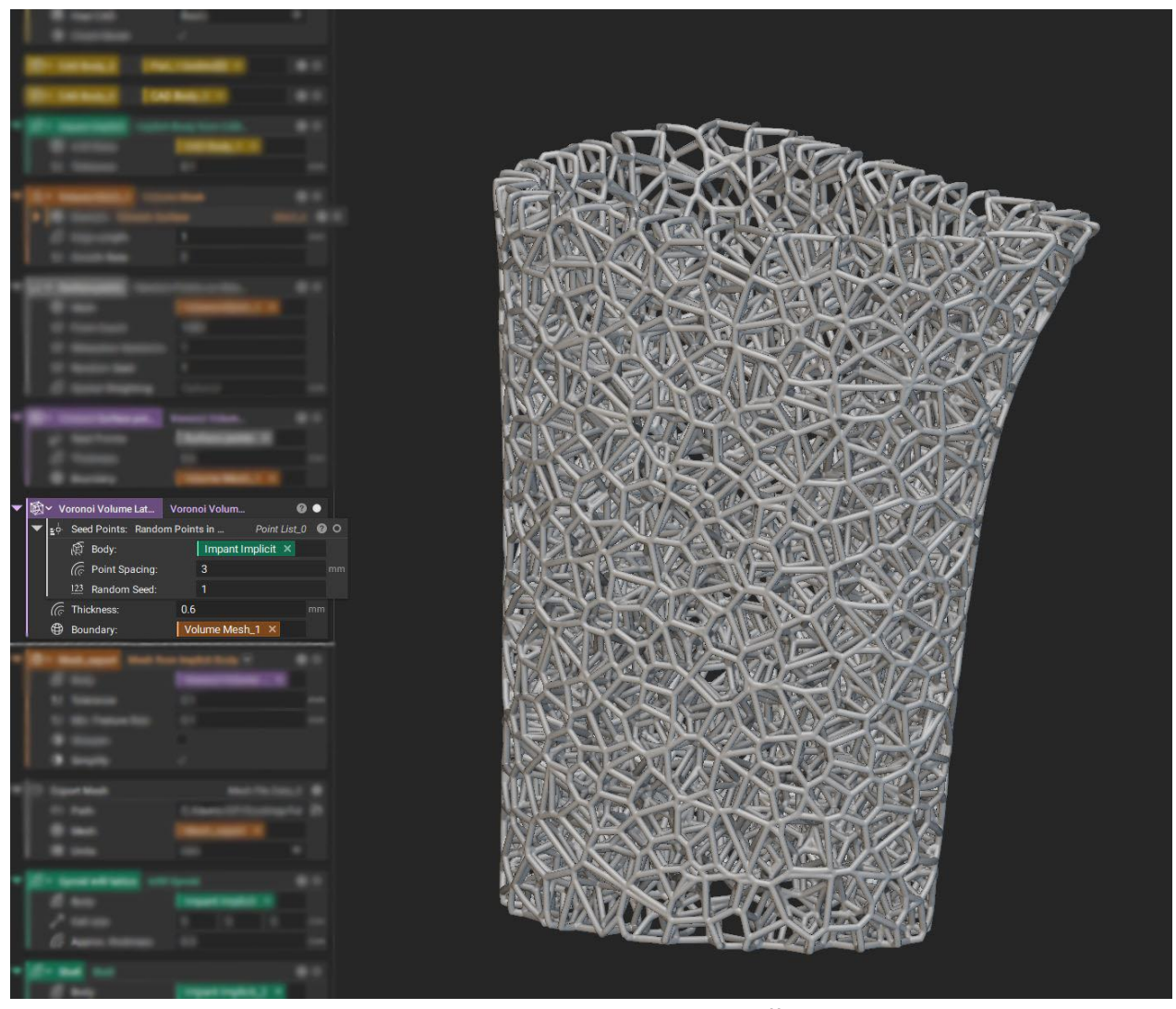


Figure 4.14 Voronoi Volume Lattice Scaffold

4. Constraining the Geometry to the Original Scaffold Boundaries:

After creating the Voronoi lattice, we needed to constrict the generated geometry to the original scaffold's volume. We achieved that by using the Boolean Intersect command, which trimmed down the lattice geometry to the external shape of the original scaffold. This step ensured that the lattice did not extend beyond the intended scaffold region maintaining its original anatomical dimensions, ensuring proper fit and function within the bone defect site.

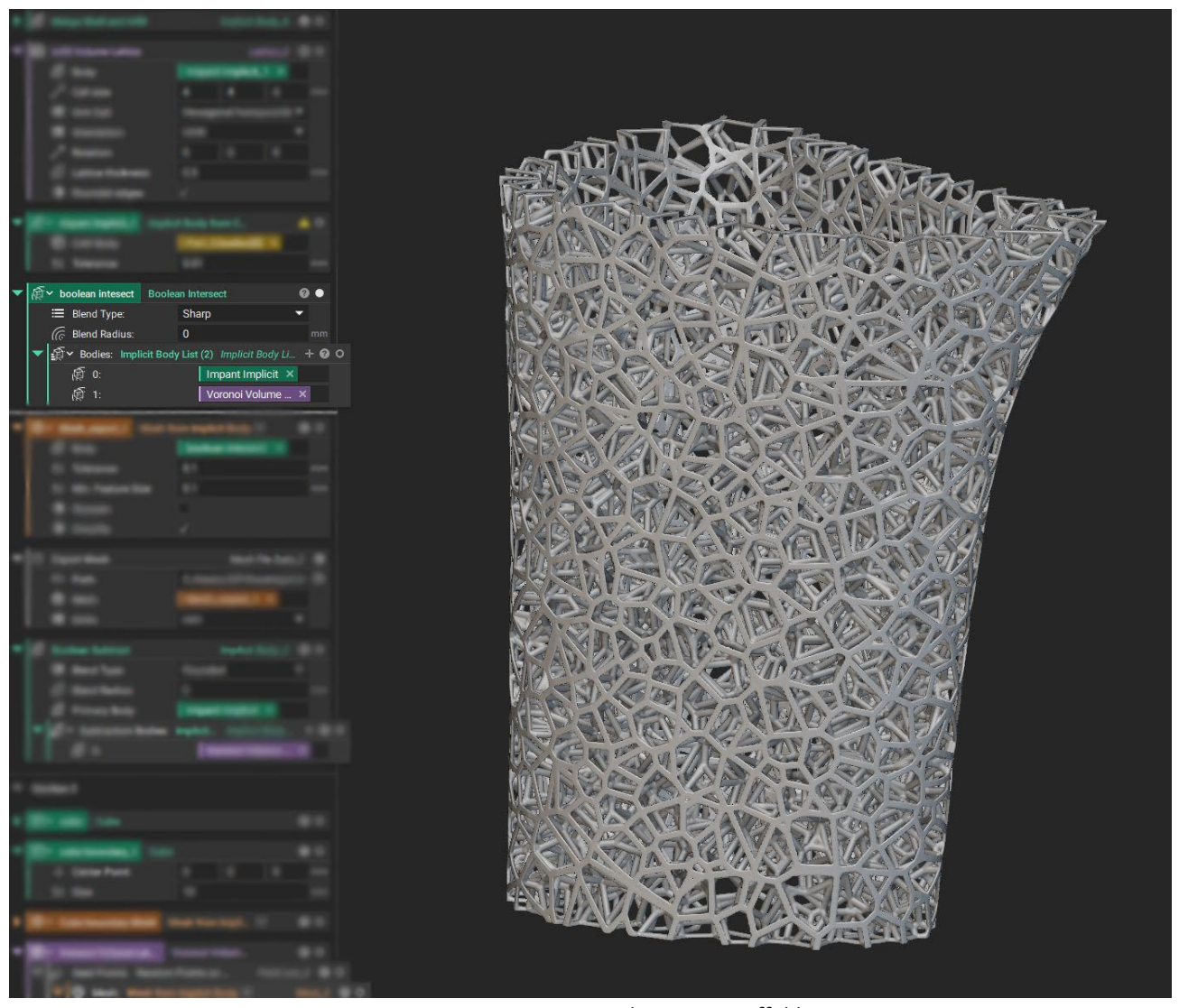


Figure 4.15 Trimmed Voronoi Scaffold

5. <u>Creating and Exporting the Final Detailed Mesh for Simulation:</u>

Once the Voronoi scaffold was finalized, we generated a high-resolution mesh of the lattice structure and exported it as an STL file for use in SLM printing and finite element simulations. The final mesh ensured smooth lattice transitions for better manufacturability, accurate representation of the Voronoi geometry for simulation and optimized meshing density to balance computational efficiency with structural precision.

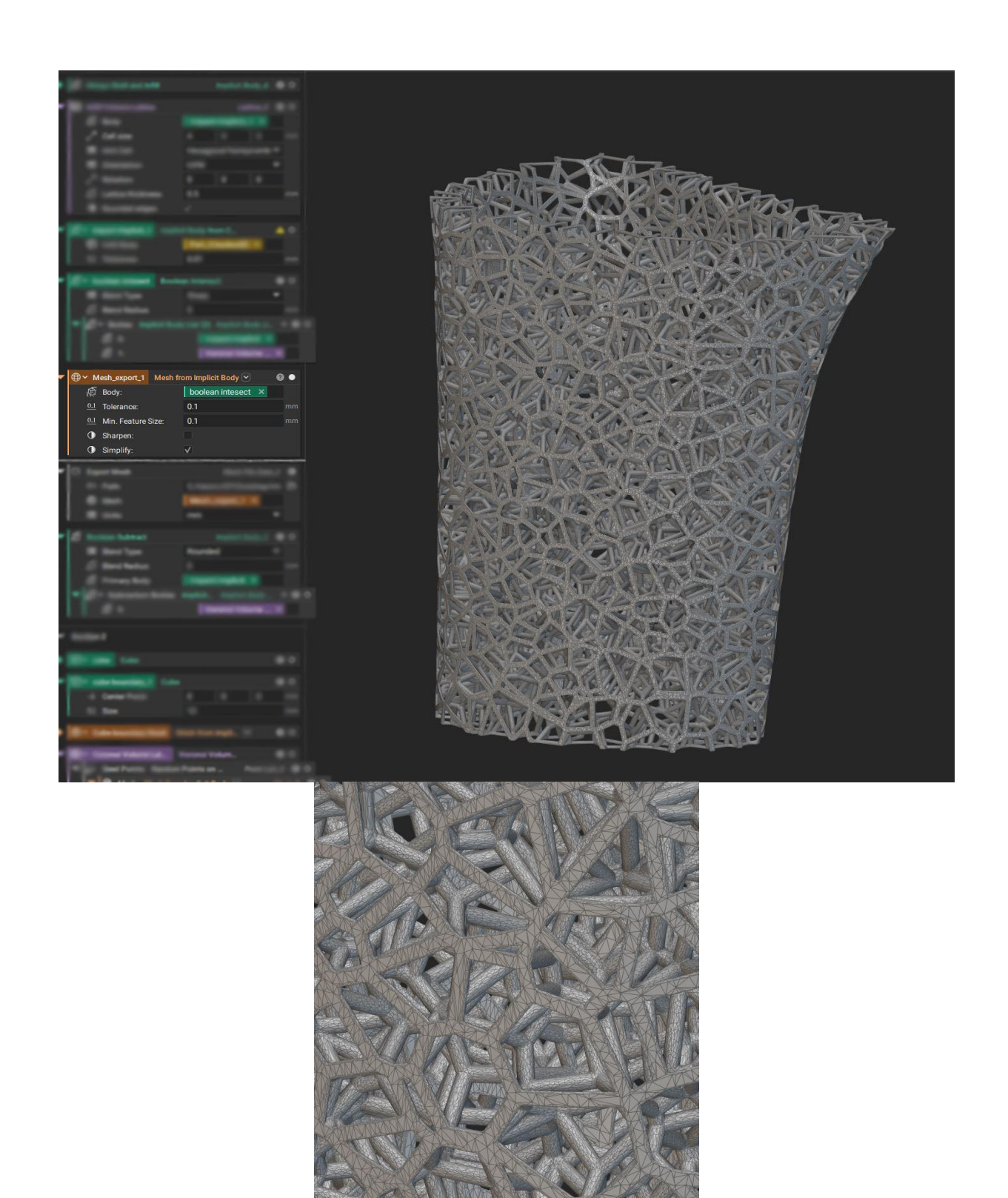


Figure 4.16 Final Mesh for Simulation

To conclude, through NTop's advanced implicit modeling tools, we successfully transformed a solid CAD model into a Voronoi lattice scaffold optimized for SLM printing. By carefully selecting point spacing and strut thickness, applying Boolean operations for geometric constraints, and exporting a detailed STL mesh, we ensured that the scaffold met both biomechanical and manufacturing requirements.

5. Printing Process Simulation

5.1 Ansys Additive

5.1.1 Introduction to Ansys Additive

The ANSYS Additive Library is a specialized resource within the ANSYS suite of simulation tools designed to assist in additive manufacturing (AM) processes. It provides simulation capabilities for additive manufacturing, enabling engineers to optimize the design, process, and performance of 3D-printed components [24].

The Additive application simulates the layer-by-layer construction of metal parts using Laser Powder Bed Fusion (LPBF), a method where a laser melts or fuses metal powder to create a solid structure and as we already discussed, is very suited for the manufacturing of bone imitating implantable scaffolds. During this process, the area under the laser is exposed to intense localized heat that rapidly cools, leading to thermal distortion. To predict this distortion, the simulation applies a layer-by-layer inherent strain accumulation model. This simulation provides valuable insights into the complex thermal and mechanical behaviors involved in the LPBF process.

Simulations can be utilized at various stages of the design and manufacturing process, depending on specific objectives. By addressing issues such as residual stress, distortion, and build failures, these simulations offer practical solutions to enhance manufacturing outcomes. For instance, they enable designers to improve product designs by predicting and visualizing areas of distortion caused by rapid heating and cooling. This allows for quick adjustments to ensure parts remain within tolerances, eliminating the need for multiple trial builds which are costly and time consuming, especially when referring to patient specific implantable scaffolds. Furthermore, simulations can predict part distortion during the printing process and use this information to create a distortion-compensated geometry. This adjusted geometry ensures that the final manufactured part aligns with the original design intent. All of the above make Ansys additive a useful tool to make production more efficient and minimize the challenges associated with metal additive manufacturing.

5.1.2 Theoretical Overview and Strain Simulation Types

In additive manufacturing, components are created by sintering or fusing material in a sequential track-by-track manner, forming thin horizontal layers that are stacked vertically to build the final part geometry.

Ansys Additive utilizes two solving routines to estimate the resulting printed geometry, the **Mechanics solver** and the **Thermal solver**.

The Mechanics Solver simulates material consolidation and the resulting distortions and residual stresses in Laser Powder Bed Fusion (LPBF) additive manufacturing. It predicts deformation, residual stress accumulation, and post-build distortions by modeling the layer-by-layer thermal and mechanical effects of the process. To optimize computational efficiency while maintaining accuracy, the solver simplifies the micron-level details by assuming that entire powder layers melt simultaneously rather than track by track. This approximation reduces computational costs while still capturing the shrinkage effects that cause internal stresses. The solver also enables key post-processing analyses, such as warping prediction, support structure optimization, and distortion compensation, allowing engineers to refine designs and improve print accuracy. Additionally, it simulates the release of internal stresses when the part is removed from the baseplate, helping to anticipate final shape changes.

The Mechanics Solver offers three strain modeling approaches to simulate how thermal shrinkage affects the printed part. Assumed strain applies isotropic inherent strain to each layer, using pre-calibrated strain values from experimental data. Scan-pattern-based anisotropic strain incorporates the scan vectors of the laser path, recognizing that shrinkage strain is higher in the laser's scanning direction compared to perpendicular directions. This method assigns different strain values along the parallel, perpendicular, and Z-directions based on an anisotropic strain coefficient. Thermal strain, the most detailed approach, derives strain values directly from the Ansys Additive Thermal Solver by tracking how thermal cycling influences strain accumulation. This method employs a thermal ratcheting algorithm, which assigns a

base strain to each location in the part as it solidifies. Every time a specific area is reheated above a defined temperature threshold (typically 40% of its melting temperature), additional strain accumulates. If an area fully re-melts, the strain resets to the base value. The more times a region is exposed to heat without melting, the more strain it accumulates, affecting residual stress distribution.

The Thermal Solver models heat transfer and temperature evolution throughout the LPBF process, predicting phase changes, cooling rates, and localized thermal effects. It follows the laser scan path in small time steps, simulating heat conduction through the solidifying part. The solver uses a multi-scale approach, employing fine-scale finite element modeling (FEM) for individual scan tracks and coarsening the results for the entire part to balance computational efficiency and accuracy. It tracks material state changes, estimating melt pool formation and detecting porosity caused by lack of fusion. The solver also applies predefined temperature-dependent material properties, including thermal conductivity, density, and absorptivity, which have been calibrated against experimental data. The thermal simulation results are then passed to the Mechanics Solver to refine stress and distortion predictions, ensuring a highly accurate representation of the additive manufacturing process.

All simulations were conducted using **the Thermal Solver** and the **thermal strain** model approach to ensure greater accuracy. The intricate design of the Voronoi bone scaffold required high precision, even at the cost of increased computational resources and simulation time.

5.2 Printing Process Simulation and Result Options

5.2.1 Simulation Geometry and Voxelization

The initial step in setting up a printing simulation involves selecting and importing the part along with any necessary supports. However, in this case, the Voronoi-structured bone scaffold cannot include supports due to its intricate design, as their removal during post-processing would be impossible.

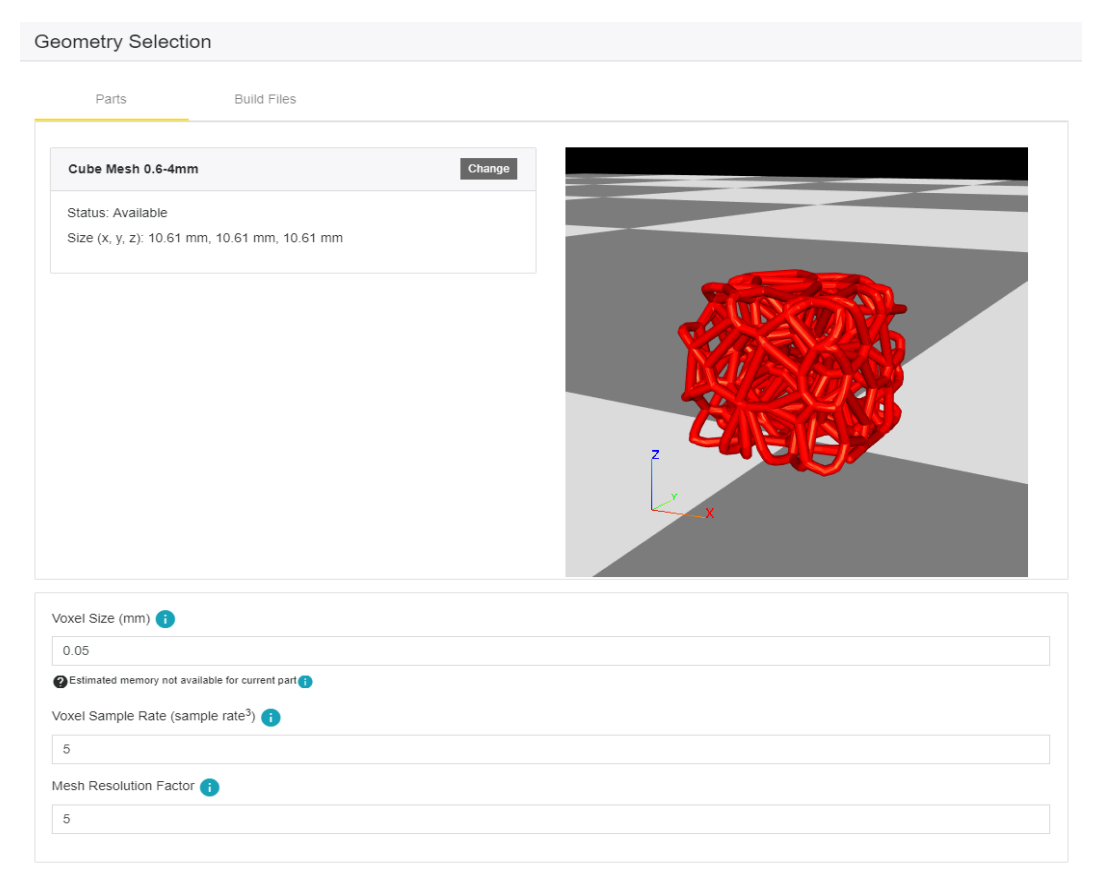


Figure 5.1 Geometry and Voxel Size Selection Window in Ansys Additive

Once added, a preview of the part is displayed, along with key dimensional information in the X, Y, and Z directions and we are prompted to select the appropriate voxel size for our simulation. The voxelization process converts the geometry into a mesh of hexahedral (cubic) elements called voxels, which define the computational domain for simulation. Voxel Size determines the resolution of the voxelized geometry and influences both simulation accuracy and memory requirements. The Minimum Voxel Size is automatically calculated to ensure that the simulation runs without exceeding the machines RAM memory limits. Voxel size significantly impacts computation time, as reducing the voxel size increases the number of elements exponentially with a fourth-power relationship between voxel size and computation time. The Voxel Sample Rate controls how many subvoxels are used within each voxel, particularly at edges and curved regions. A higher sample rate improves geometric fidelity but increases voxelization time. The default sample rate is 5, though higher values may be necessary for capturing small supports and fine details. Generally, there should be at least **four voxels** through the thickness of the finest feature of interest

For our simulations we used the smallest voxel size that was able to be rendered at the available 16 GB of RAM memory we had to our disposal, and left the sampling rate at the default value.

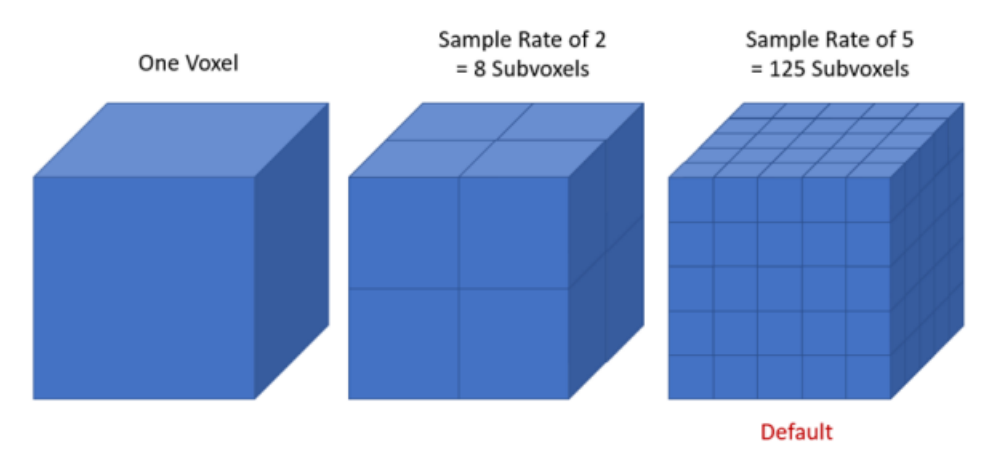


Figure 5.2 Voxel Sample Rate Illustration

5.2.2 Material Selection and Stress mode

In Ansys Additive simulations, materials can be chosen from the predefined library or customized to suit specific needs. Predefined materials include key properties such as elastic modulus, Poisson's ratio, and yield strength at room temperature, which populate the simulation form automatically. For more detailed adjustments, the materials Library allows users to customize materials, enabling modifications like adjusting strain scaling factors or defining fully new temperature-dependent materials. To ensure the material used in the simulation reflected the requirements for medical applications, we customized the default titanium material in Ansys Additive to represent **Ti6Al4V** [21]. As we discussed earlier, this titanium alloy is widely recognized for its biocompatibility, corrosion resistance, and mechanical properties, making it an ideal choice for 3D-printed bone scaffolds. Modifications included tuning its properties, such as elastic modulus and yield strength, to align with the material's established characteristics. By using this alloy in the simulation, we ensured that the results were directly applicable to real-world applications, especially in fabricating load-bearing, biocompatible scaffolds.

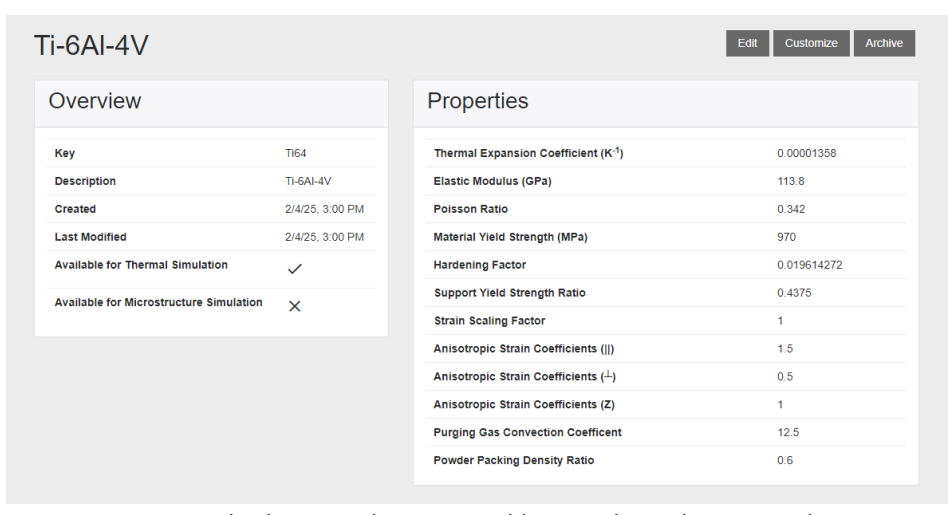


Figure 5.3 Material Selection Tab in Ansys Additive with Ti6Al4V material properties

We also have to specify the stress mode for material behavior, choosing between **linear elastic** and **elastoplastic** (J2-plasticity) models.

The **linear elastic stress mode** assumes that material stress remains proportional to strain, even beyond the yield point, and is computationally less demanding, making it suitable for simulations focused on trends, such as on-plate distortions. While this mode overestimates stress values in the plastic range, it provides accurate predictions of distortion trends and is ideal for cases where heat treatment will later relieve residual stresses. On the other hand, the **J2-plasticity model** is more accurate for ductile materials, capturing both elastic and plastic deformation with strain-hardening behavior. However, it requires significantly longer runtimes and is most useful for precise simulations of aftercutoff distortions and residual stresses.

For our simulations, we opted for the **linear elastic stress mode** to prioritize efficiency. The goal of the simulation was to analyze distortion trends rather than precisely calculate stresses, and the elastoplastic model's extended runtime was unnecessary for our purpose. This approach allowed us to efficiently evaluate the distortion of our Voronoi-structured bone scaffolds while still achieving relevant insights for optimizing the design.

5.2.3 Machine Parameters

In every method of additive manufacturing machine parameters play a critical role in determining the accuracy, mechanical properties, and overall success of a printed part. By optimizing the following machine parameters within Ansys Additive, we can try to enhance part quality and reduce defects, ultimately improving the efficiency and reliability of SLM production:

- Laser Power (W) is the power output of the machines laser module. It is set between 50 and 700 Watts with the default being 195W.
- **Scan Speed (mm/sec)** is the speed that the laser spot moves across the powder bet to melt the material. Typical values are between 350 and 2500 mm/sec with the default being set to 1000 mm/sec.
- Laser Beam Diameter (μ m) is a parameter typically provided by the machine manufacturer. Often referred to as the laser spot diameter, it ranges between 20 and 140 μ m, with a default setting of 100 μ m.
- Starting Layer Angle (°) refers to the orientation of the of fill rasters on the first layer of the part measured from the X axis, most commonly set at 57 degrees.
- Layer Rotation Angle (°) is the angle at which the major scan vector orientation changes from layer to layer and it is commonly set to 67 degrees.

- Layer Thickness (μm) refers to the thickness of the powder layer coating that is applied with every pass of the recoater blade. Typically, between 10 and 100 microns with the default value being set at 50 microns.
- Hatch Spacing (μm) is the distance between neighboring scan vectors as the laser moves in a raster pattern. It is designed to allow slight overlap between scan tracks, enabling partial re-melting of material to ensure complete solidification. The value typically ranges from 10 to 1000 microns, with a default of 100 microns.
- Slicing Stripe Width (mm). When using the stripe pattern scan strategy, the geometry is divided into smaller sections known as stripes, which are scanned sequentially to prevent excessively long continuous scan vectors. The Slicing Stripe Width is typically set to 10 mm to balance efficiency and accuracy. Increasing this width beyond the default significantly raises memory demands for the thermal simulation. The value is set between 1 and 100 mm, with a default of 10 mm.
- Baseplate Temperature (°C) is the controlled temperature of the baseplate, ranging from 20 to 500 °C and defaulting to 20 °C.

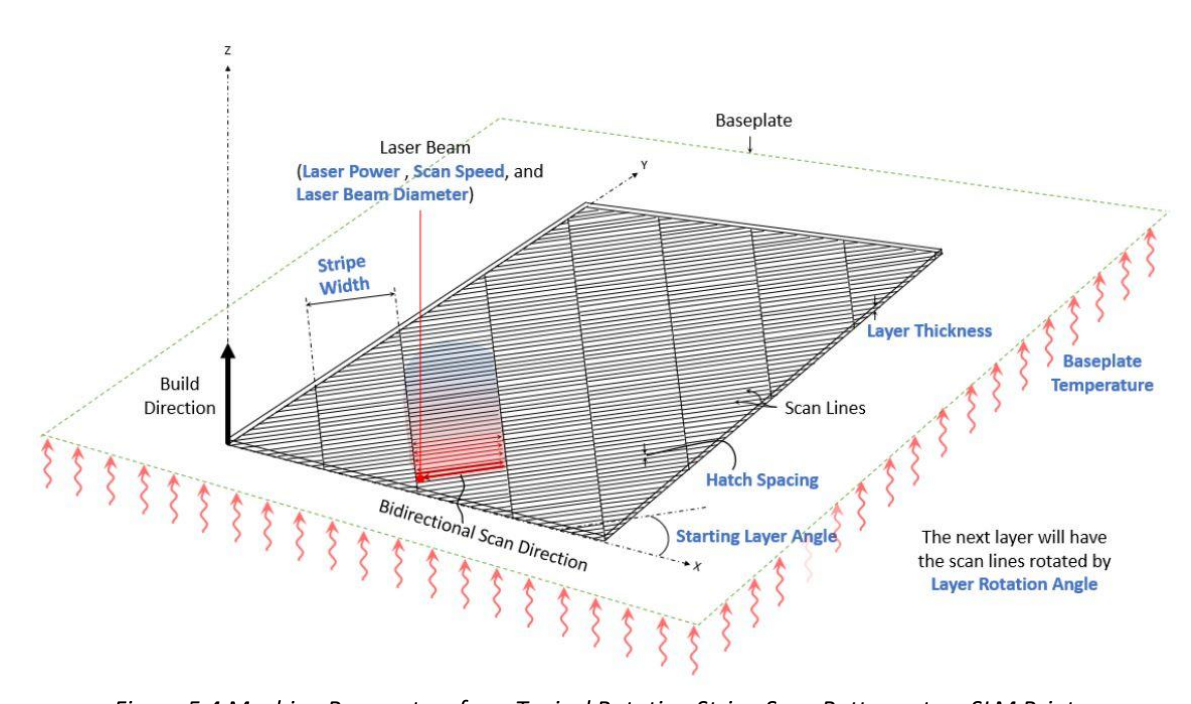


Figure 5.4 Machine Parameters for a Typical Rotating Stripe Scan Pattern at an SLM Printer

In our simulations, we first analyzed the results produces by the stock simulation, where all parameters retained their default value. We then modified specific parameters in subsequent simulations to optimize the manufacturing process and improve the final results.

5.2.4 Simulation Outputs Selection

The Ansys Additive application offers a variety of result options to analyze and evaluate the outcomes of additive manufacturing simulations. Below is an explanation of the available outputs and how they apply to simulations.

1. On-Plate Residual Stress/Distortion: This is the default output option for all simulations, providing a voxelized representation of the part with residual stresses and displacements while the part is still attached to the baseplate. Both the final stress state and the maximum stress experienced during the build are included. For parts without supports, such as our Voronoi-structured bone scaffold, this output is crucial for analyzing distortion trends during the build process.

Distortion Compensation can also be activated to generate a compensated .stl file that adjusts the geometry to account for predicted distortions. This file helps ensure the final manufactured part conforms more closely to the intended design. Multiple compensation scale factors can be tested iteratively to refine accuracy.

- 2. Displacement After Cutoff: This output simulates the deformation of the part after it is removed from the baseplate. In our simulations, the Displacement After Cutoff feature did not function effectively, possibly due to the extreme level of geometric detail in the Voronoi bone scaffold. The high-resolution mesh required for such intricate geometry may have exceeded the solver's capability to simulate stable cutoff behavior accurately. These factors combined likely contributed to the inability of this output option to produce usable results for our scaffold design.
- 3. Layer-by-Layer Stress/Distortion: This output provides detailed results for each voxel layer as the part is built, allowing us to visualize the progressive behavior of the part during the additive process. It is especially useful for identifying potential issues such as blade crashes or high-stress regions that could lead to cracking. Although highly detailed, this option generates large files and significantly increases disk space usage, making it suitable primarily for simulations requiring in-depth analysis of build dynamics.
- **4. Blade Crash Detection:** The Blade Crash Detection feature predicts areas where the recoater blade may collide with distorted regions of the part during the build. By simulating layer displacements and comparing them to the recoater blade's clearance, the tool highlights potential collision areas. For our scaffold, blade crash detection helped ensure that the fine structure would not interfere with the recoater, despite the lack of supports. The blade crash potential is calculated and each voxel is assigned a 0, 1, or 2 as follows:
 - 0 (none predicted)
 - 1 = warning/potential blade crash when positive Z displacement is greater than (Layer Thickness x Threshold).
 - 2 = critical/likely blade crash when positive Z displacement is greater than (Layer Thickness x Threshold + ½ Layer Thickness).

The default Threshold factor is set at 1 and we left the value unchanged.

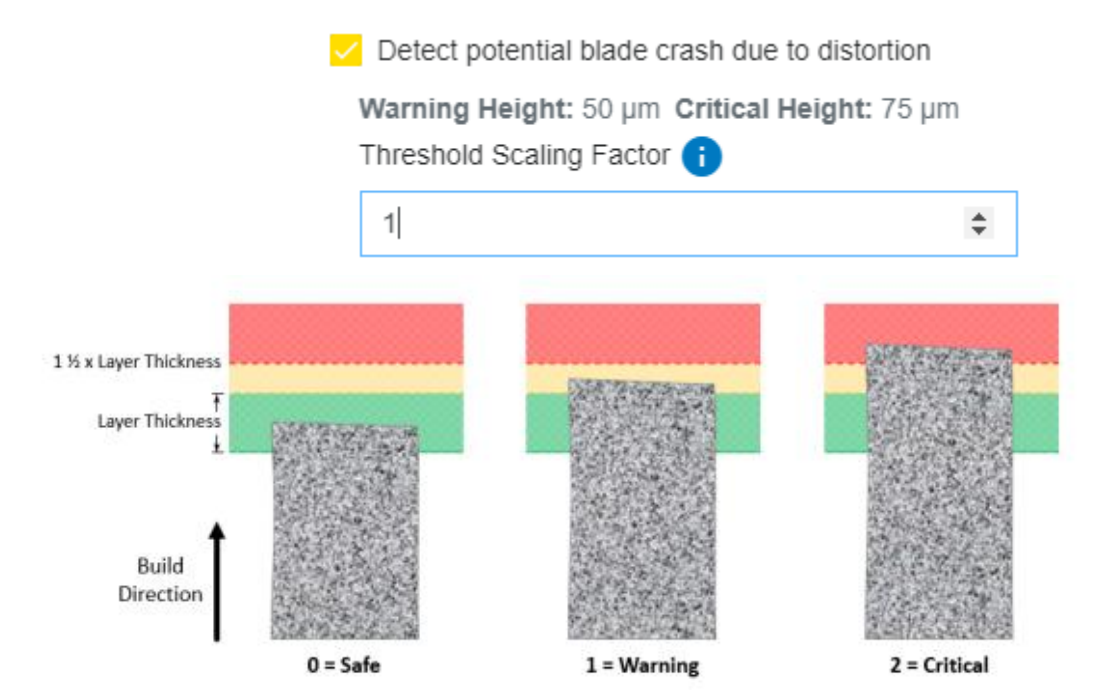


Figure 5.5 Blade Crash Risk Accession by Ansys Additive

5. **High Strain Areas:** The High Strain Areas output identifies regions of the part where strain exceeds the material's limits, indicating areas prone to cracking or failure. This feature is especially useful for detecting weak points in

unsupported designs, like our Voronoi structure, where strain concentrations may occur due to the fine geometry. Critical strain values are highlighted in the output files, providing insights into potential failure regions during or after the build. For our simulations we kept the default values for high strain areas indication [22].

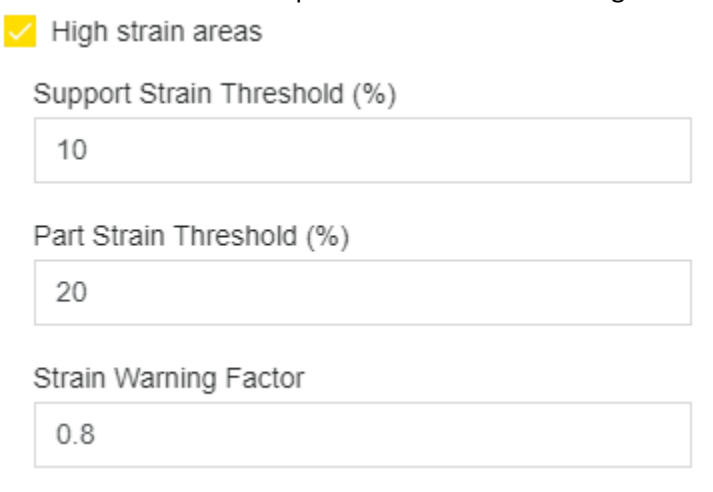


Figure 5.6 Input Variables for High Strain Areas Calculation

5.3 Simulation and Results

In all of the simulations, we analyzed key performance indicators, including maximum displacement (mm), maximum Von Mises stress (MPa), potential blade crash locations, and high strain severity locations. These factors are crucial in assessing the structural integrity, manufacturability, and mechanical performance of the implant.

- **Displacement (mm)**: Indicates the overall deformation of the implant under applied loads. Excessive displacement can lead to implant failure or improper load transfer to surrounding bone tissue.
- End-state von Mises Stress (MPa): Helps evaluate whether the material will yield under stress. Areas exceeding the material's yield strength pose a risk of structural failure.
- **Potential Blade Crash Locations**: In Powder Bed Fusion (PBF) 3D printing, regions with excessive upward displacement may interfere with the recoater blade, potentially damaging the part or halting the print.
- **High Strain Severity Locations**: Identifying areas with significant strain helps predict fatigue failure, particularly for implants subject to cyclic loading.

5.3.1 Full Scaffold Lattice Simulation

Our first simulation involved the entire scaffold lattice, using a voxel size of 0.14 mm. Due to hardware constraints, reducing the voxel size further caused RAM memory shortages, making the simulation unfeasible. The computation time was extensive, taking approximately two days to complete. Despite the coarse voxel size, the results provided insight into overall deformation, stress distribution, and potential weak points in the design.

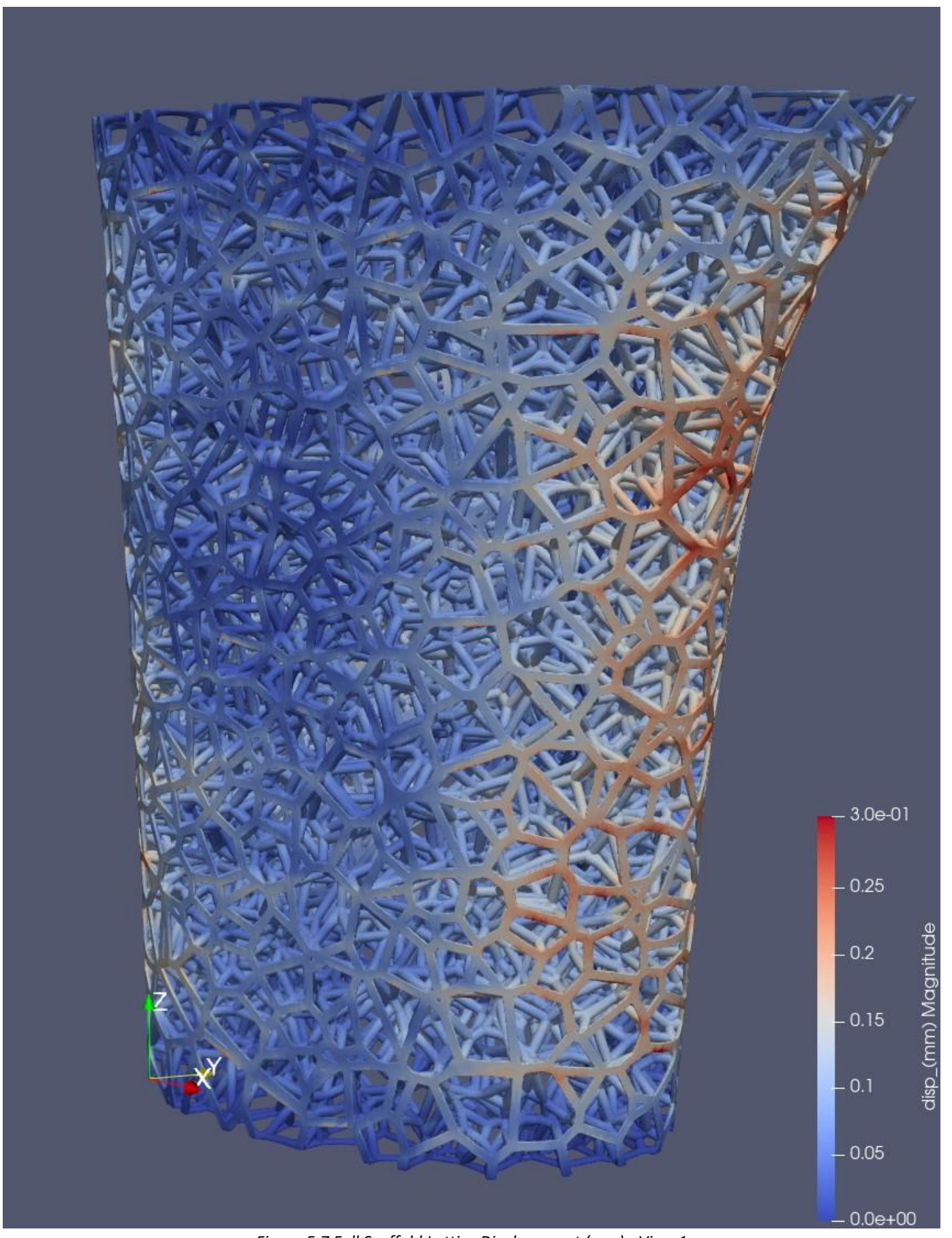


Figure 5.7 Full Scaffold Lattice Displacement (mm) - View 1

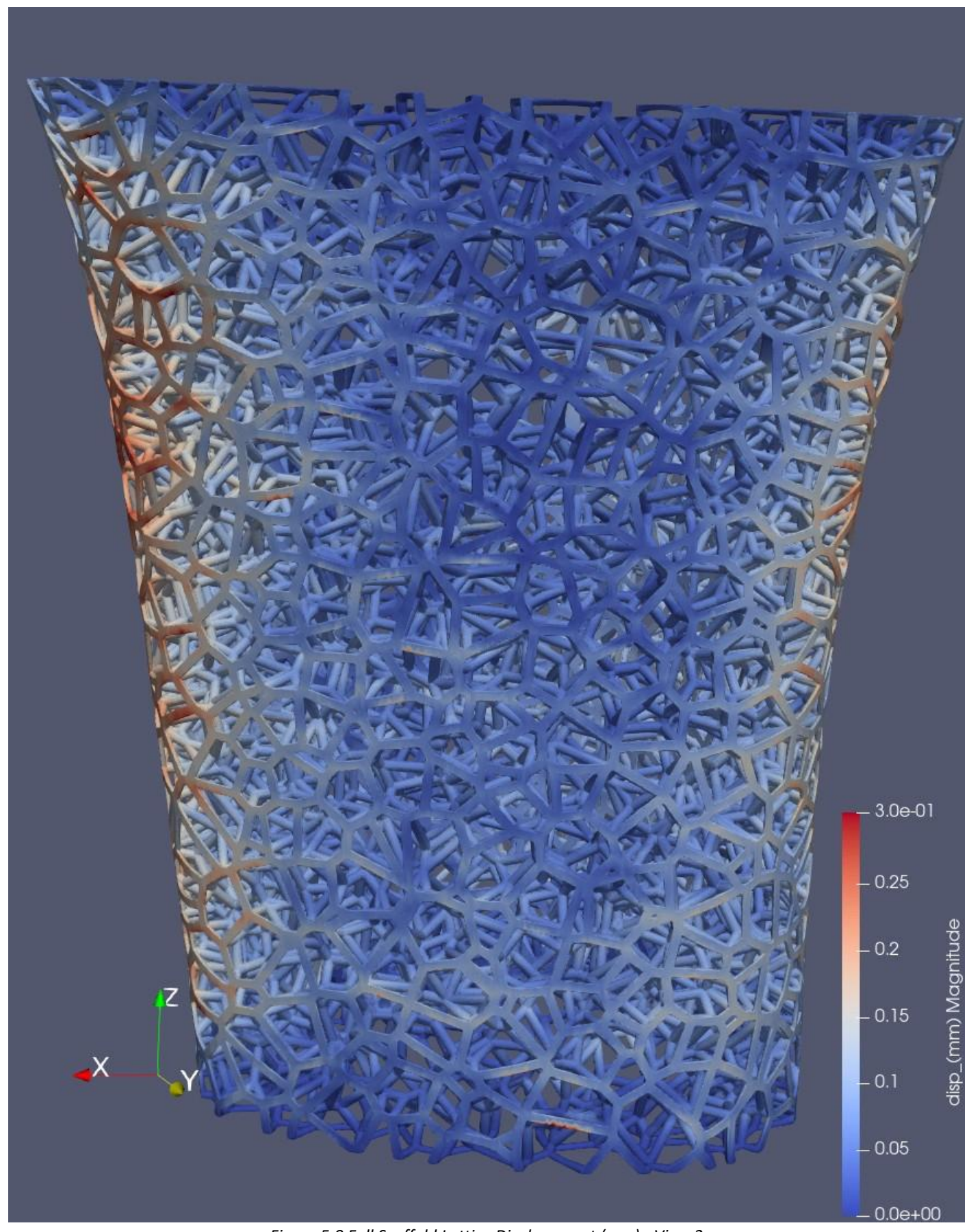


Figure 5.8 Full Scaffold Lattice Displacement (mm) - View 2

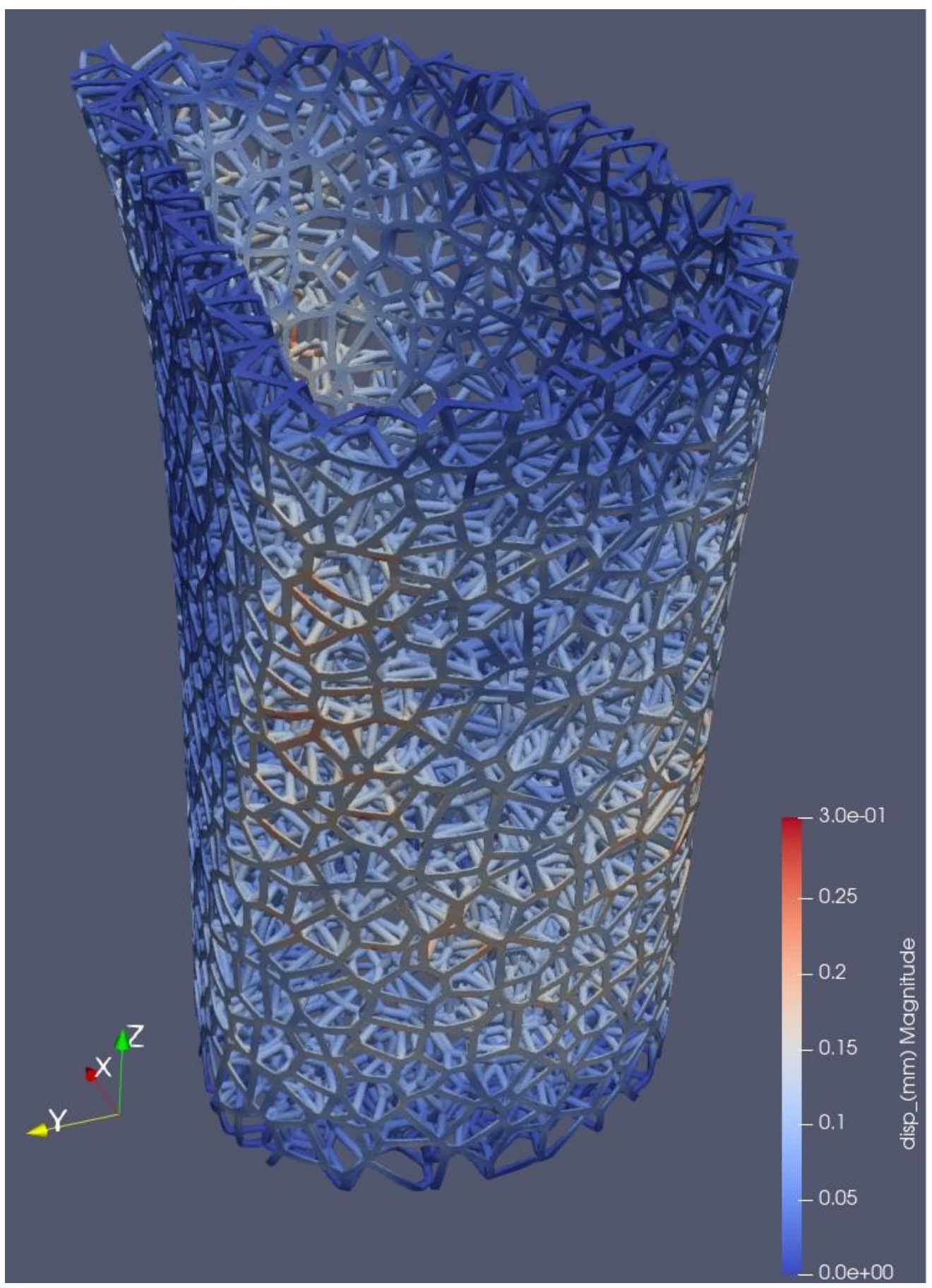


Figure 5.9 Full Scaffold Lattice Displacement (mm) - View 3

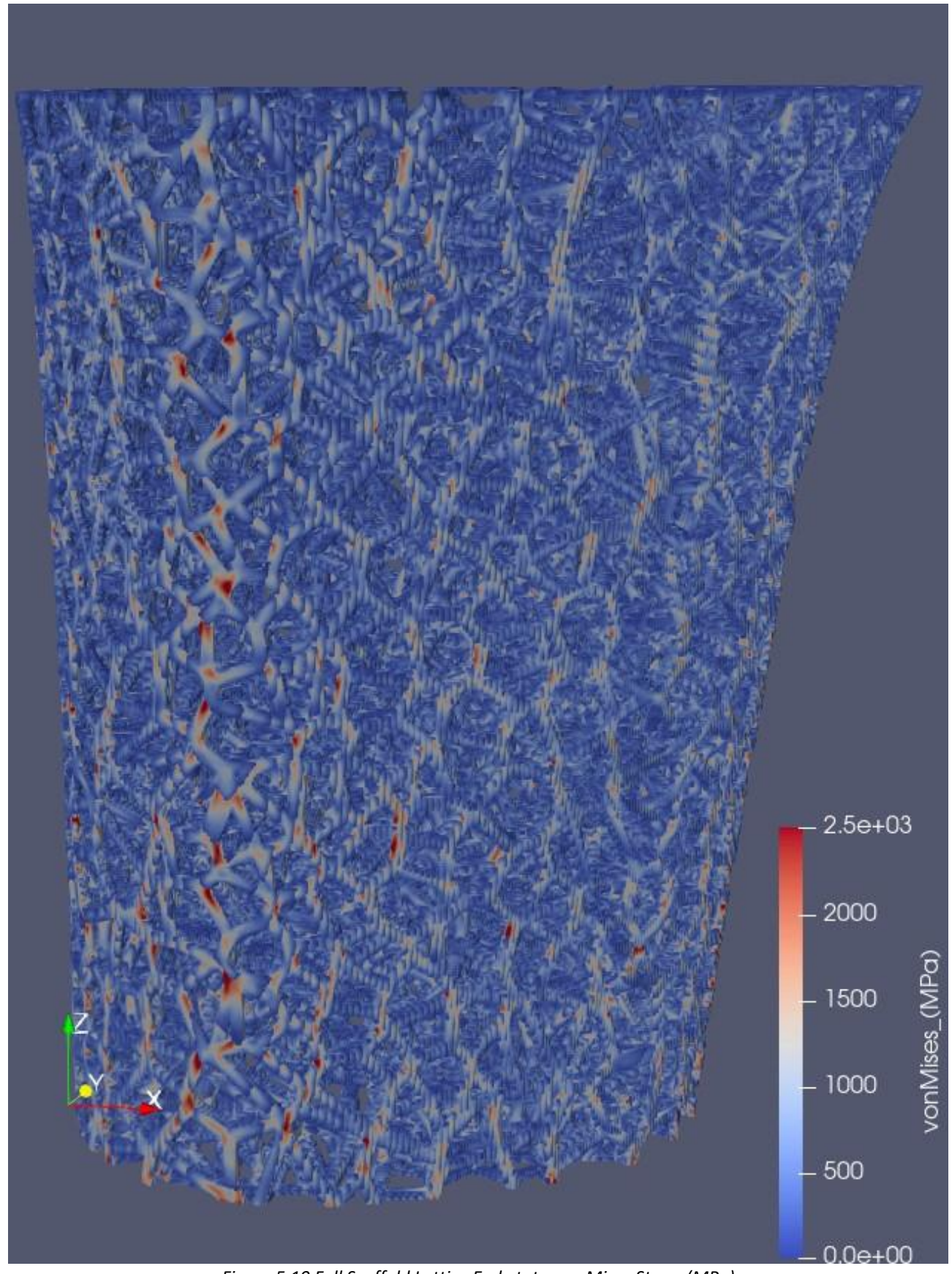


Figure 5.10 Full Scaffold Lattice End-state von Mises Stress (MPa)

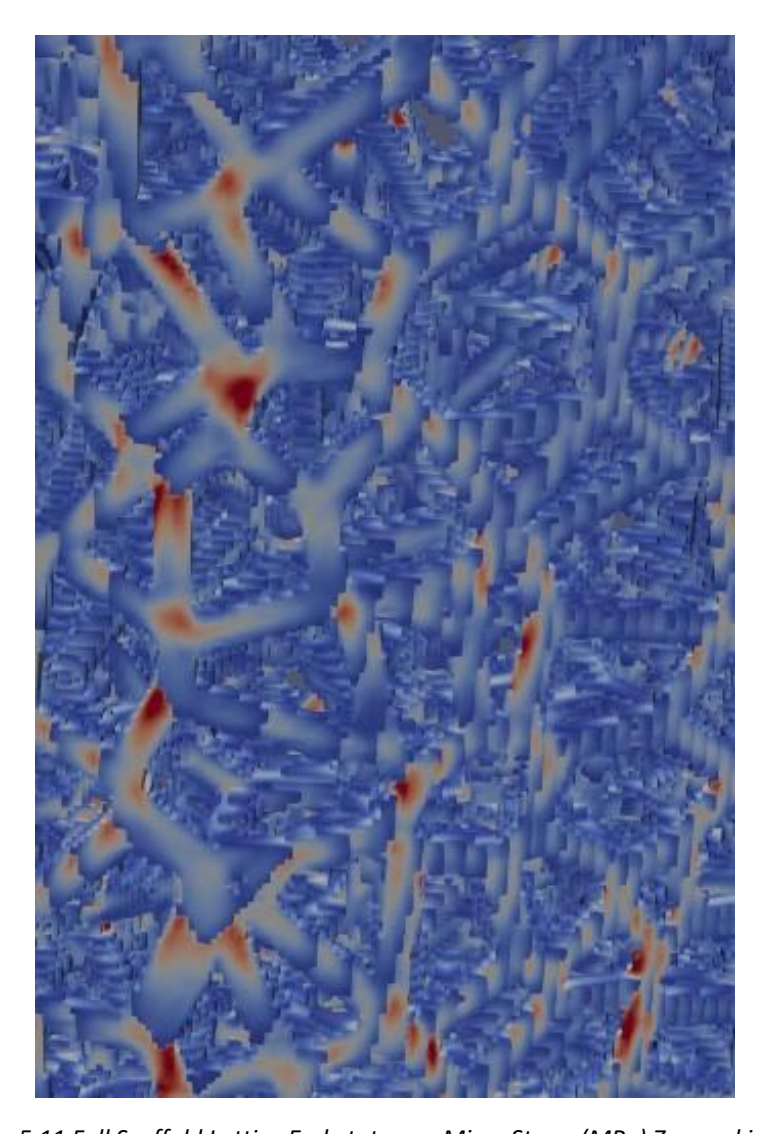


Figure 5.11 Full Scaffold Lattice End-state von Mises Stress (MPa) Zoomed in View

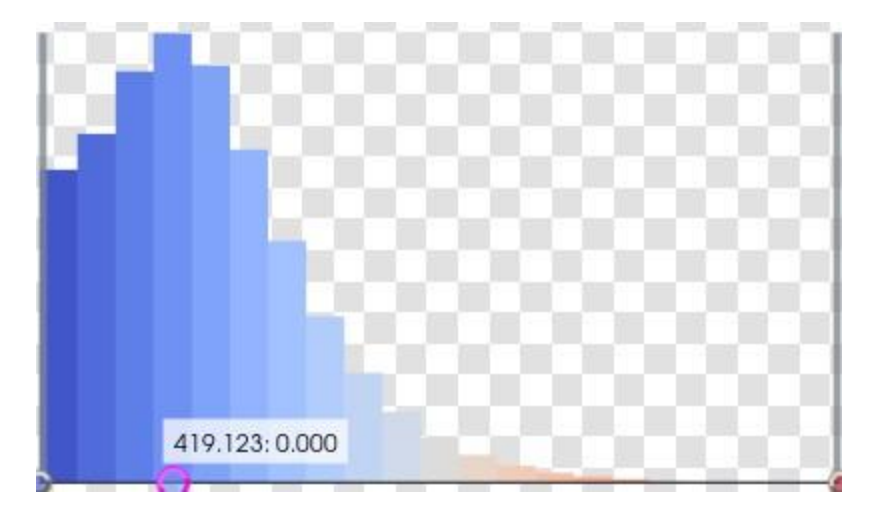


Figure 5.12 Full Scaffold Lattice End-state von Mises Stress (MPa) Histogram

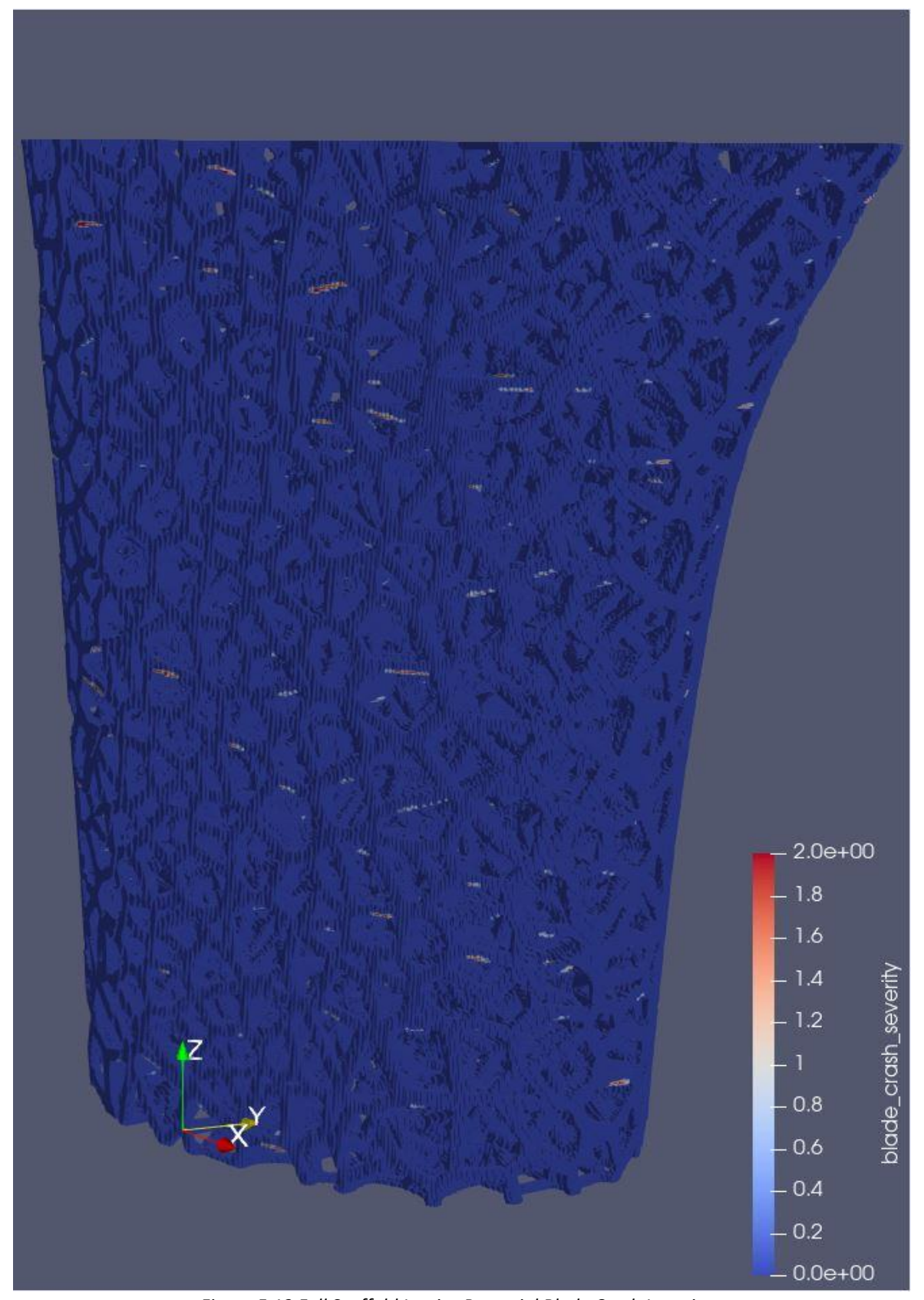


Figure 5.13 Full Scaffold Lattice Potential Blade Crash Locations

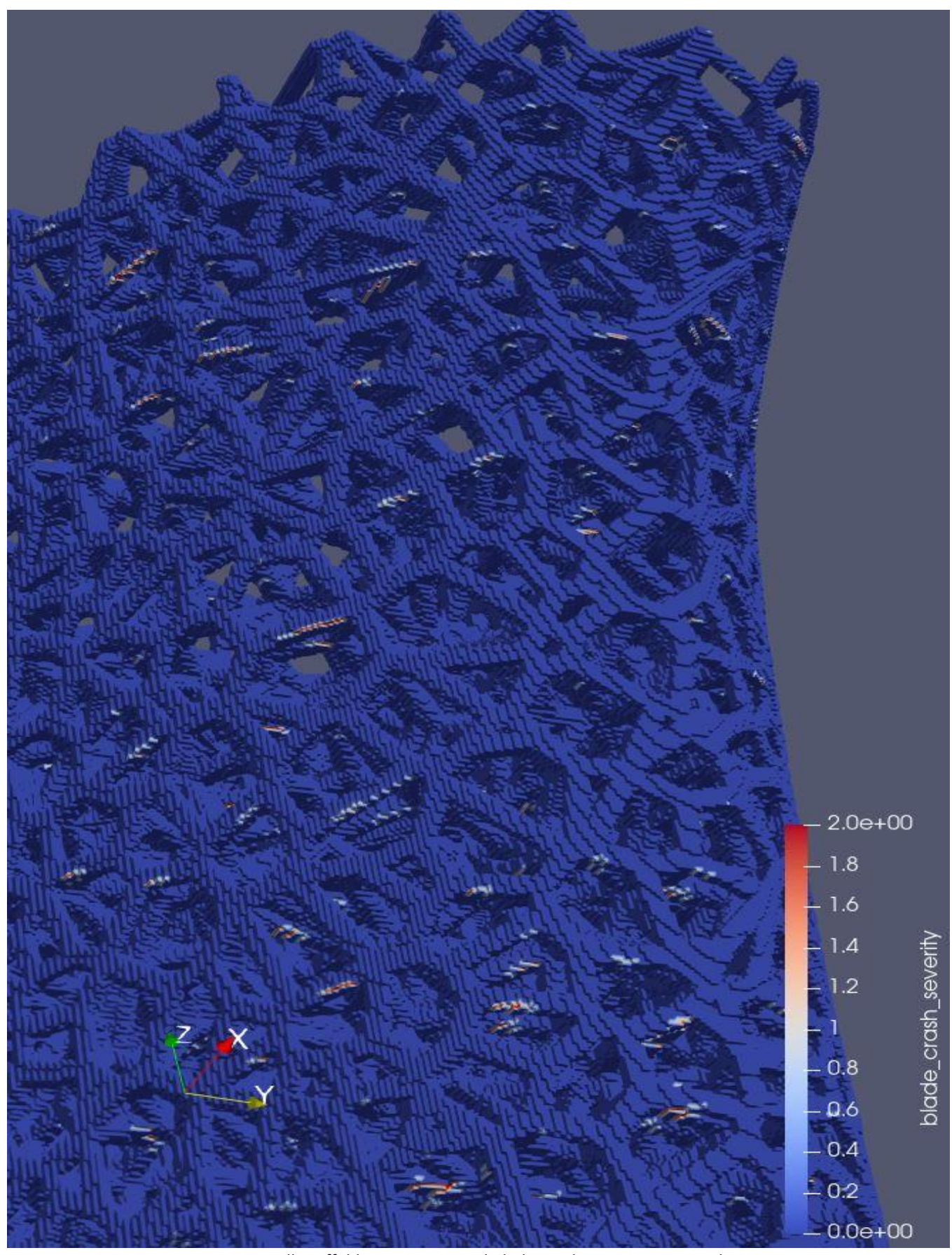


Figure 5.14 Full Scaffold Lattice Potential Blade Crash Locations Zoomed in view

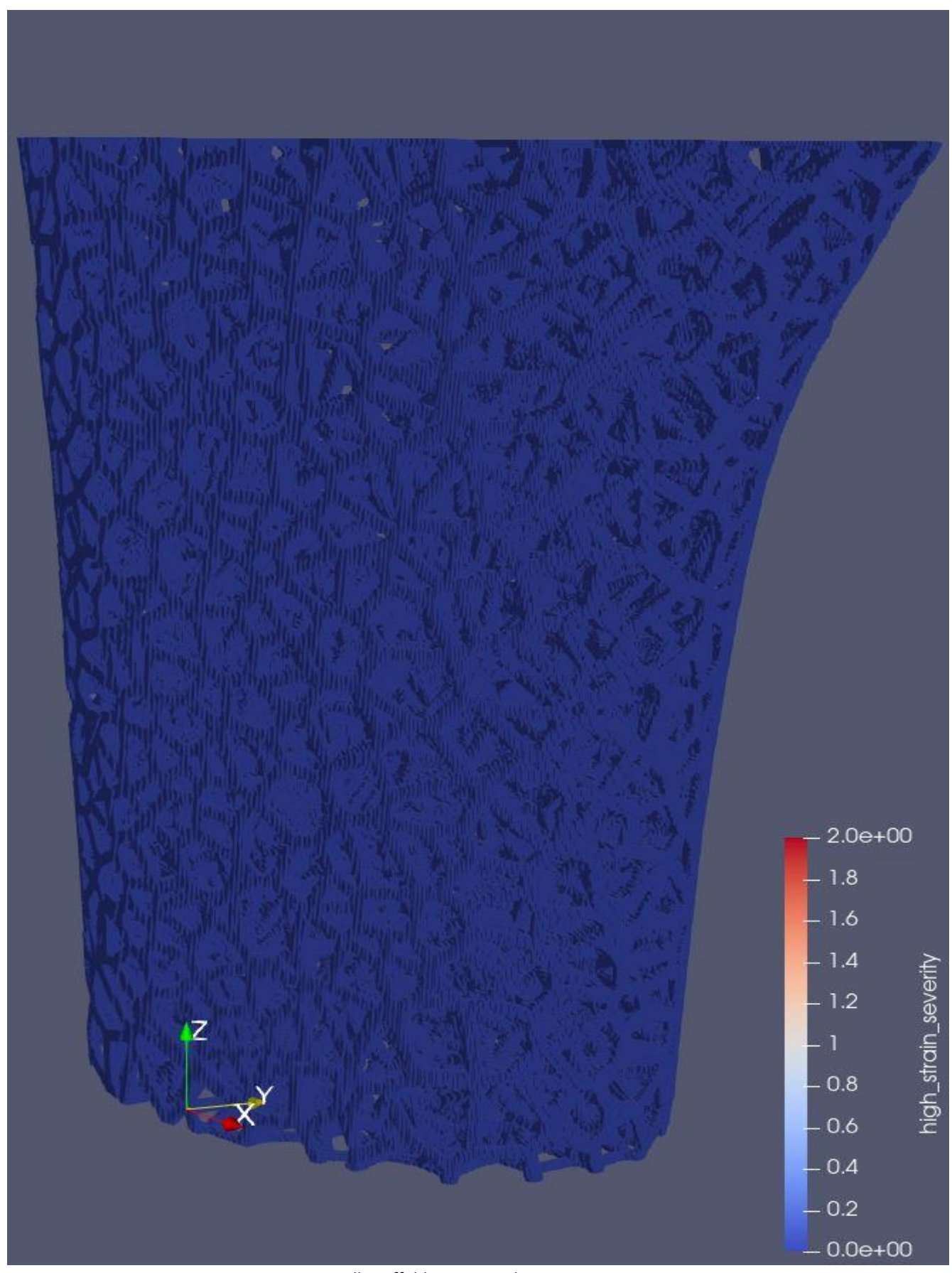


Figure 5.15 Full Scaffold Lattice High Strain Severity Locations

Observations on the Full Lattice Simulation

The full lattice scaffold simulation offers a broad, system-level view of mechanical performance, helping identify general trends in displacement, stress distribution, high-strain zones, and potential blade crash sites. However, due to computational constraints, the simulation had to be run at relatively low mesh resolution, which visibly limits its precision, particularly in identifying localized stress concentrations or subtle geometric features.

Displacement results show a pronounced anisotropy, with deformation being more significant in the upper flared or curved regions of the scaffold. This trend likely arises from both geometry-driven flexibility and reduced structural stiffness in these zones.

The von Mises stress distribution is relatively diffuse in the full scaffold results. While we can detect broader patterns of stress localization near the scaffold's inner and outer surfaces, the coarse mesh blurs the finer-scale gradients. The stress concentration zones are not sharply defined, which limits precise identification of weak points that might initiate mechanical failure. The end-state Von Mises stress histogram shows that the most commonly occurring stress values are centered around 500 MPa, while stress values exceeding 900 MPa appear far less frequently. This trend aligns with findings in the literature on stress accumulation during SLM of titanium alloys, where localized peak stresses may approach the material's yield strength, but the majority of the structure experiences moderate stress levels [26].

High strain severity and potential blade crash visualizations follow a similar trend. The full-scale model allows for identification of global zones with potential risks, such as overhanging or unsupported features near the outer wall and upper flared regions. Still, the results lack the granularity needed to determine exact critical struts or pinpoint fabrication risks—this is where high-resolution analysis becomes necessary.

Overall, the full lattice simulation plays a critical role in understanding macro-level behavior and spatial performance variation across the scaffold. However, its limitations in local detail resolution justify the need for the follow-up 10 mm high-resolution slice analysis.

5.3.2 High-Resolution Simulation of a 10mm Slice

To enhance detail and accuracy in localized regions, we simulated a 10 mm slice of the scaffold using a finer voxel size of 0.07 mm. This allowed for a more precise representation of stress concentration points and deformation patterns while remaining computationally manageable. The finer resolution improved our ability to analyze microstructural responses of the lattice, particularly in regions prone to failure.

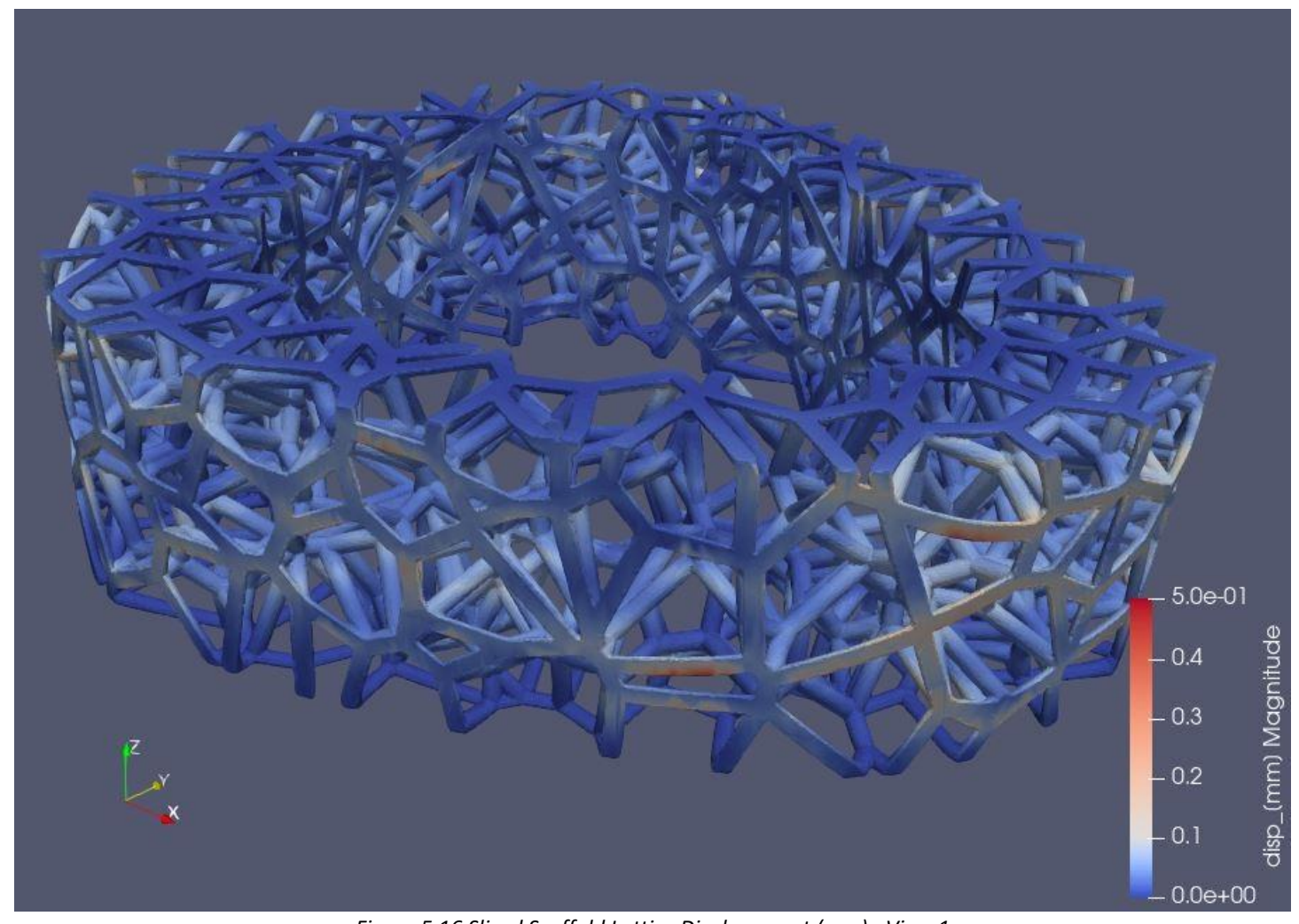


Figure 5.16 Sliced Scaffold Lattice Displacement (mm) - View 1

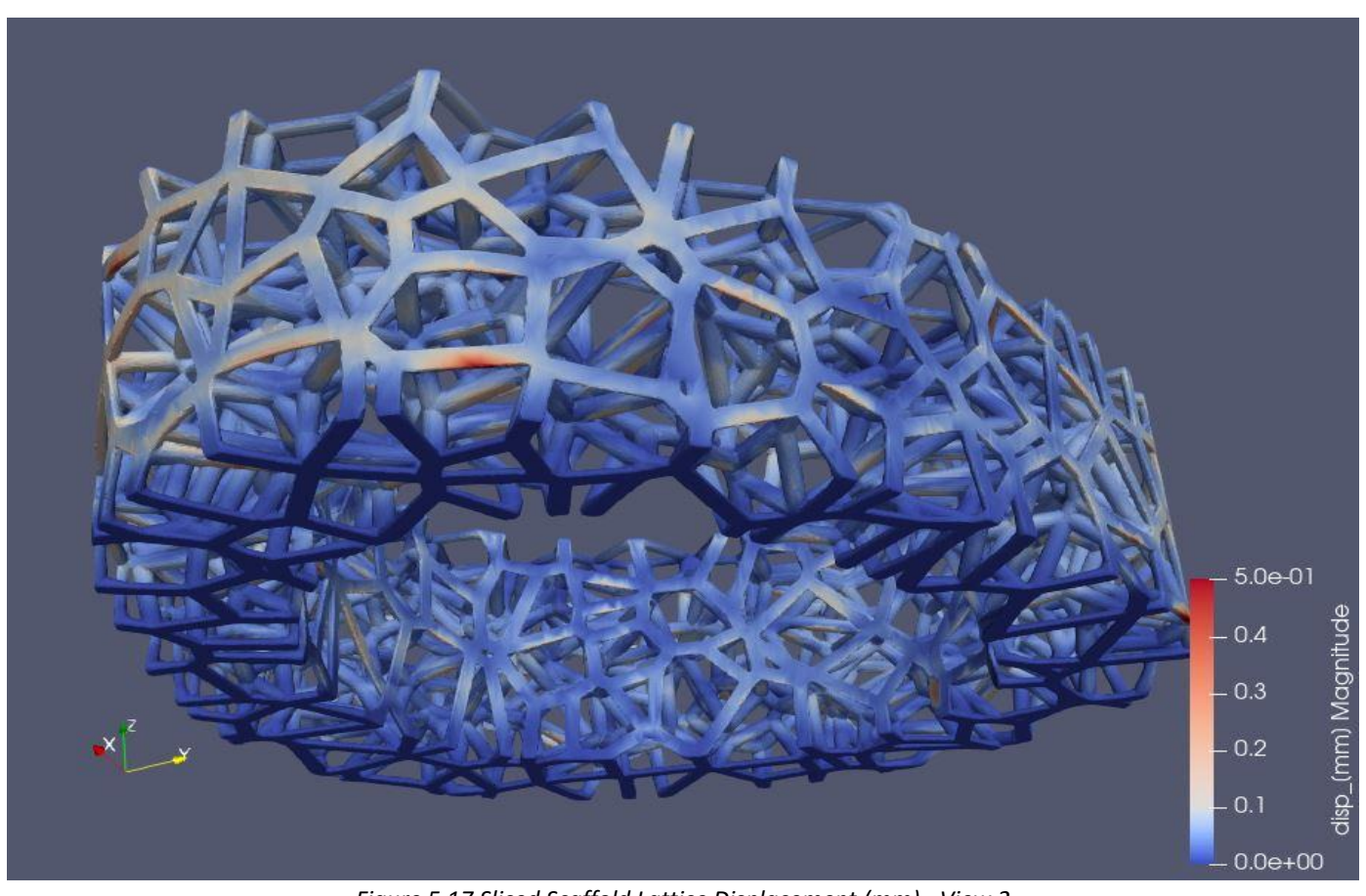


Figure 5.17 Sliced Scaffold Lattice Displacement (mm) - View 2

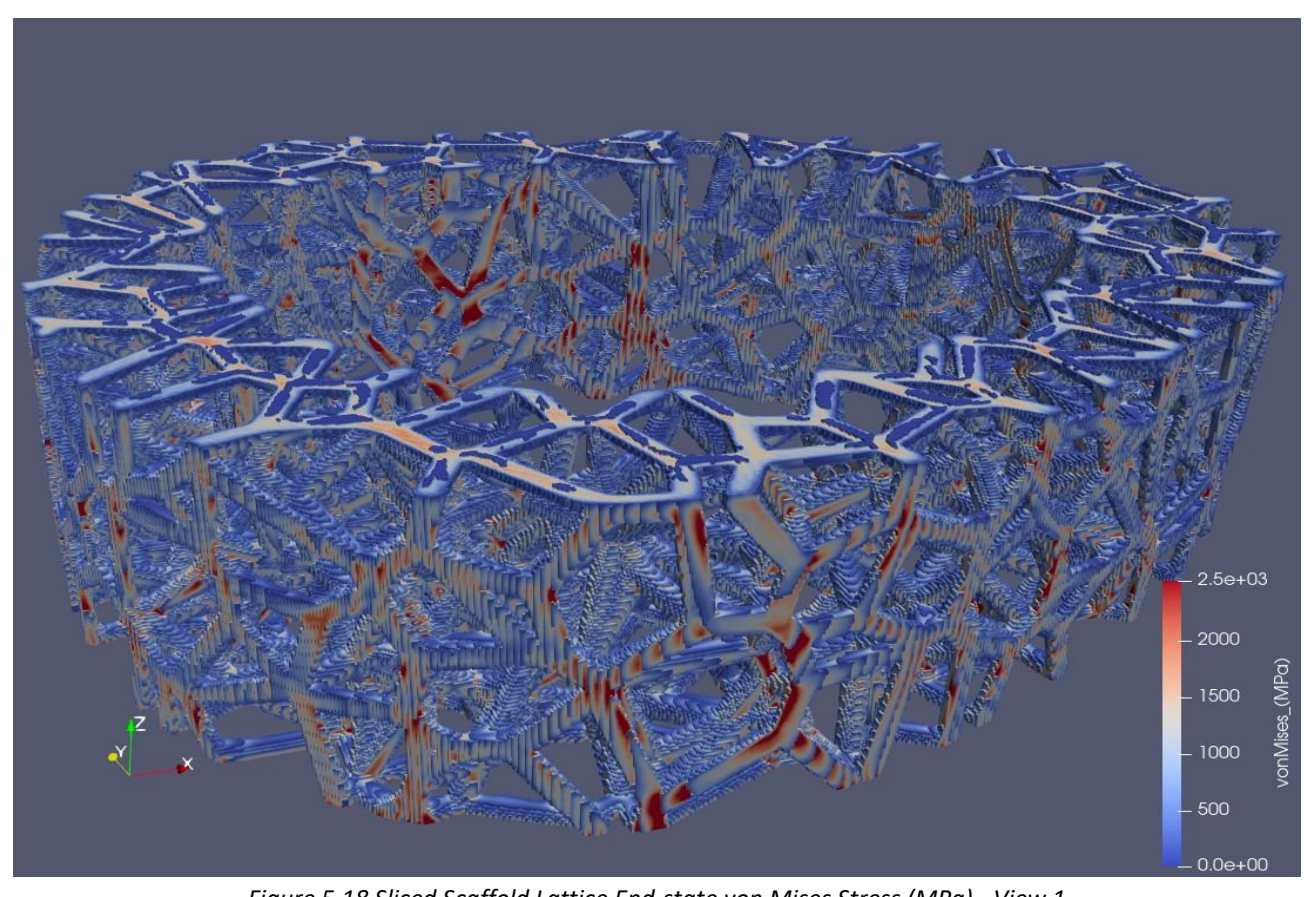
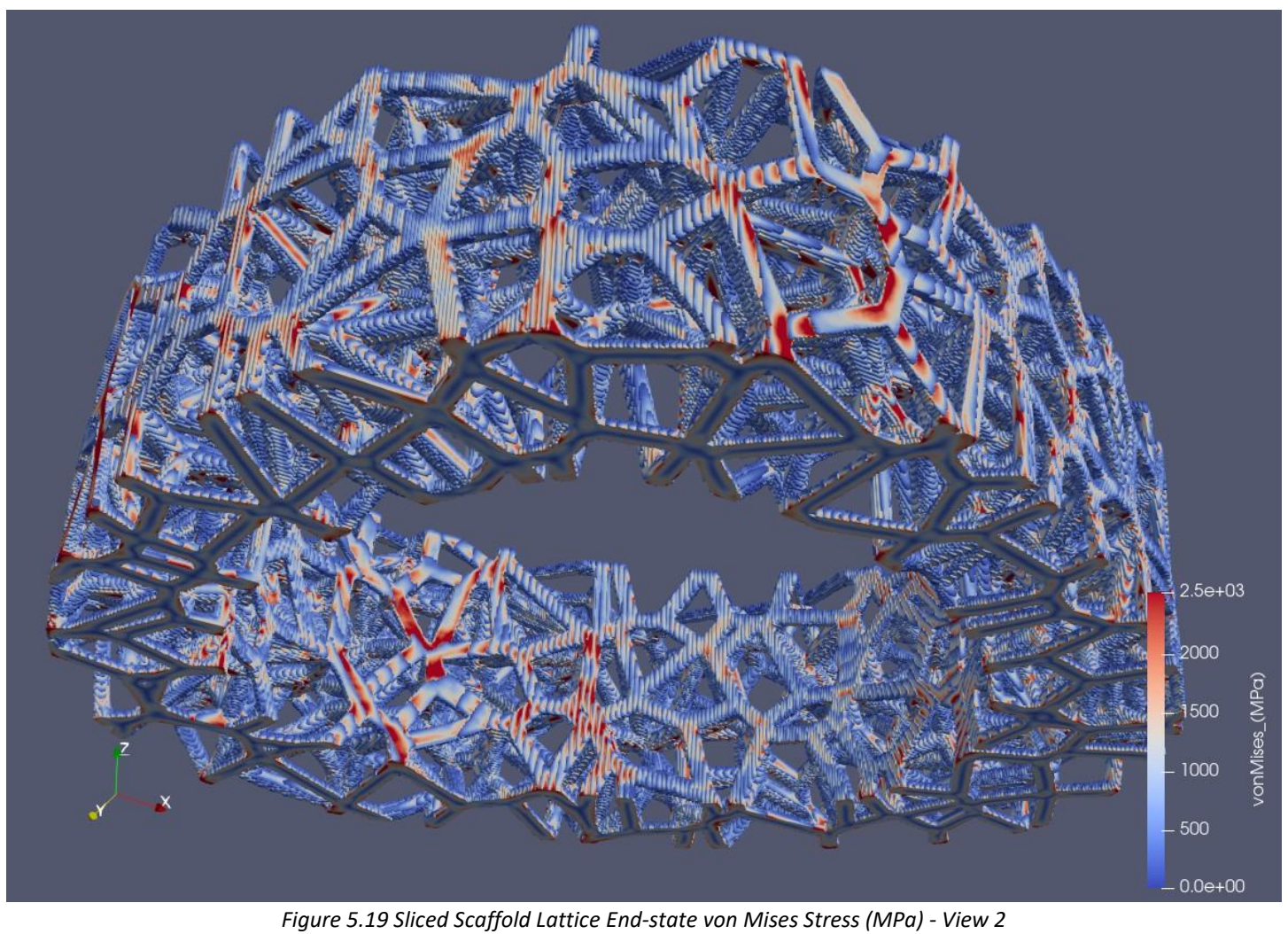


Figure 5.18 Sliced Scaffold Lattice End-state von Mises Stress (MPa) - View 1



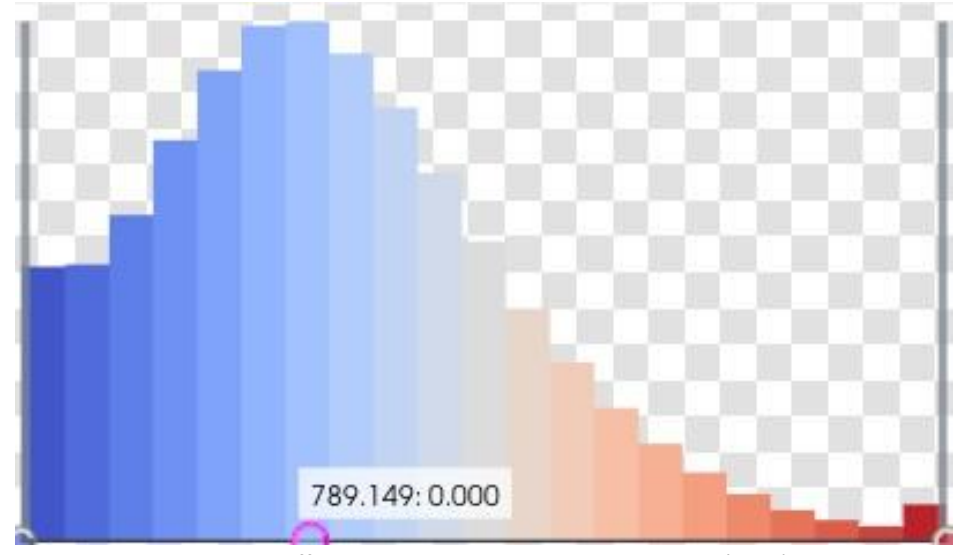


Figure 5.20 Sliced Scaffold Lattice End-state von Mises Stress (MPa) Histogram

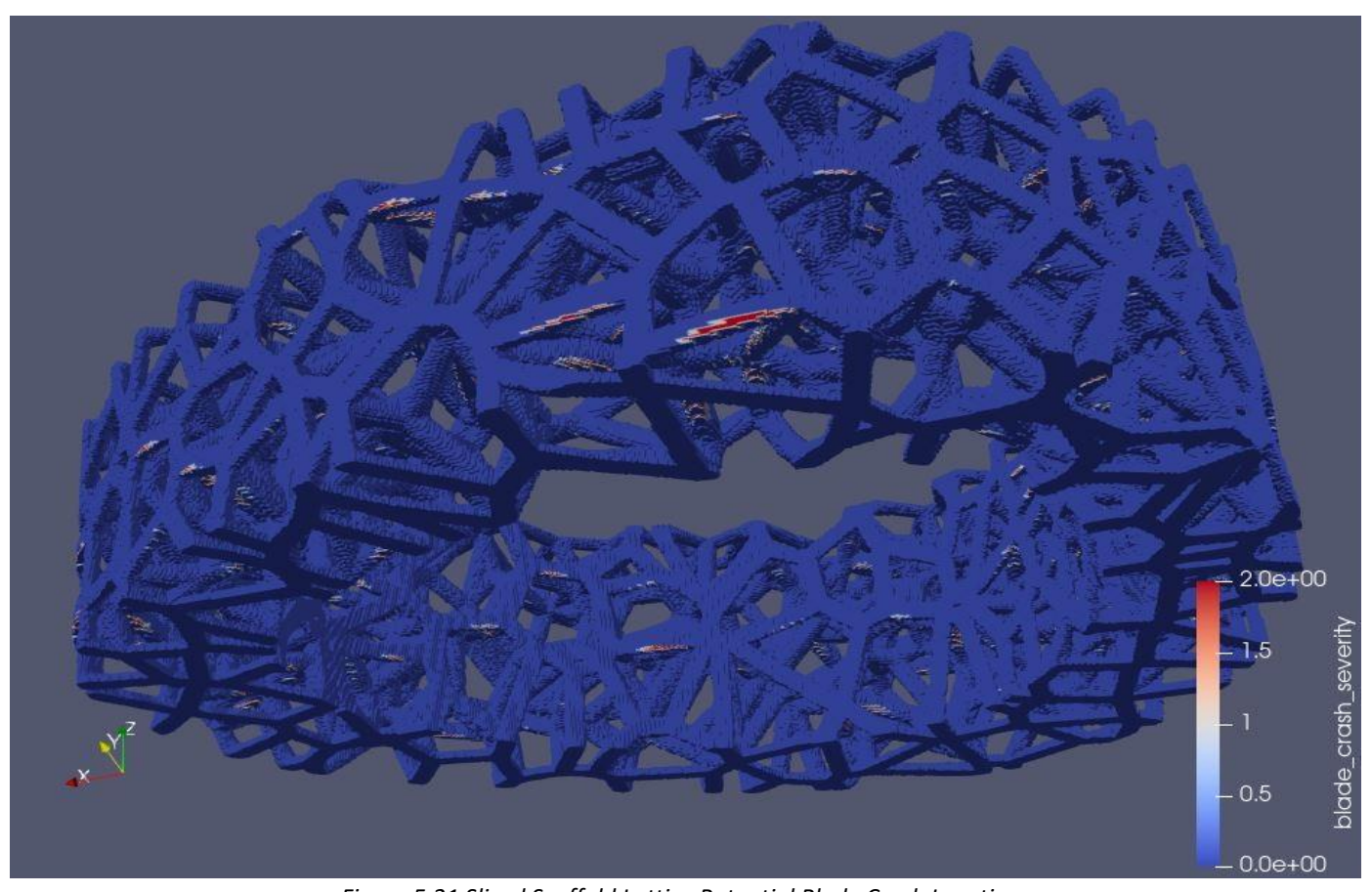


Figure 5.21 Sliced Scaffold Lattice Potential Blade Crash Locations

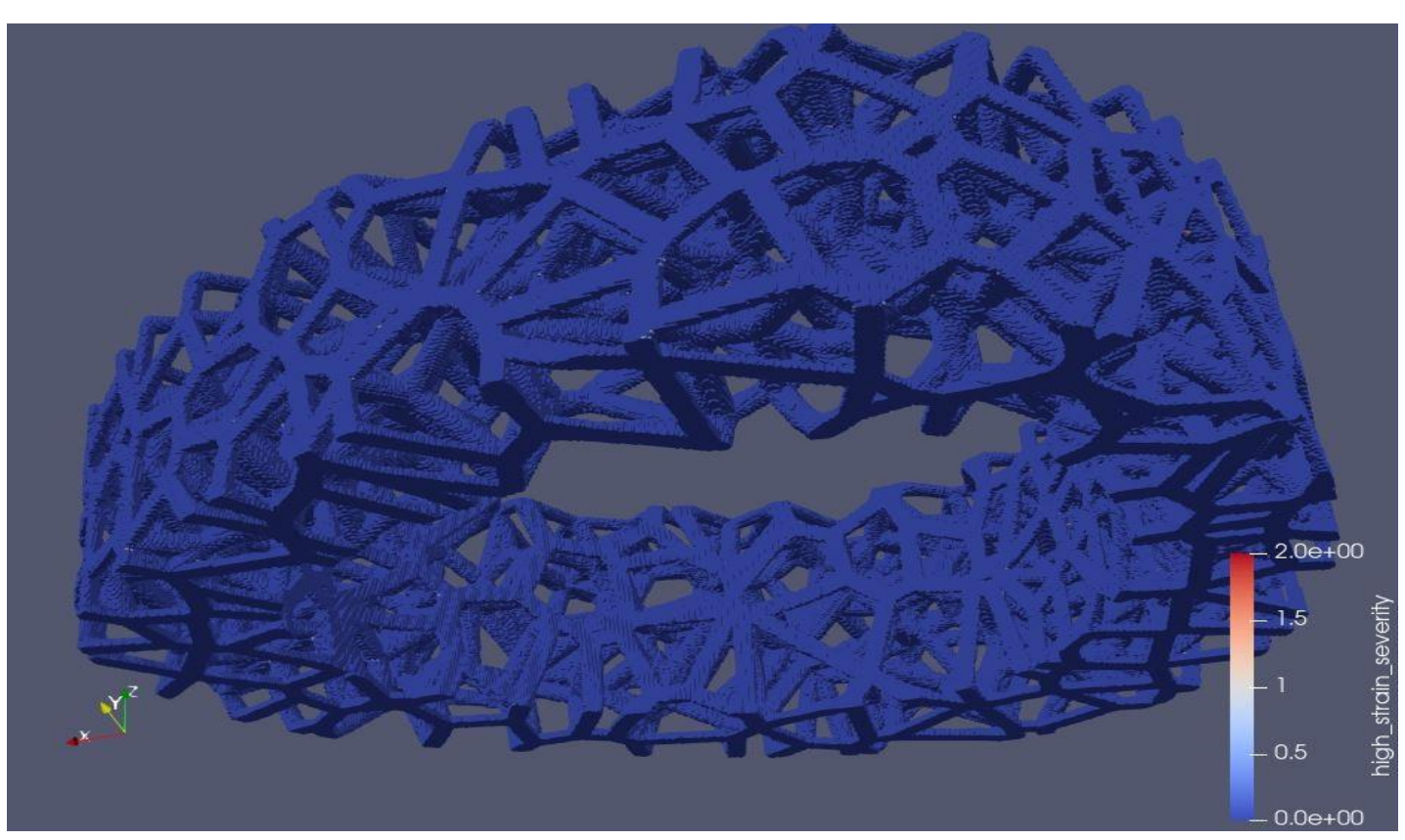


Figure 5.22 Sliced Scaffold Lattice High Strain Severity Locations

Observations on the 10 mm High-Resolution Slice Simulation

The 10 mm slice simulation offers significantly enhanced spatial resolution, and this added fidelity brings valuable insights that the full lattice simulation could only hint at.

From the displacement maps, we see localized deformation more clearly-particularly at overhangs and curved struts-in the lower parts of the scaffold that we simulated. The simulation reveals how some nodes and beams bear disproportionate loads, and small gaps or asymmetries in the geometry are now resolved. These details were previously obscured in the full scaffold simulation due to its coarser element sizing.

In our simulations, the 10 mm slice of the scaffold exhibited significantly higher end-state Von Mises stress values, often approaching or exceeding the yield strength of titanium, compared to the full scaffold simulation. This difference can be attributed primarily to the finer voxel resolution used in the slice, that enables more precise capture of local stress concentrations that are often smoothed out in the coarser full-scale models. Additionally, the slice model lacks the thermal inertia of the full scaffold, meaning that heat induced stress redistribution across the full geometry is reduced. This explains the elevated stress levels, especially near the boundaries. Collectively, these factors explain the observed increase in stress values within the higher resolution 10mm slice model. Other than the elevated values, the von Mises stress plots show higher-definition stress bands tracing along strut paths, with peaks now easily attributable to specific regions, such as the free inner and outer surfaces, internal corners and beam intersections. Compared to the full lattice simulation, this view makes it far easier to isolate problematic regions for design iteration or print path optimization.

As we previously saw in the full scaffold simulation, not many high strain severity regions are observed. The undersupported overhangs and the nodes that they connect do present elevated strain. These areas can be flagged for potential early failure under cyclic loading that the scaffold is going to face during its use.

Lastly, the blade crash severity visual provides more information at this scale. Local features like overhanging struts that may intersect with the recoater blade path are more clearly visible. This level of resolution is essential for accurate recoater crash prediction and mitigation strategies.

In conclusion, the 10 mm high-resolution slice delivers the clarity that complements the macro-level insights of the full lattice model. Together, they form a comprehensive multi-scale analysis approach, where the coarse model identifies global trends, and the slice model exposes actionable local risks and performance bottlenecks.

5.3.3 Cube Lattice Simulation

To understand how different Selective Laser Melting (SLM) printing parameters impact the mechanical behavior of the implant, we conducted a controlled simulation on a 10 mm cubic sample with the same lattice structure as the implant. Utilizing again the NTop Platform we created the cubes sample lattice shown in the picture below.

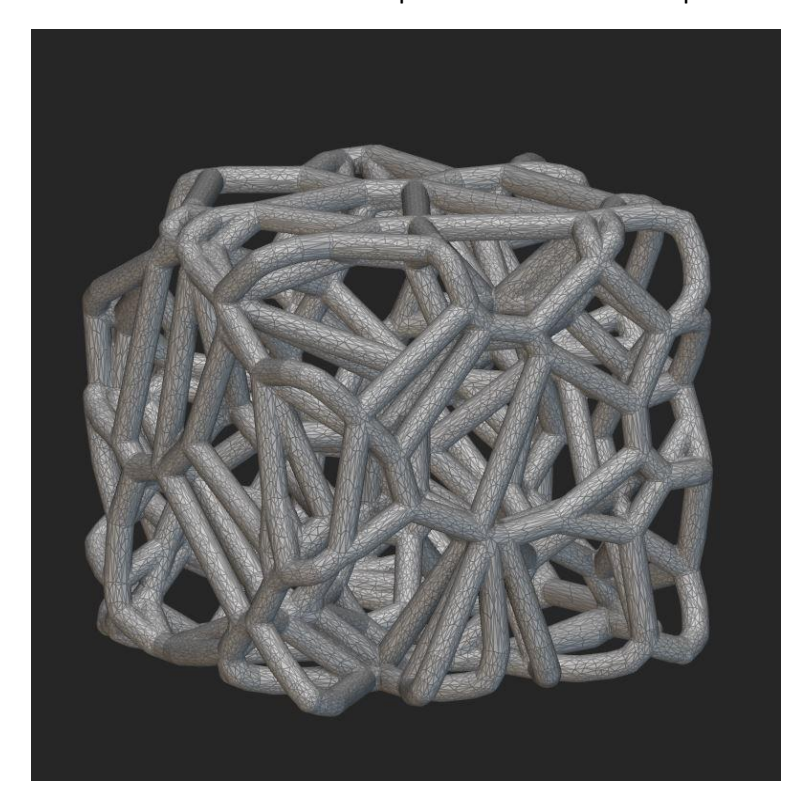


Figure 5.23 Cube Shaped Lattice Mesh

The study involved modifying one parameter at a time from the default values to isolate its effects. The parameters analyzed were [23]:

- Laser Power (W): Higher power improves fusion but may introduce excessive heat stress.
- Laser Width (mm): Affects layer bonding and density of printed material.
- Layer Height (μm): Impacts surface roughness and mechanical performance.
- Scan Speed (mm/s): Alters heat input, affecting residual stress and porosity.

The cube simulations allow for a controlled environment to assess how varying printing parameters directly impacts the mechanical behavior and printability of the Voronoi lattice structure. By isolating this variable while keeping geometry constant, the influence of the above parameters on displacement, stress accumulation, recoater interaction, and strain localization becomes much clearer. In these simulations, we evaluated the **maximum Von Mises stress occurring during the printing process**, rather than the **end-state stress**. This approach was chosen because it more clearly highlights the impact of each initial printing parameter. The peak stresses experienced during the build are typically higher than the residual stresses present in the final, cooled part, making them more effective for comparing how different parameters influence stress development.

1. Displacement / Distortion (mm)

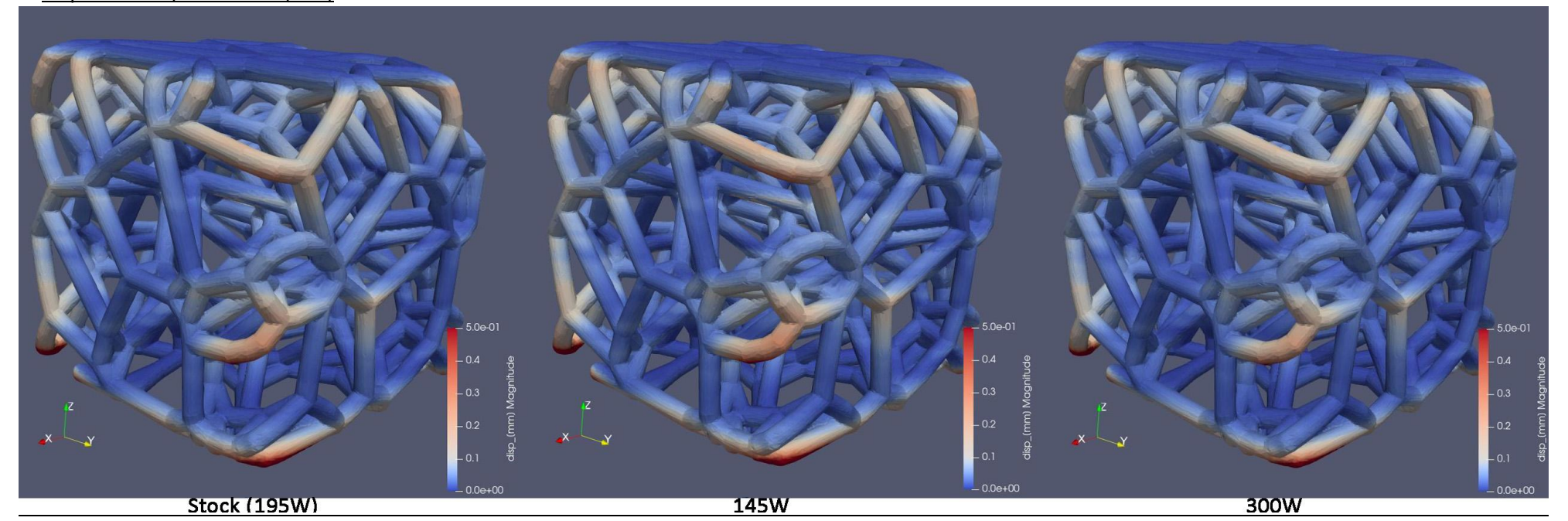


Figure 5.24 Cube Lattice Displacement (mm) Comparison for Variable Laser Power - View 1

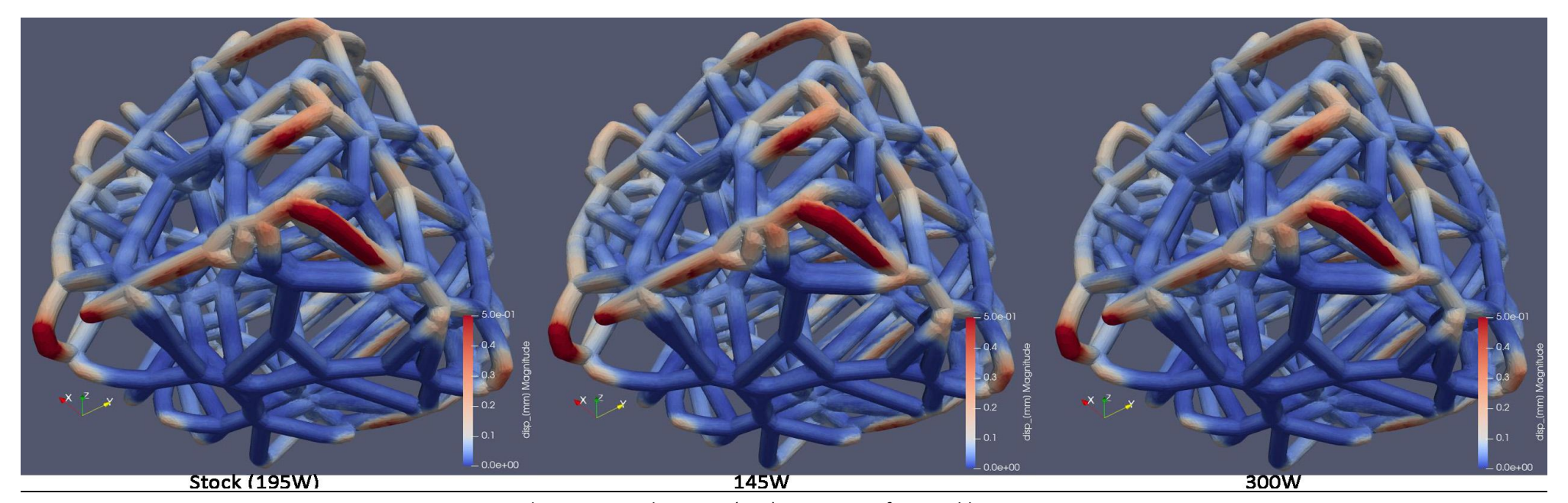


Figure 5.25 Cube Lattice Displacement (mm) Comparison for Variable Laser Power - View 2

2. Max von Mises Stress (MPa)

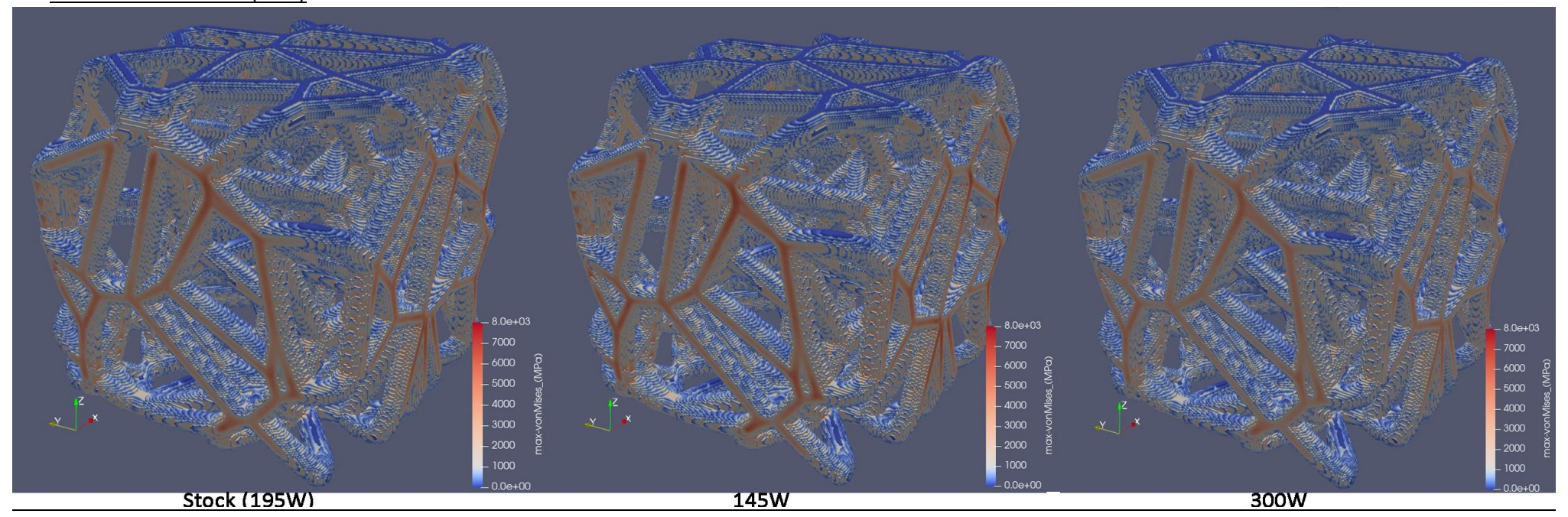


Figure 5.26 Cube Lattice Max von Mises Stress (MPa) Comparison for Variable Laser Power

3. Potential Blade Crash Locations

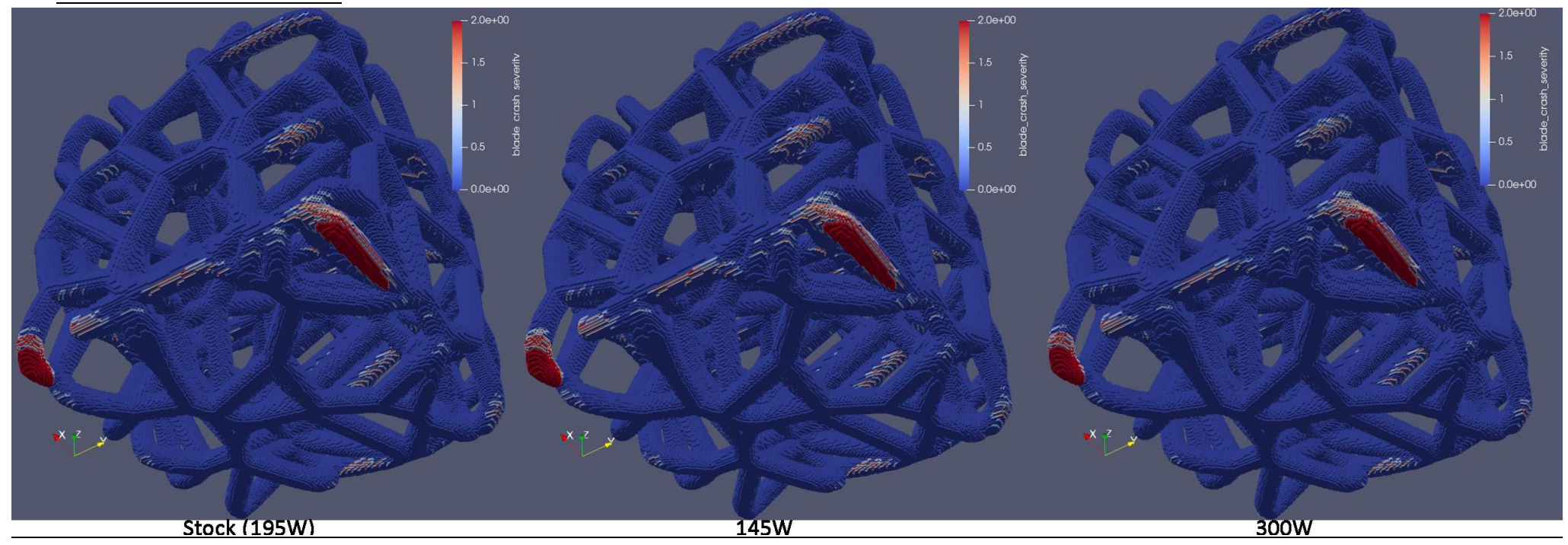


Figure 5.27 Cube Lattice Potential Blade Crash Locations Comparison for Variable Laser Power

4. High Strain Severity

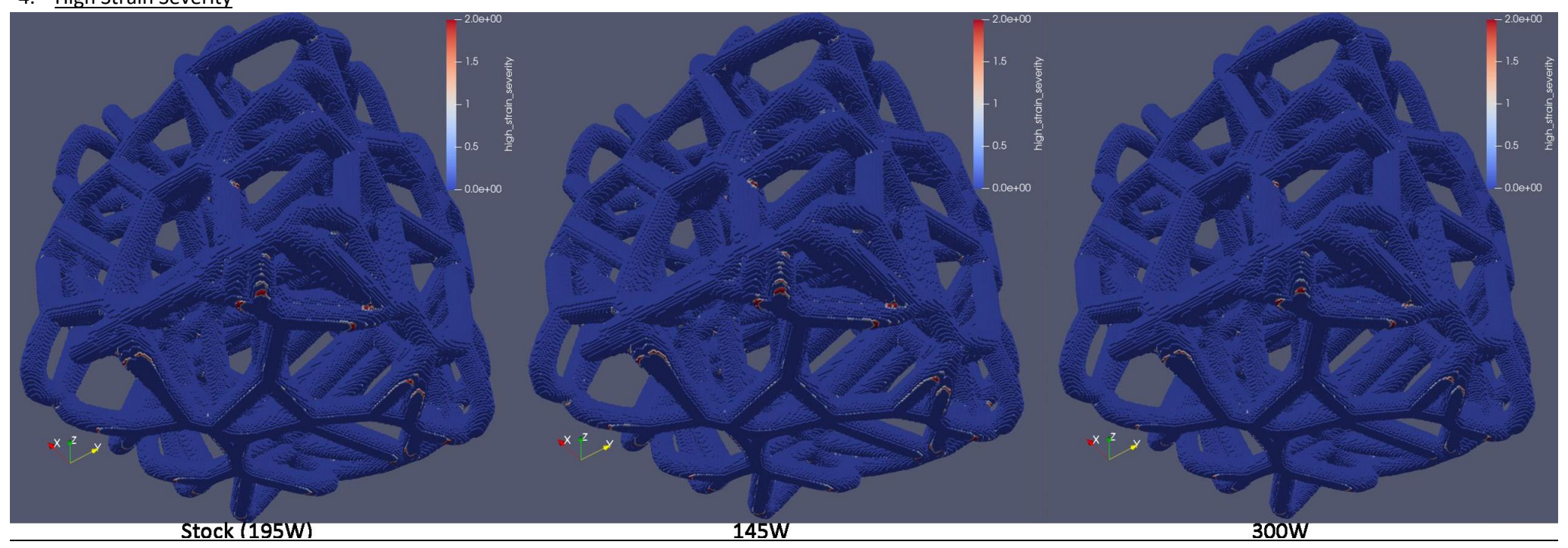


Figure 5.28 Cube Lattice High Strain Severity Locations Comparison for Variable Laser Power

Observations on the Cube Simulation with Varying Laser Powers (145 W, 195 W, 300 W)

The cube simulations provide a focused and consistent geometry to isolate the influence of laser power on mechanical performance and manufacturability indicators.

In terms of displacement, the results show that the lowest laser power setting (145 W) produces the greatest deformation, particularly around unsupported or overhanging struts. This is expected, as insufficient energy input may cause incomplete fusion between layers, weaker inter-layer adhesion, and consequently, a higher tendency for thermal contraction and distortion. The 195 W setting, which may be considered a mid-point or stock value, presents a much more balanced displacement profile—distortion is moderate and more evenly distributed. The highest power setting of 300 W does further reduce displacement. At these levels of laser power we do not seem to have any problems with overheating, or stress accumulation during cooling.

The von Mises stress maps reveal important distinctions in structural performance. At 145 W, the stress distribution appears relatively mild but less cohesive—indicative of a potentially under-fused structure with low internal continuity. Conversely, 195 W produces clearly defined stress pathways along load-bearing members, suggesting optimal energy input for material fusion and mechanical continuity. The 300 W setting shows a similar stress layout, with lower overall values and with slightly more diffusion in stress zones. This could reflect excess melting or material inconsistencies introduced by over-processing, which may not benefit mechanical performance and could even introduce brittleness in localized regions.

When looking at blade crash potential, a critical aspect of additive manufacturability, great differences are observed. The 145 W setting presents the highest risk of blade crash, with notable red regions suggesting material protrusions likely caused by thermal warping and recoater interference. These protrusions are common in parts with poor bonding alongside with residual stress buildup. The 195 W power level reduces these risks significantly and at 300 W the red zones are even fewer. This progression suggests that higher laser powers help with better layer melting and fusion, thereby decreasing susceptibility to blade collision incidents due to deformation or weak bonding in those zones.

In terms of high strain severity, the 145 W simulations show widely distributed but poorly defined strain zones, reflecting weaker structural integrity from under-fused struts. The 195 W configuration again appears most optimal, with strain neatly localized at logical mechanical junctions and transitions. The 300 W setting shows slightly muted strain fields, likely due to broader heat distribution and a more ductile response in simulation—but this could mask potential microstructural brittleness not captured in a purely elastic-plastic simulation model.

Overall, these results suggest that 195 or 300 W laser power offers the best trade-off between dimensional accuracy, structural performance, and manufacturing reliability for this type of lattice structure. The 145 W option is clearly suboptimal, introducing poor mechanical continuity and print instability. The 300 W option seems to produce better results but it may introduce new risks related to thermal overshoot and blade interference, more research and experimentation is suggested.

All of the above highlight the importance of laser power optimization not only for strength but also for successful, reproducible printing of complex implants with Voronoi lattice structure.

5.3.3.2 Laser Width 80μm, 100μm, 120μm

1. <u>Displacement / Distortion (mm)</u>

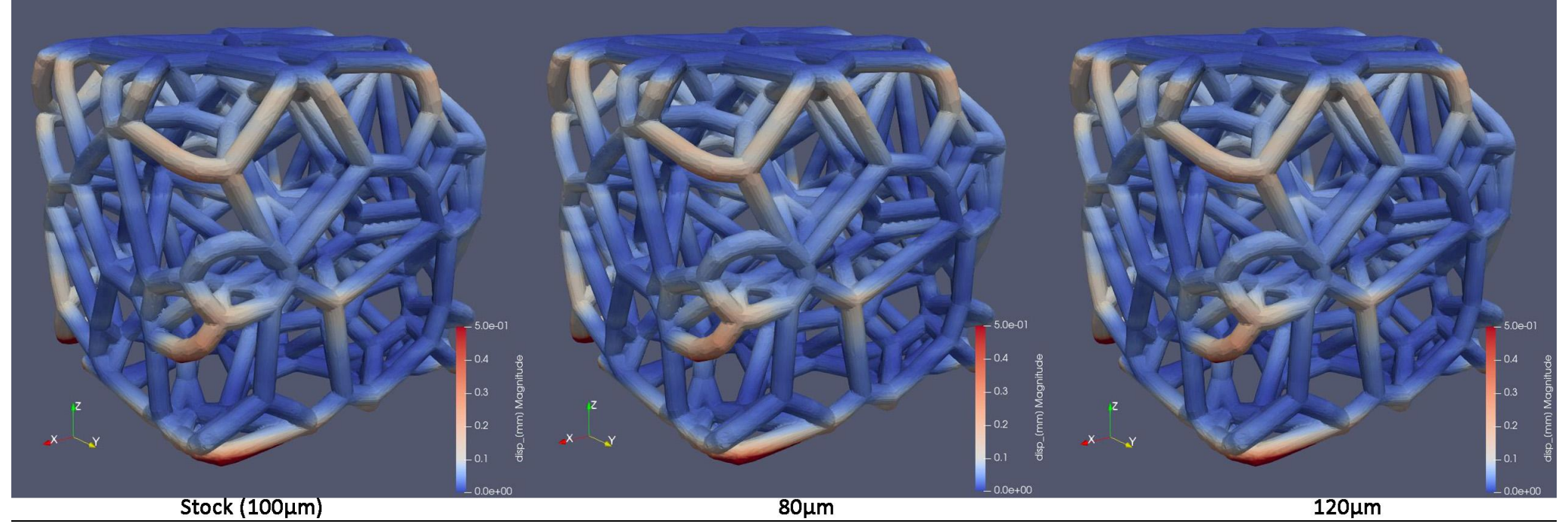


Figure 5.29 Cube Lattice Displacement (mm) Comparison for Variable Laser Width

2. Max von Mises Stress (MPa)

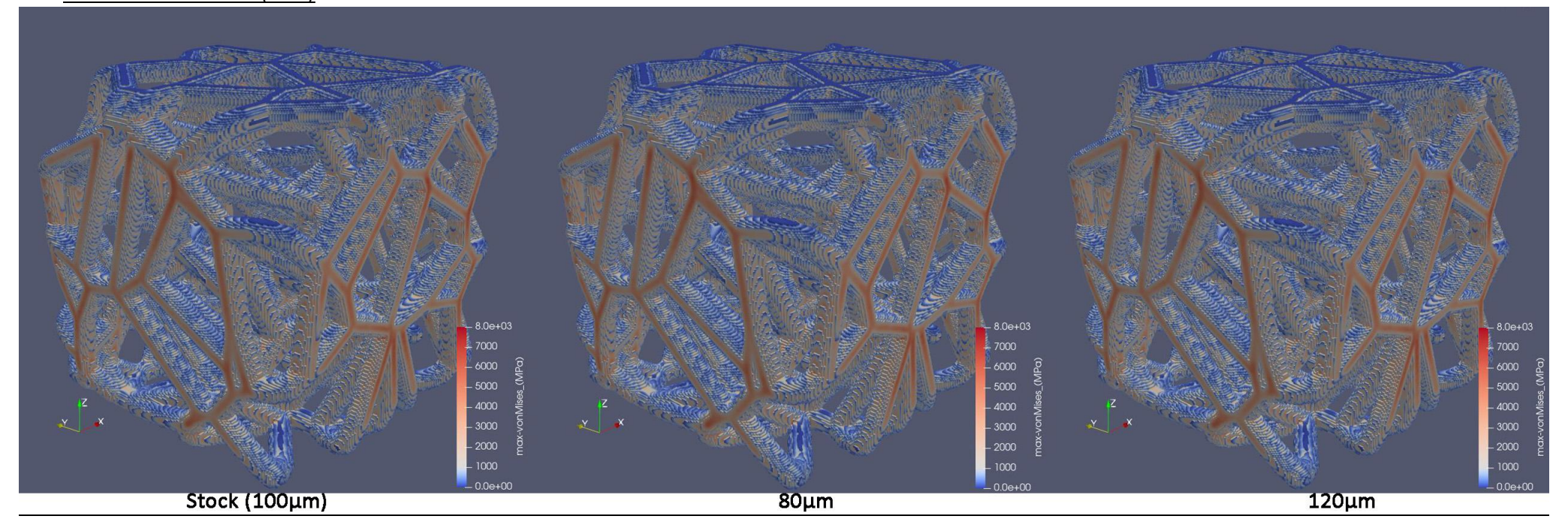


Figure 5.30 Cube Lattice Max von Mises Stress (MPa) Comparison for Variable Laser Width

3. Potential Blade Crash Locations

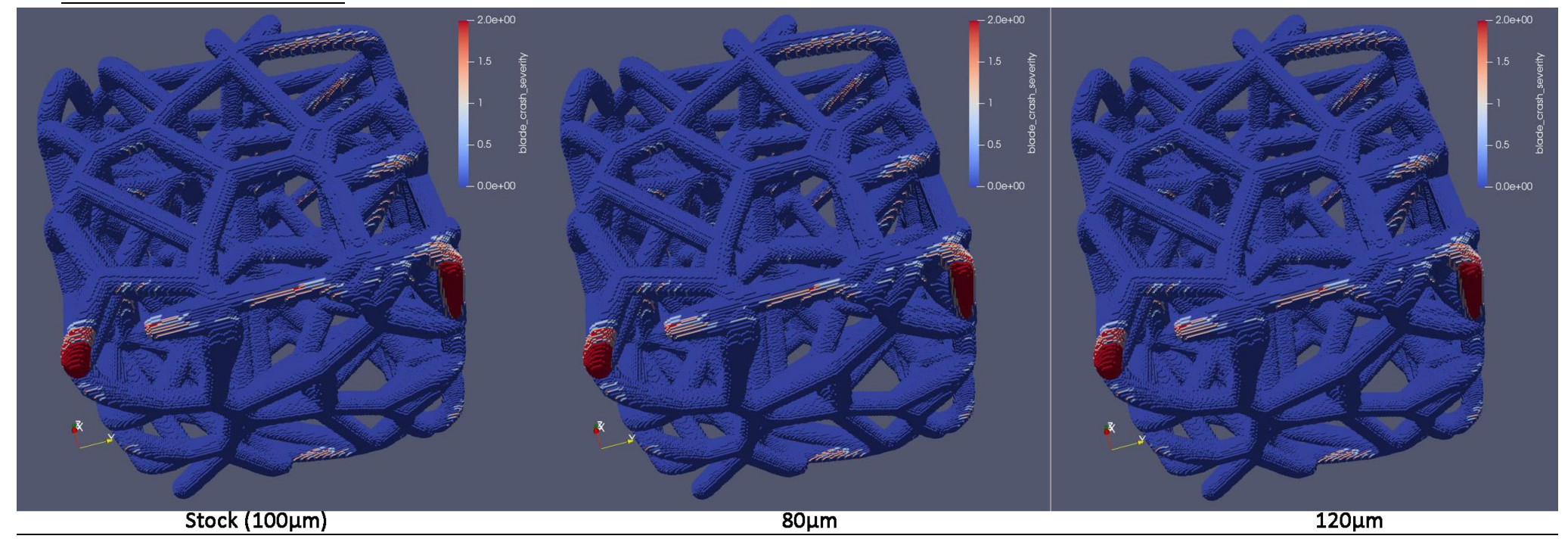


Figure 5.31 Cube Lattice Potential Blade Crash Locations Comparison for Variable Laser Width

4. High Strain Severity

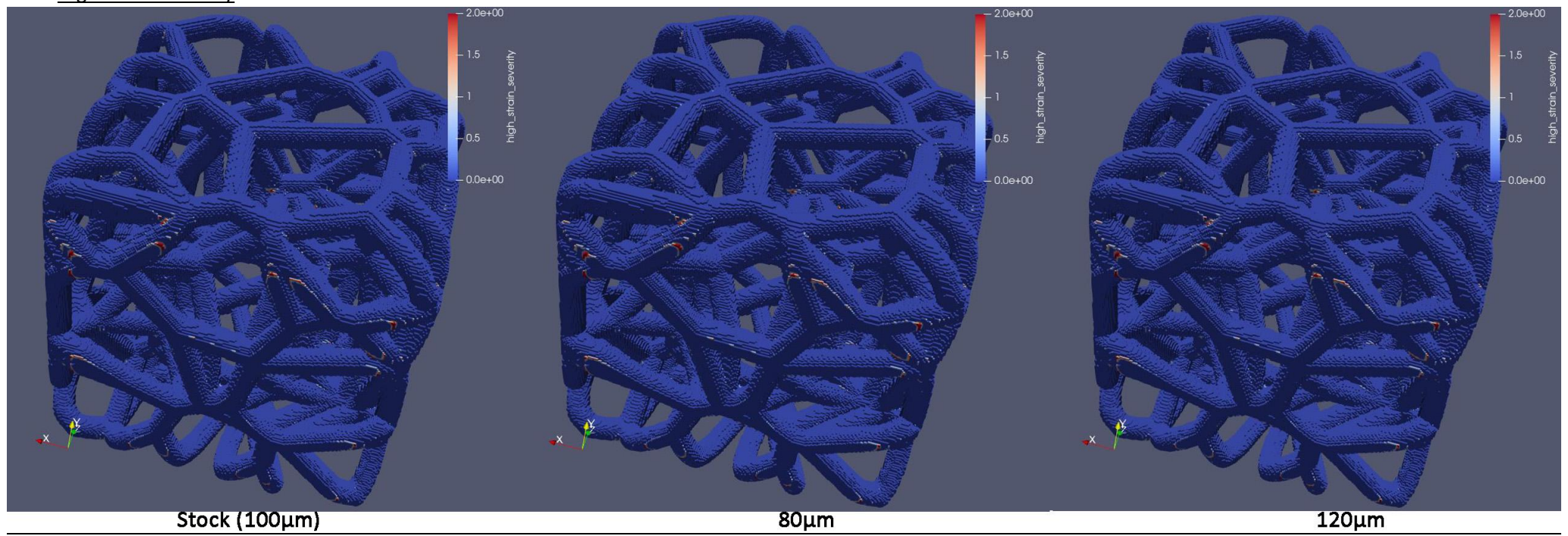


Figure 5.32 Cube Lattice High Strain Severity Locations Comparison for Variable Laser Width

Observations on the Cube Simulation with Varying Laser Beam Widths (80μm, 100μm, 120μm)

Laser beam width is commonly a machine specific parameter. The cube simulations conducted with different laser beam widths— $80\mu m$, $100\mu m$ (stock), and $120\mu m$ —offer some insight into how beam diameter influences print fidelity, mechanical integrity, and manufacturing risks in a consistent lattice structure. Since the beam width directly affects the energy distribution profile, melt pool size, and track overlap, even subtle changes can lead to meaningful differences in structural behavior.

In terms of displacement, all three beam widths produced very similar deformation patterns, with no major differences in the overall magnitude or distribution of distortion. The results suggest that, within this controlled range, beam width has a relatively minor influence on thermal distortion for this lattice geometry.

Blade crash severity was similarly consistent across the three beam widths. All three configurations showed low crash potential, with only minimal red zones detected—primarily on sharp overhangs or unsupported tips. There was no meaningful increase or decrease in recoater interference risk with increasing beam width, which implies that within the tested range, beam diameter does not critically affect surface swelling or upward bulging that might lead to recoater contact. This is an important finding, as it suggests that beam width can potentially be increased for faster builds without sacrificing build stability.

The max von Mises stress distributions across the three simulations also followed very comparable patterns. The load-bearing paths through the lattice were similarly highlighted in all cases, with stress concentrated near node junctions and internal supports. Minor differences were present: the 80µm setting showed slightly sharper and more fragmented stress zones, while the 120µm setting displayed a slightly more diffuse pattern. This could reflect a trade-off between melt precision and bonding consistency—smaller beams offer better feature resolution, while wider beams ensure more continuous material fusion.

When analyzing high strain severity, the results again indicate subtle if any changes. All the settings performed similarly, with localized high-strain zones appearing primarily where expected—at curved members or unsupported transitions. No major strain anomalies were introduced by changing the beam width, and all settings maintained reasonable mechanical continuity.

Overall, the cube simulations indicate that laser beam width within the range of $80-120\mu m$ has minimal impact on global mechanical behavior and manufacturability, at least in this lattice configuration. While $80\mu m$ may provide slightly sharper stress localization and resolution, it could also increase sensitivity to poor bonding. The $120\mu m$ setting, on the other hand, offers marginally smoother mechanical distributions and may allow for increased build rates without sacrificing structural quality. The $100\mu m$ setting remains a balanced midpoint, but the results suggest that both narrower and wider beam widths are viable, depending on whether resolution or print speed is prioritized in the manufacturing process. As a final comment, since laser beam width did not significantly influence the results in the cube lattice simulations, machine selection can prioritize other factors—such as reliability, speed, or cost—without concern for minor variations in beam width.

5.3.3.3 Layer Height 30μm, 50μm, 70μm

1. <u>Displacement / Distortion (mm)</u>

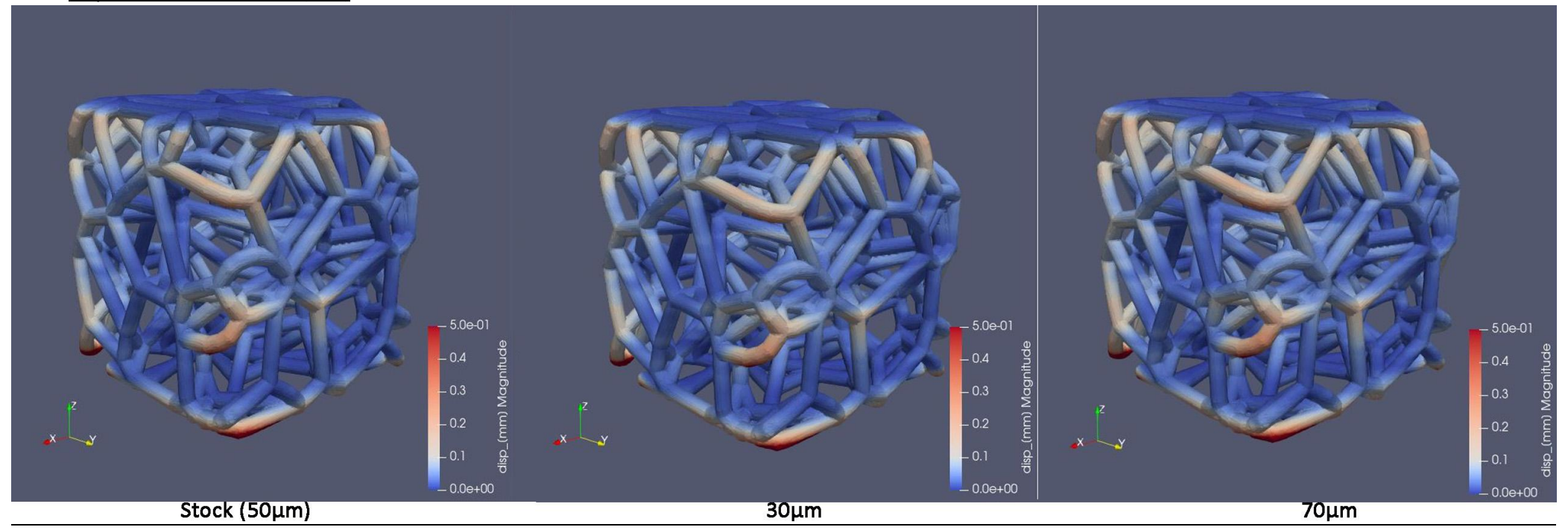


Figure 5.33 Cube Lattice Displacement (mm) Comparison for Variable Layer Height - View 1

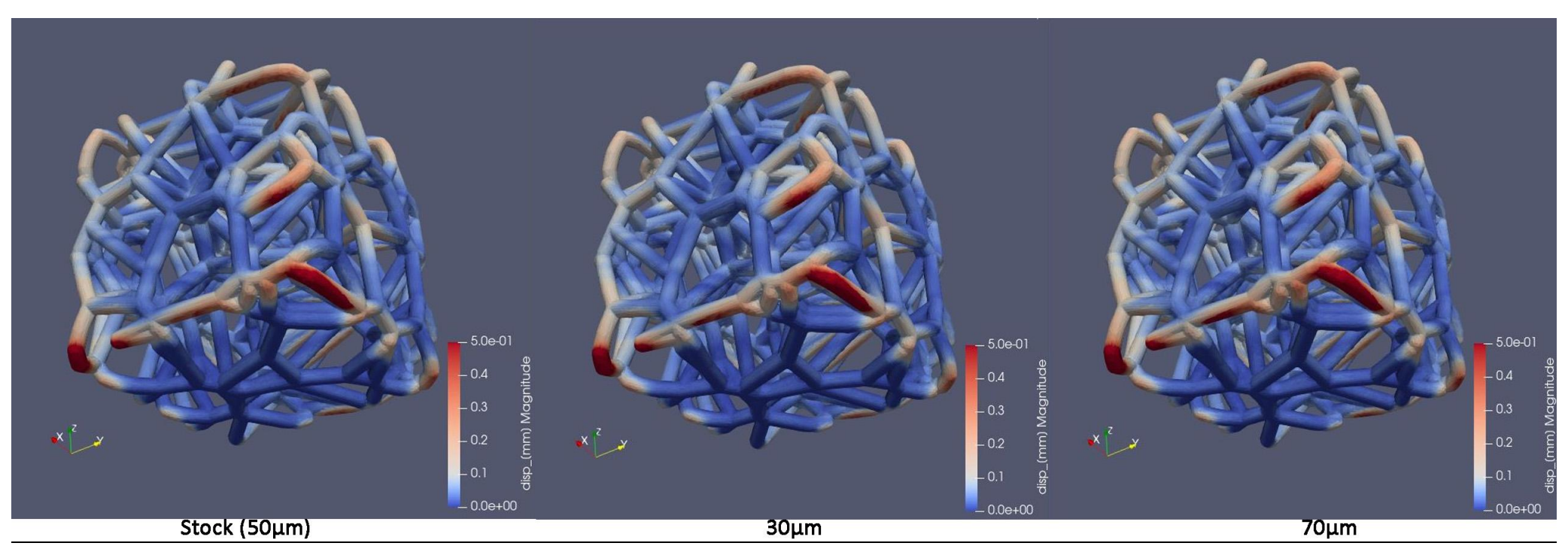


Figure 5.34 Cube Lattice Displacement (mm) Comparison for Variable Layer Height - View 2

2. Max von Mises Stress (MPa)

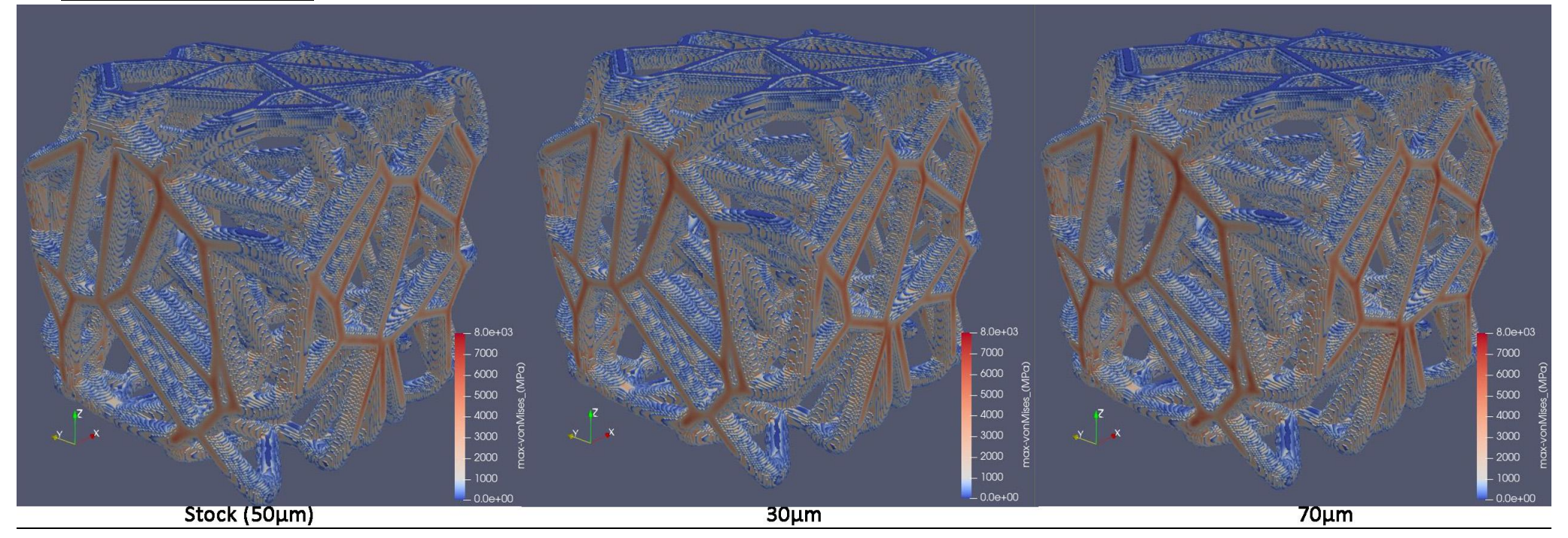


Figure 5.35 Cube Lattice Max von Mises Stress (MPa) Comparison for Variable Layer Height

3. Potential Blade Crash Locations

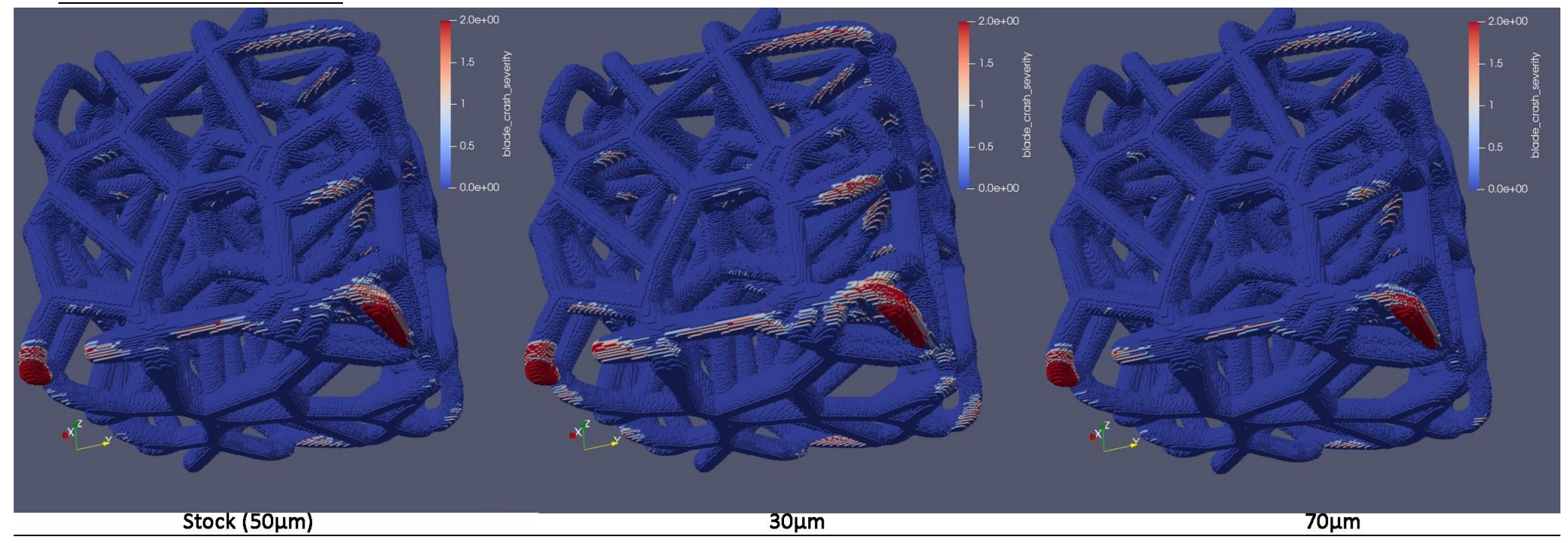


Figure 5.36 Cube Lattice Potential Blade Crash Locations Comparison for Variable Layer Height

4. High Strain Severity

A stock (50μm)

30μm

70μm

Figure 5.37 Cube Lattice High Strain Severity Locations Comparison for Variable Layer Height

Observations on the Cube Simulation with Varying Layer Heights (30μm, 50μm, 70μm)

The cube simulations conducted with different layer heights—30µm, 50µm (stock), and 70µm—offer a clear view of how layer thickness affects the mechanical response, thermal distortion, and manufacturing risks of a lattice structure during selective laser melting (SLM). Layer height directly influences vertical resolution, melt pool overlap, and heat accumulation per layer, making it a critical parameter for both print quality and process reliability.

In terms of displacement, the 30 and 50µm layer heights show very similar deformation trends, highlighting superior control over thermal gradients. The smaller layer thickness allows for better heat dissipation and bonding consistency, resulting in a more dimensionally accurate print. In contrast, the 70µm setting results in visibly increased deformation, particularly in poorly supported and thin features. The thicker layers accumulate more heat before each solidification cycle, leading to greater residual stresses and larger geometric warping.

Regarding blade crash severity, a different trend is evident. The $70\mu m$ setting performs best, showing minimal risk of blade interference. This is due to the larger layer height, reducing the likelihood of bulges or warping to rise above the intended Z-axis step of the recoater blade. The $50\mu m$ simulation shows moderate crash zones, generally limited to corners and transitions. The $30\mu m$ setting, however, introduces more severe crash risks—particularly in overhanging features—where the very small rise of the recoater blade in each pass makes it more likely to collide with vertical growths that encroach into its path.

In terms of von Mises stress distribution, the $50\mu m$ stock setting reveals the most continuous stress paths across the lattice. The $30\mu m$ layer height provides similar results but with marginally higher peak values during the printing process. At $70\mu m$, the max von Mises stress takes higher values, likely due to irregular bonding between the thicker, layers caused by the poor melting of the material, regarding of course the constant laser power.

When examining high strain severity, the 30μ m configuration again performs best, showing localized and structurally realistic high strain risk areas, especially in the lattice beams junctions. This implies a stable and predictable mechanical response. The 50μ m case performs very similarly to the 30μ m, it might introduce slightly more high strain areas but barely noticeable on the diagrams. The 70μ m setting shows more dispersed and irregular strain concentrations. These may be indicative of inconsistent bonding or variable stiffness across the height of the part due to thermal instability in thicker layers.

In summary, the cube simulation results strongly favor the 50µm layer height as it offers a great balance between geometric precision, stress behavior, and manufacturing safety. The 30µm setting could offer better printing accuracy especially if coupled with a smaller laser beam diameter, but the compromises in printing speed and introduces higher probability of the recoater blade crashing, making it not worth the risk. In contrast, the 70µm setting introduces measurable drawbacks in most major aspects like distortion, mechanical integrity, and strain concentration, only showing improvements in the blade crash risk, making it less suitable for complex lattice structures where precision and performance are critical.

5.3.3.4 Scan Speed 600mm/s, 1000mm/s, 1400mm/s

1. <u>Displacement / Distortion (mm)</u>

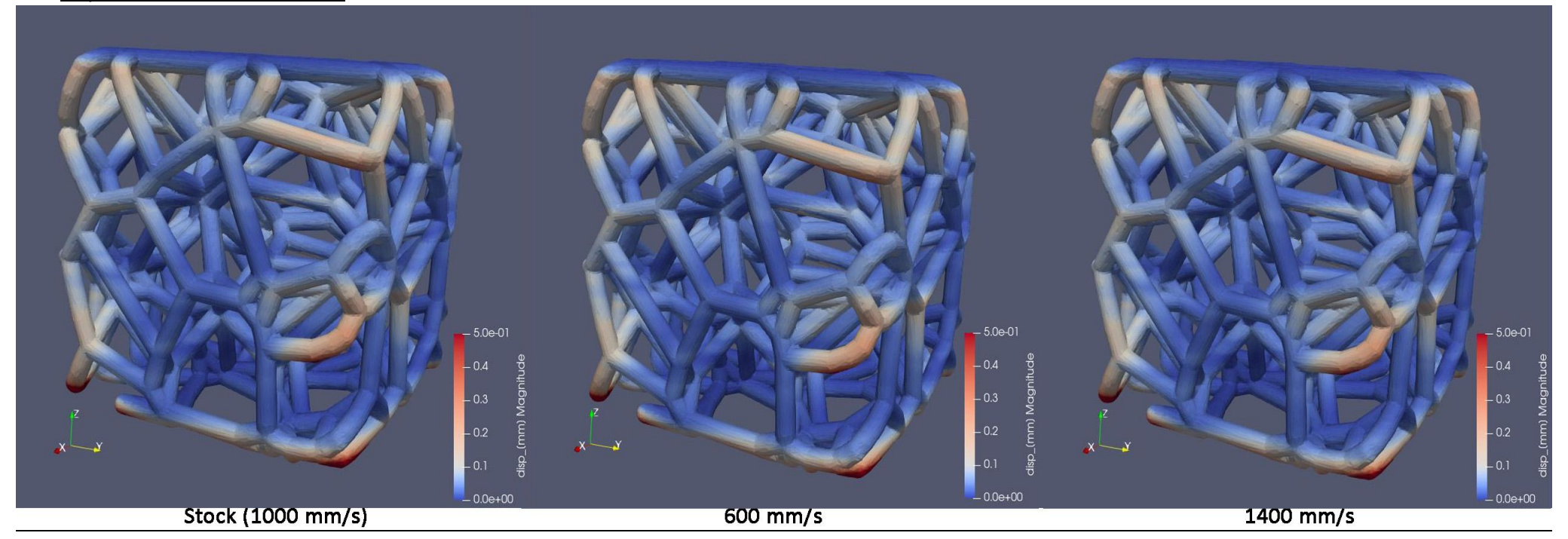


Figure 5.38 Cube Lattice Displacement (mm) Comparison for Variable Scan Speed-View 1

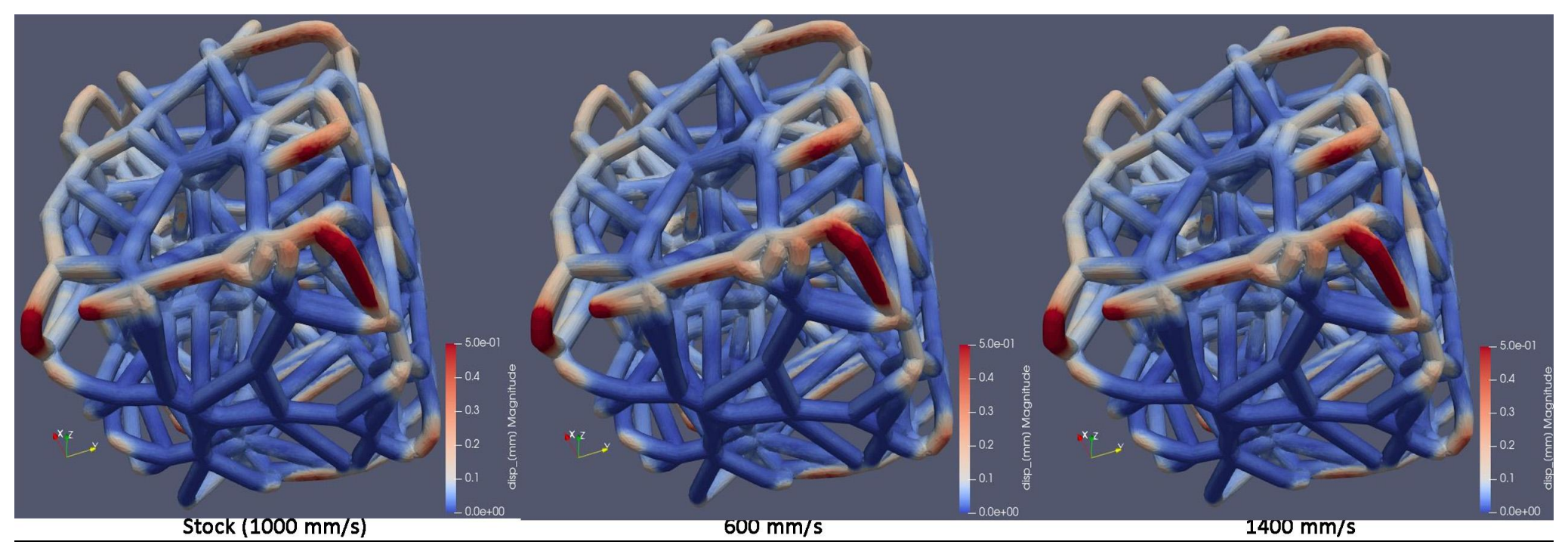


Figure 5.39 Cube Lattice Displacement (mm) Comparison for Variable Scan Speed - View 2

2. Max von Mises Stress (MPa)

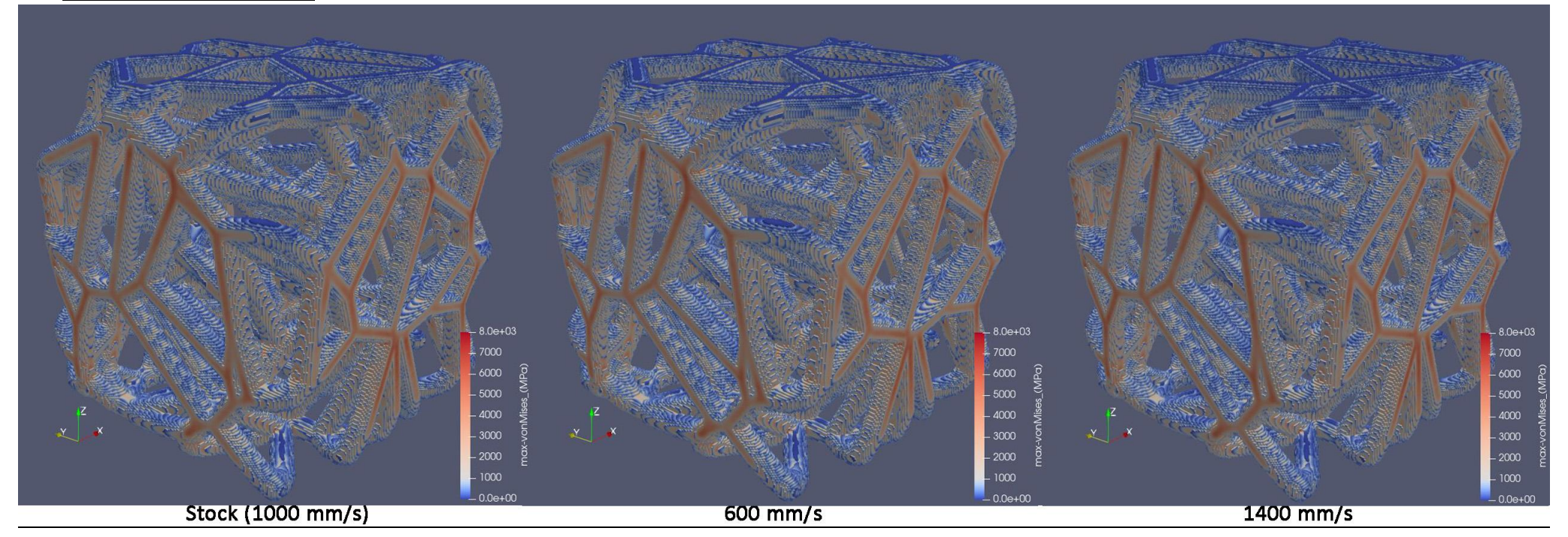


Figure 5.40 Cube Lattice Max von Mises Stress (MPa) Comparison for Variable Scan Speed

3. Potential Blade Crash Locations

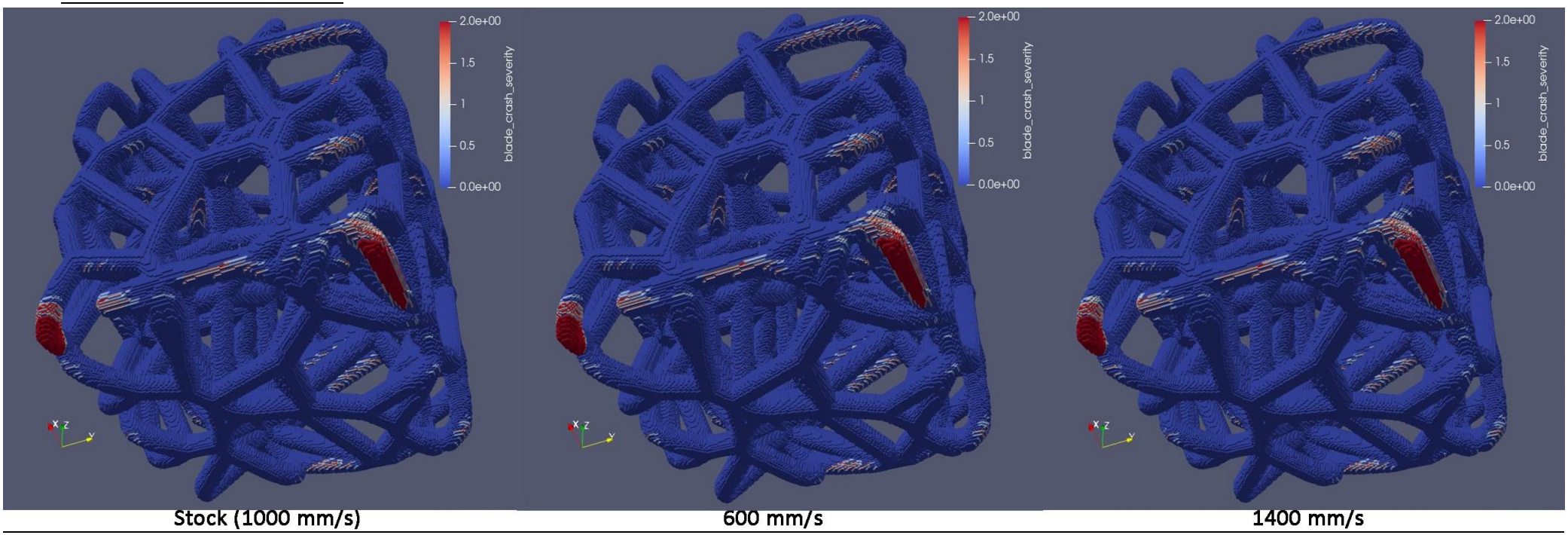


Figure 5.41 Cube Lattice Potential Blade Crash Locations Comparison for Variable Scan Speed

Figure 5.42 Cube Lattice High Strain Severity Locations Comparison for Variable Scan Speed

Observations on the Cube Simulation with Varying Scan Speeds (600 mm/s, 1000 mm/s, 1400 mm/s)

The cube simulations using three different scan speeds (600 mm/s, 1000 mm/s (stock), and 1400 mm/s) highlight how laser traversal velocity impacts thermal behavior, structural stability, and print reliability in selective laser melting of lattice structures. Since scan speed directly influences energy input per unit area, faster or slower movement across the powder bed changes melt pool dynamics, layer bonding, and residual stress development.

The displacement results from the cube lattice simulations across varying scan speeds (600 mm/s, 1000 mm/s, and 1400 mm/s) demonstrate a consistent and notably uniform deformation pattern. From both the front and bottom perspectives, the maximum displacement values remain within the same general regions, typically at the corners and lower support beams, regardless of the scan speed. The color scale indicates only slight differences in the magnitude of displacement, with no significant redistribution or escalation of strain concentrations as the speed increases. With the 1400 mm/s scan speed setting, maybe the slightest increase in displacement can be observe, indicating worse layer fusion due to less energy being deposited in each material layer. These visual similarities suggest that, for this particular lattice geometry and loading condition, variations in scan speed within this range do not drastically affect the global mechanical response in terms of displacement.

For blade crash severity, all three scan speeds exhibit localized high-risk zones, particularly near overhanging features and horizontal members. While the high-risk areas appear in nearly the same locations across all scan speeds, their intensity marginally increases with speed. This suggests that faster scan speeds might contribute to more aggressive material buildup or thermal gradients, which in turn elevate the risk of recoater blade interference.

The maximum von Mises stress distributions during printing also show only subtle variation, with stress primarily accumulating at key junctions and truss intersections. Notably, stress peaks remain in the same regions regardless of scan speed, implying that the lattice maintains a consistent stress distribution pattern across different thermal cycles, which is a positive indicator of print reliability.

Lastly, in terms of high strain severity, the results are uniformly low across all scan speeds, with negligible red zones. The structure demonstrates minimal strain accumulation during the build, underscoring its robustness under thermal and mechanical loads imposed during additive manufacturing. This further supports the conclusion that the simulated lattice geometry is tolerant to variations in scan speed.

In summary, although small gradients in displacement, stress, and crash severity are visible with increasing scan speed, the changes are minimal. This indicates that faster scan speeds than the stock setting could be used to accelerate the manufacturing process of the scaffold.

5.4 Final Comments on Printing Parameters and Scaffold Design Modifications for Better Manufacturability

Based on the above analysis of both full and sliced scaffold simulations, as well as the controlled cube printing tests, several key modifications can be proposed to enhance the manufacturability and mechanical reliability of the scaffold structure. Geometrically, we could reinforce high-risk structural zones, particularly struts that appear highly displaced or crash-prone in simulation, by modestly increasing their thickness (by around 10–20%). This method can reduce deformation without significantly altering the required mechanical properties and porosity. Furthermore, the simulations demonstrate localized von Mises stress and high strain severity at the boundary flat surfaces and some junctions where multiple struts meet. By substituting smoother, filleted transitions for sharp angles, these can be lessened, improving stress distribution and reducing the possibility of fatigue or cracking during printing and use.

Reducing unsupported or cantilevered geometries is another important adjustment. Struts that overhang significantly or protrude at steep angles contribute heavily to blade crash events and poor layer adhesion, especially during the initial build layers. These features should be shortened, supported, or reoriented to minimize interference with the recoater blade. Sparse connectivity also reveals structural instability in the lower layers of the sliced scaffolds. By stabilizing the structure early in the print process with detachable support scaffolds or by permanently densifying the base region, this problem can be resolved. Ensuring consistent spacing and symmetric patterns throughout the lattice also aids in maintaining thermal equilibrium during layer deposition, reducing distortion and print variability. All the design modifications should be implemented without much altering the implants mechanical characteristics, especially the strain under load, as it has proven to be of crucial importance for efficient bone regeneration.

From the cube simulations focused on printing parameters, several advantageous printer settings emerge. A laser power around the preset value of 195W appears to strike the best balance. Lower powers (such as 145W) result in poor melting and weak bonding increasing displacement and blade crash risks. Higher powers (like 300W) seem to produce very similar if ever so slightly better results than the stock value, but more testing is advised. Laser beam width around the 100µm stock value doesn't seem to greatly affect the final result. The preset layer height of 50µm layer height offers a great balance between geometric precision, stress behavior, and manufacturing efficiency, although shorter layers could further improve resolution and material bonding sacrificing printing speed. Similarly to laser beam width, scan speed changes does not seem to greatly impact the simulation results. Thus, a moderate speed of 1000 mm/s could be used for strong fusion and reduced crash risk, but also higher values could offer faster manufacturing without great sacrifices.

In summary, these complex scaffold structures can be made much more printable, less prone to mechanical failure, and more durable by combining geometric refinements like thickening weak struts, smoothing node transitions, and strengthening the base with the previously mentioned printing parameters.

6. Future Work

Even though this study has shed some light on the potential problems that the additive manufacturing of Voronoi-lattice bone scaffolds, there are still a number of directions that could advance the research and aid its further adoption.

1. High-Resolution Simulations with more Powerful Computing Resources

The full scaffold simulations were limited in the voxel density due to computational and time restraints. Although informative, their resolution restricted a finer analysis of localized stresses and deformation patterns. Future studies should be conducted in higher power systems to perform more detailed simulations of the full-scale implant geometry. Also scaffolds from other parts of the femur bone or even scaffolds for other bones could be simulated so that we could observe how different bone geometries affect the scaffold's printability.

2. Experimental Manufacturing and Validation

Although the simulations conducted with Ansys Additive offered detailed predictions about printability and mechanical response, physical validation is essential. The next logical step is the fabrication of test scaffolds based on the optimized settings determined from the cube lattice simulations. By printing these structures using selective laser melting (SLM), it will be possible to compare real-world deformation, defects, and surface quality with the simulated results. This feedback loop would be critical for verifying and refining the digital workflow, especially in relation to process parameter sensitivity.

3. Mechanical Testing Under Physiological Loading

Once the scaffolds are printed, they should be subjected to mechanical testing under cyclic loading conditions that replicate the stresses encountered in the human femur. One idea is to design and build a custom test rig to apply variable loads that mimic the stress cycles experienced during walking, running, and resting. Fatigue testing under simulated body temperatures and humidity would also be crucial for evaluating long-term performance.

4. Biocompatibility and In-Vitro Cell Studies

Beyond mechanical performance, the biological aspect of the scaffold should be addressed by conducting in-vitro studies. The test rigs mentioned before, could be evolved to observe and further quantify how the scaffolds mechanical behavior along with other characteristics like surface roughness and porosity. These experiments will help validate whether the geometrical features simulated and fabricated actually support the osteointegration goals of the implant.

5. Economic Considerations

The final step for the production of such implantable scaffolds lies in exploring and optimizing cost-effectiveness. Economic analyses comparing traditional treatments with 3D-printed scaffolds could help better position the technology for adoption in healthcare systems.

In summary, the continuation of this research should focus on more simulations, experimental manufacturing, biological evaluation and economic evaluation. Together, these steps will bring the technology closer to clinical use, enabling the reliable production of customized, load-bearing bone implants for real-world orthopedic applications.

7. Conclusion

This study demonstrated a comprehensive approach to the design, simulation, and evaluation of 3D-printed lattice implants for the treatment of large femoral bone defects. To precisely locate and define the defect area, a patient-specific anatomical model was created starting with a CT-based reconstruction of the femur. A Voronoi lattice structure was chosen for the implant's design using nTopology software because of its biomimetic qualities, specifically its capacity to mimic the porous nature of cancellous bone and to encourage osteogenesis and osseointegration while preserving mechanical performance.

ANSYS Additive, a specialized tool for Selective Laser Melting (SLM) process modeling, was used to conduct the simulations. A high-resolution 10 mm slice simulation was used to get around computational limitations and obtain a better understanding of local structural responses after a full-scale scaffold simulation was used to assess global behavior. Fine details lost in the full scaffold model were uncovered by the high-resolution 10 mm slice simulation. Local stress concentrations, subtle deformation patterns, and small-scale blade crash risks were more clearly identified, particularly in overhangs and curved regions of the lattice. This reinforced the value of multi-scale simulation—using the full model for macro-level insight and detailed slices for local performance evaluation.

Afterwards multiple manufacturing parameters were tested individually by simulating the printing process of a cube shaped lattice. These included laser power, laser beam width, layer height, and scan speed, to investigate their influence on four critical outcomes: displacement, maximum von Mises stress during printing, high strain severity and potential recoater blade crash locations.

Results showed that layer height and laser power had the most pronounced effects on print quality and mechanical consistency while laser width and scan speed did not affect our results much. A layer height of $50\mu m$ and a laser power of 195W or higher provided the best results without increasing the manufacturing time. Laser beam width and scan speed showed minimal impact within the tested range ($80-120\mu m$, 600-1400m m/s), indicating flexibility in optimizing print speed without sacrificing quality.

In conclusion, this thesis validates a digital workflow for developing patient-specific, load-bearing lattice implants that combines anatomical modeling, advanced lattice design, and in-depth additive manufacturing simulation. The findings highlight the importance of parameter optimization and localized simulation fidelity, and offer a strong foundation for future experimental validation and clinical translation of 3D-printed orthopedic implants.

References

- [1] REVIEW ARTICLE Distal femur fractures. Surgical techniques and a review of the literature M. Ehlinger * , G. Ducrot , P. Adam , F. Bonnomet 29 October 2012.
- [2] Sheen JR, Mabrouk A, Garla VV. Fracture Healing Overview. [Updated 2023 Apr 8]. In: StatPearls [Internet]. Treasure Island (FL): StatPearls Publishing; 2024 Jan-. Available from: https://www.ncbi.nlm.nih.gov/books/NBK551678/.
- [3] Duan ZW, Lu H. Effect of Mechanical Strain on Cells Involved in Fracture Healing. Orthop Surg. 2021 Apr;13(2):369-375. doi: 10.1111/os.12885. Epub 2021 Jan 25. PMID: 33496077; PMCID: PMC7957396
- [4] Sheen JR, Mabrouk A, Garla VV. Fracture Healing Overview. [Updated 2023 Apr 8]. In: StatPearls [Internet]. Treasure Island (FL): StatPearls Publishing; 2024 Jan-. Available from: https://www.ncbi.nlm.nih.gov/books/NBK551678/.
- [5] Mehmood, Seemab & Ansari, Umar & Ali, Murtaza Najabat & Rana, Nosheen. (2014). Internal fixation: An evolutionary appraisal of methods used for long bone fractures. International Journal of Biomedical and Advance Research. 5. 142. 10.7439/ijbar.v5i3.627.
- [6] https://teachmeanatomy.info/lower-limb/bones/femur/.
- [7] Retrogade Nailing[Lee, Hohyoung & Jeong, Ji-Ho & Kim, Min-Su & Kim, Bum-Soo. (2018). Factors Affecting Posterior Angulation in Retrograde Intramedullary Nailing for Distal Femoral Fractures. Journal of the Korean Fracture Society. 31. 50. 10.12671/jkfs.2018.31.2.50.
- [8] Antegrade Interlocking Intramedullary Nailing in Humeral Shaft Fractures C. Cho, K. Song, Sin Ki Kim Published in International Conference on 30 June 2010.
- [9] Schulze F, Lang A, Schoon J, Wassilew GI, Reichert J. Scaffold Guided Bone Regeneration for the Treatment of Large Segmental Defects in Long Bones. Biomedicines. 2023 Jan 24;11(2):325. doi: m10.3390/biomedicines11020325.
- [10] Bruinink A., Luginbuehl R. Evaluation of Biocompatibility Using In Vitro Methods: Interpretation and Limitations. Adv. Biochem. Eng. Biotechnol. 2011;126:117–152. doi: 10.1007/10_2011_111.
- [11] Lei P., Sun R., Wang L., Zhou J., Wan L., Zhou T., Hu Y. A New Method for Xenogeneic Bone Graft Deproteinization: Comparative Study of Radius Defects in a Rabbit Model. PLoS ONE. 2015;10:e0146005. doi: 10.1371/journal.pone.0146005.
- [12] Li Z, Wang Q, Liu G. A Review of 3D Printed Bone Implants. Micromachines (Basel). 2022 Mar 27;13(4):528. doi: 10.3390/mi13040528. PMID: 35457833; PMCID: PMC9025296.
- [13] Anketa Jandyal, Ikshita Chaturvedi, Ishika Wazir, Ankush Raina, Mir Irfan UI Haq, 3D printing A review of processes, materials and applications in industry 4.0, Sustainable Operations and Computers, Volume 3, 2022, Pages 33-42, ISSN 2666-4127, https://doi.org/10.1016/j.susoc.2021.09.004.
- [14] Konda Gokuldoss, P., Kolla, S., & Eckert, J. (2017). "Additive manufacturing processes: Selective laser melting, electron beam melting, and binder jetting—Selection guidelines." Materials, 10(6), 672.
- [15] Sing SL, An J, Yeong WY, Wiria FE. Laser and electron-beam powder-bed additive manufacturing of metallic implants: A review on processes, materials and designs. J Orthop Res. 2016 Mar;34(3):369-85. doi: 10.1002/jor.23075. Epub 2015 Oct 29. PMID: 26488900.
- [16] An Overview of Extensive Analysis of 3D Printing Applications in the Manufacturing Sector, M. Jayakrishna, M. Vijay, Baseem Khan First published: 20 December 2023 https://doi.org/10.1155/2023/7465737.

- [17] Willems, Nop & Langenbach, Geerling & Everts, Vincent & Zentner, Andrej. (2013). The microstructural and biomechanical development of the condylar bone: A review. European journal of orthodontics. 36. 10.1093/ejo/cjt093.
- [18] Zaharin, H.A.; Abdul Rani, A.M.; Azam, F.I.; Ginta, T.L.; Sallih, N.; Ahmad, A.; Yunus, N.A.; Zulkifli, T.Z.A. Effect of Unit Cell Type and Pore Size on Porosity and Mechanical Behavior of Additively Manufactured Ti6Al4V Scaffolds. Materials 2018, 11, 2402. https://doi.org/10.3390/ma11122402.
- [19] Nicolas Soro, Hooyar Attar, Xinhua Wu, Matthew S. Dargusch, Investigation of the structure and mechanical properties of additively manufactured Ti-6Al-4V biomedical scaffolds designed with a Schwartz primitive unit-cell, Materials Science and Engineering: A, Volume 745, 2019, https://doi.org/10.1016/j.msea.2018.12.104.
- [20] S. Gómez, M.D. Vlad, J. López, E. Fernández, Design and properties of 3D scaffolds for bone tissue engineering, Acta Biomaterialia, Volume 42, 2016.
- [21] Materials Properties Handbook: Titanium Alloys, R. Boyer, G. Welsch, and E. W. Collings, eds. ASM International, Materials Park, OH, 1994.
- [22] Skripnyak, V.V.; Skripnyak, V.A. Localization of Plastic Deformation in Ti-6Al-4V Alloy. Metals 2021, 11, 1745. https://doi.org/10.3390/met11111745.
- [23] Gong, H., Rafi, K., Gu, H., Starr, T., & Stucker, B. (2014). "Analysis of defect generation in Ti-6Al-4V parts made using powder bed fusion additive manufacturing processes".
- [24] Additive Print and Science User's Guide, Release 2024 R1, January 2024
- [25] Cassandra Villicana, Ni Su, Andrew Yang, Xinming Tong, Hung Pang Lee, Manish Ayushman, Jeehee Lee, Michelle Tai, Tayne Kim, Fan Yang, Incorporating Bone-Derived ECM into Macroporous Microribbon Scaffolds Accelerates Bone Regeneration, January 2025.
- [26] Teixeira, Ó.; Silva, F.J.G.; Ferreira, L.P.; Atzeni, E. A Review of Heat Treatments on Improving the Quality and Residual Stresses of the Ti–6Al–4V Parts Produced by Additive Manufacturing. *Metals* **2020**, *10*, 1006. https://doi.org/10.3390/met10081006